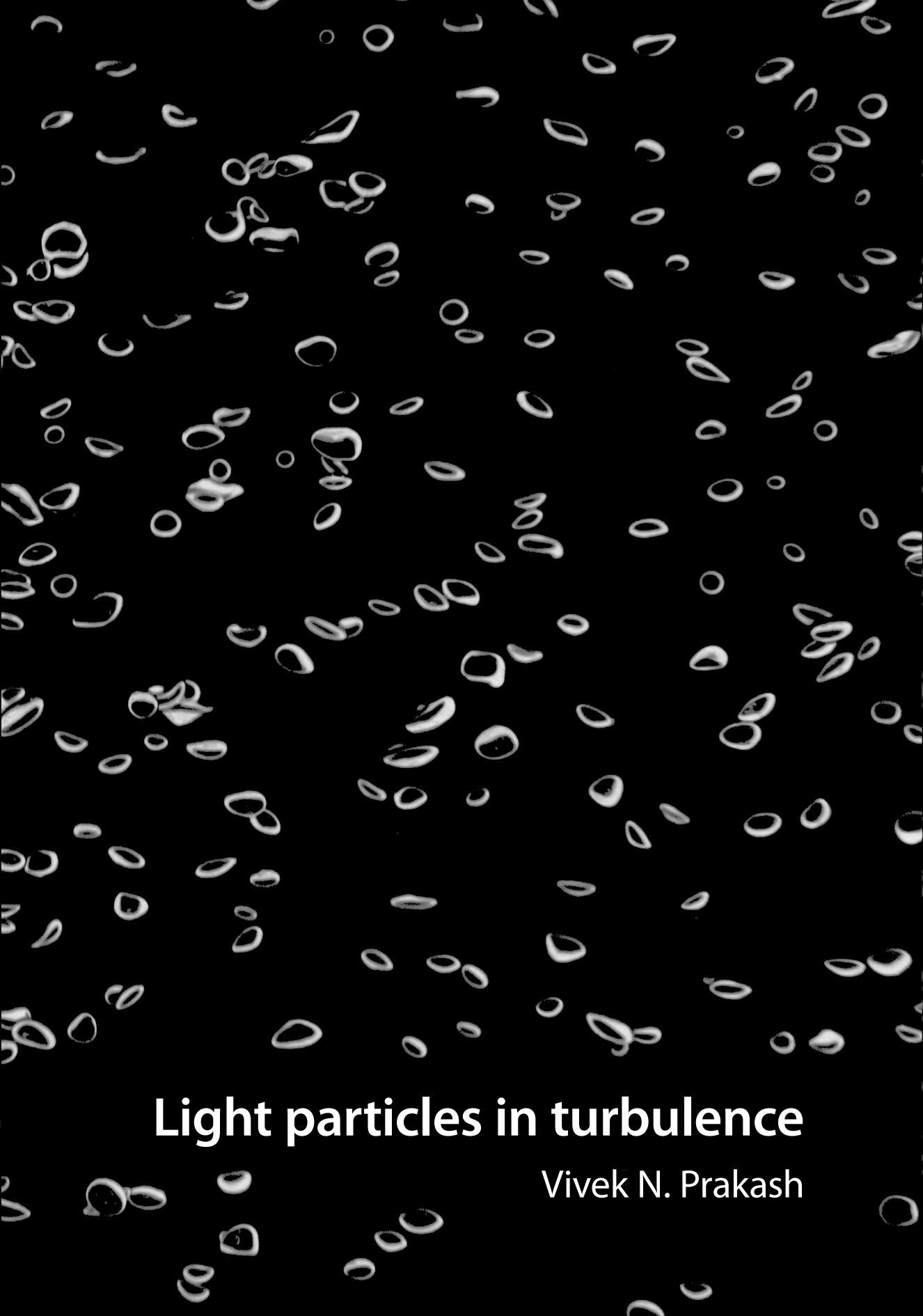

Light particles in turbulence

Vivek N. Prakash

Light particles in turbulence

Vivek Nagendra Prakash

Samenstelling promotiecommissie:

Prof. dr. Gerard van der Steenhoven (voorzitter)	Universiteit Twente
Prof. dr. Detlef Lohse (promotor)	Universiteit Twente
Dr. Chao Sun (assistent promotor)	Universiteit Twente
Prof. dr. Mickael Bourgoin	Université de Grenoble
Prof. dr. ir. Rob Hagmeijer	Universiteit Twente
Prof. dr. ir. Harry W. M. Hoeijmakers	Universiteit Twente
Prof. dr. Devaraj van der Meer	Universiteit Twente
Prof. dr. Federico Toschi	Technische Universiteit Eindhoven

UNIVERSITY OF TWENTE.

Physics of Fluids Group
University of Twente

European High-performance
Infrastructures in Turbulence
(EuHIT)

Action MP0806
Particles in turbulence

The work in this thesis was carried out at the Physics of Fluids group of the Faculty of Science and Technology of the University of Twente. It was supported by the University of Twente, the European High-performance Infrastructures in Turbulence (EuHIT) consortium and the European Cooperation in Science and Technology (COST) Action MP0806: *Particles in turbulence*.

Nederlandse titel:
Lichte deeltjes in turbulentie

Cover design: Sander G. Huisman and Vivek N. Prakash
Front cover: Freely rising bubbles in the Twente Water Tunnel

Publisher: Vivek Nagendra Prakash, Physics of Fluids Group, University of Twente, P.O. Box 217, 7500 AE Enschede, The Netherlands
Web: http://pof.tnw.utwente.nl, E-mail: viveknprakash@gmail.com

Printer: Gildeprint, Enschede

ISBN: 978-90-365-0724-0
DOI: 10.3990/1.9789036507240

LIGHT PARTICLES IN TURBULENCE

PROEFSCHRIFT

ter verkrijging van
de graad van doctor aan de Universiteit Twente,
op gezag van de rector magnificus,
Prof. dr. H. Brinksma,
volgens besluit van het College voor Promoties
in het openbaar te verdedigen
op donderdag 26 september 2013 om 16.45 uur

door

Vivek Nagendra Prakash
geboren op 26 September 1985
te Bangalore, India

Dit proefschrift is goedgekeurd door de promotor:

Prof. dr. rer. nat. Detlef Lohse

en de assistent-promotor:

Dr. Chao Sun

Contents

1 Introduction

1.1 Turbulence

Fluid turbulence is all around us - in our common everyday experience - for example on a typical flight journey we 'experience' unpleasant spells of turbulence, or when we quickly stir the sugar in our coffee, we 'induce' turbulence to help speed-up the mixing process. Turbulent fluid flow is an amazingly ubiquitous phenomenon found over length-scales ranging over many orders of magnitude; from the smallest, e.g. bacterial turbulence $\sim O(\mu m)$ [1] to the largest, e.g. astrophysical turbulence $\sim O(Mm)$ [2]. Turbulence is a complex phenomenon and has challenged the best scientific minds throughout history. Feynman described turbulence as "the most important unsolved problem of classical physics" [3].

Rather than seeking a definition of turbulence, it is more useful to outline typical features that characterize it. Turbulent flows are highly irregular, random and chaotic, hence a statistical description is necessary. The presence of a range of length scales complicates the problem, as turbulent eddies with different time and length scales interact with each other. Intermittency is another typical feature of turbulent flows, where sudden and rare violent fluctuations can arise. Turbulent flows are mathematically described by the Navier-Stokes equations, and the non-linearity makes them difficult to treat. Using pipe flow experiments, Osborne Reynolds (back in 1883 [4]) showed that the flow can be laminar or turbulent, depending on the value of a dimen-

sionless number, the Reynolds number (*Re*), named after him. The Reynolds number is a ratio of the inertial to viscous forces, and in a pipe flow is defined as $Re = UD/\nu$, where U is the fluid velocity, D is the pipe diameter, and ν is the kinematic viscosity of the fluid. Compared to laminar flows, Turbulent flows have the ability to transport and mix fluid much more effectively. Turbulent flows are also dissipative in nature; an external energy input is required to sustain the turbulence.

The broad framework describing turbulence was laid out first by Richardson in 1922 [5], and later (1941) extended by Kolmogorov [6, 7]. The big picture consists of an energy cascade process in which the energy injected at the large scale eddies is transferred successively to smaller and smaller eddies until finally it is dissipated as heat by viscosity. Kolmogorov further assumed that at sufficiently large *Re*, the turbulence can be assumed to be statistically isotropic at length scales smaller than the largest scale eddies. These small-scale motions are universal and independent of the large-scale geometry of the eddies determined by the boundary conditions. In this inertial sub-range, the flow is determined by the dissipation rate ε alone. At even smaller scales (Kolmogorov length scales), we reach the dissipation regime where viscosity starts dominating, and the flow is now determined by both the ε and the viscosity ν.

Turbulent flow research can be broadly categorized into three types [8]: (i) *discovery*, where the goal is to provide new information about specific type of turbulent flows, (ii) *modeling*, where mathematical models are developed to accurately describe and predict the flow properties, and (iii) *control*, where the idea is to manipulate the turbulence in a beneficial way - the engineering approach - to enhance efficiencies, reduce drag, etc. The contribution of this thesis is primarily in the *discovery* of new physics: We have investigated unexplored flow regimes, i.e. light particles in turbulence, and provide novel fundamental insights. Such new information is complementary to modeling approaches; we have compared our experimental results with numerical simulations to test their performance. With an improved understanding of the fundamental physics of particles in turbulence, it is only a matter of time before this knowledge can be exploited for engineering applications.

1.2 Particles in Turbulence

A vast majority of fluid flows found in nature and in the industry are turbulent and contain dispersed particles; there are abundant examples - like pollutant dispersion in the atmosphere, cloud formation, plankton distribution in the oceans, sedimentation in rivers, sand storms, volcanic eruptions, protoplanetary disks, or fuel spray combustion in the industry; the list goes on (see Figure 1.1). Hence, ‘particles in turbulence’

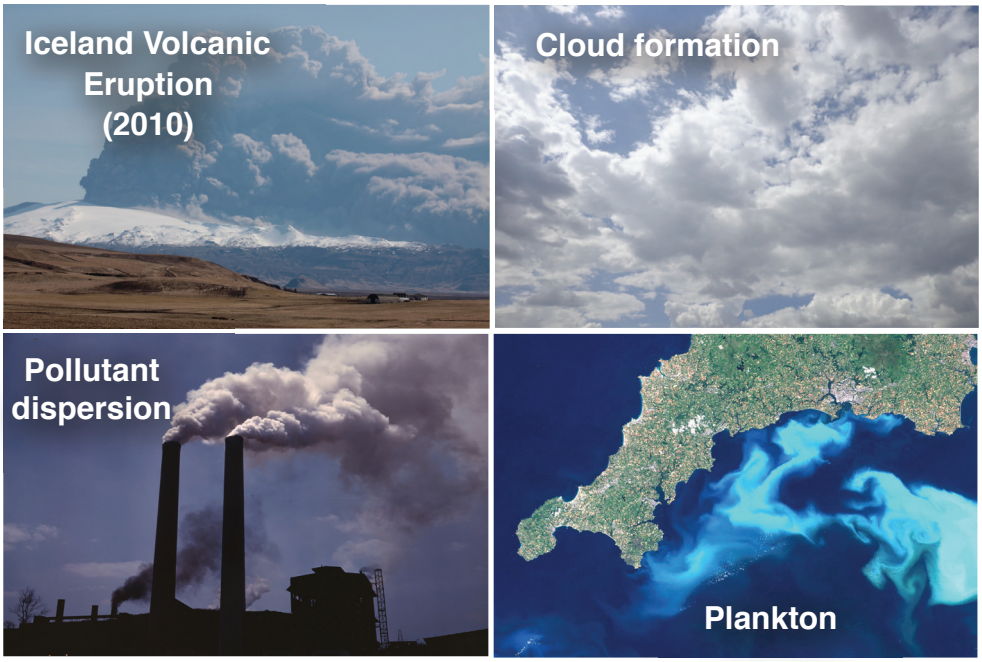

Figure 1.1: Examples of particles in turbulence in nature (Images from wikipedia, Creative Commons license).

is an important topic in physics with applications in a diverse number of fields. We recall the recent Iceland volcanic eruption (Eyjafjallajökull, 2010), which released ash around northern Europe causing major air-travel disruption for weeks. Clearly, it was important to determine the ash spreading and concentration to answer the big question - 'When is it safe to fly the planes again?'. This is an apt example illustrating the crucial importance of understanding the dynamics of particles in turbulence. Here, the broad research goal is to model and understand different aspects of these systems to enable optimal designs, predictions and precautions.

Let us consider the most simplified case - a dilute system of passive particles in a turbulent flow, which is referred to as the one-way coupling case (the particle dynamics is influenced by the turbulence alone). If the particles are sufficiently small (compared to the smallest length scale of the flow, the Kolmogorov length scale), and have a density equal to that of the surrounding fluid, then these particles faithfully follow the fluid motion. Such particles are called 'tracers' in experimental investigations. When the above-mentioned conditions are not met, there is a deviation from the tracer particle dynamics, and these particles are now called inertial particles. The

complexity of the particle dynamics increases drastically - if the particles are 'active' (e.g. oceanic planktons can swim), or if the particles exchange energy or mass (e.g. water droplets in clouds). Also, if the particle concentration (void fraction) increases, they can exert a back-reaction on the flow, leading to a two-way coupling (both particles and the surrounding fluid turbulence affect each other). When the particle concentration becomes significant, there might even be four-way coupling dynamics (in addition to two-way coupling, there can be particle-particle hydrodynamic interactions and collisions) [9, 10].

Given these complexities, particles in turbulence pose a challenging multitude of problems. The experimental tools and computational power available to address the enormity of these problems have been available only in the last decade [11–13]. The exact form of the equation of motion for inertial particles is still lacking and most of the current analysis relies on simplified limiting cases [14]. In recent years, significant progress has been made using a Lagrangian approach, where the particles are followed in their frame of reference. In this thesis, we study the dynamics of particles in well-controlled homogeneous and isotropic turbulent flow conditions in a laboratory. As discussed earlier, all types of high Reynolds number turbulent flows can be approximately considered to be homogeneous and isotropic at sufficiently small length-scales, hence, ours is a truly fundamental investigation of particles in turbulence.

1.3 Key research issues addressed in this thesis

1.3.1 Light particles in turbulence: Lagrangian statistics

In the investigation of particles in turbulence, an important research objective is to probe the statistical properties (for example the Lagrangian velocity and acceleration) of the particles suspended in turbulent flows. It has been established that the Lagrangian acceleration of a tracer particle in a turbulent flow at high Reynolds numbers (Re) is a very intermittent quantity [11]. This was revealed by the highly non-Gaussian statistics and stretched exponential tails of the acceleration probability distribution function (PDF). In fully developed turbulent flow (at high Re), there exist coherent structures in the flow which are small elements of intense vorticity, called as 'vortex filaments'. It is believed that the highly intermittent acceleration events are related to the interaction of the fluid (tracer) particles with these vortex filaments[13, 15]. When these tracers are trapped and ejected from vortex filaments, they experience highly intermittent accelerations, which is reflected in the wide non-Gaussian tails of the acceleration PDF.

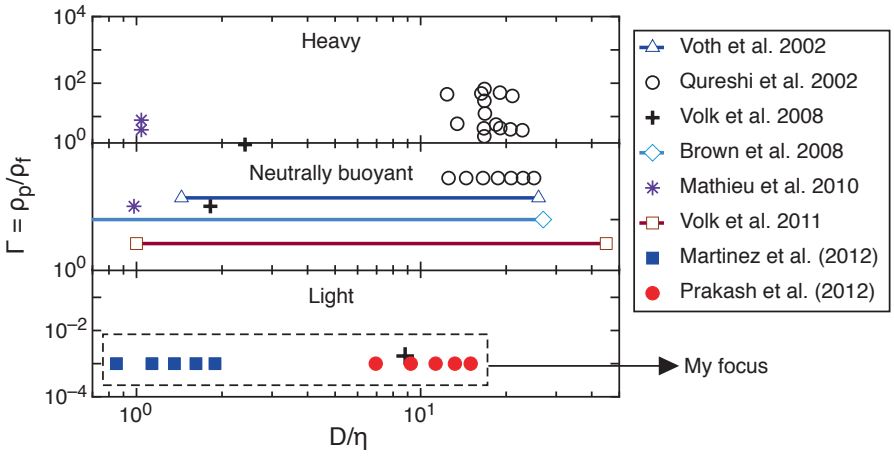

Figure 1.2: Parameter space of the density ratio $\Gamma = \rho_p/\rho_f$ (ratio of particle density to fluid density) versus size ratio, D/η (ratio of particle diameter to the Kolmogorov scale) for particles in turbulence, from data available in literature (from Chapter 3, Ref. [16]). Majority of previous studies (see Chapter 3 for the full references) have focused on $\Gamma \geq 1$, while I have explored light particles ($\Gamma \ll 1$): ■ (Chapter 2, Ref. [17]), ● (Chapter 3, Ref. [16]).

Early studies on Lagrangian turbulence were focused on tracer particles [11, 18, 19], so a lot is known about them. However, things get more interesting when we consider non-tracer particles. Suppose that the particle is still passive and small, but its density is varied, then overall we have three types of particles - light, heavy and neutrally buoyant. One would expect that the different particle-vortex filament interactions for light, heavy and neutrally buoyant particles will lead to differences in the acceleration, and other statistical quantities. Hence, it is fundamentally interesting to study inertial particles with a different density compared to the carrier fluid. There have been rather few experimental studies on light particles in turbulence, mainly due to the challenges involved in the experimental infrastructure, techniques and analysis, but are of great importance for a fundamental understanding of particles in turbulence. Therefore, in this thesis we have investigated the dynamics of light particles (bubbles and rigid hollow spheres) in turbulence in detail, which is an unexplored regime in current literature (see Figure 1.2).

I have conducted experiments in a unique large-scale (8*m* high, 3-storey) multiphase turbulence facility* - the Twente Water Tunnel (see Figure 1.3), which is part

*A short *(5-min)* video summary is available in Ref. [20]

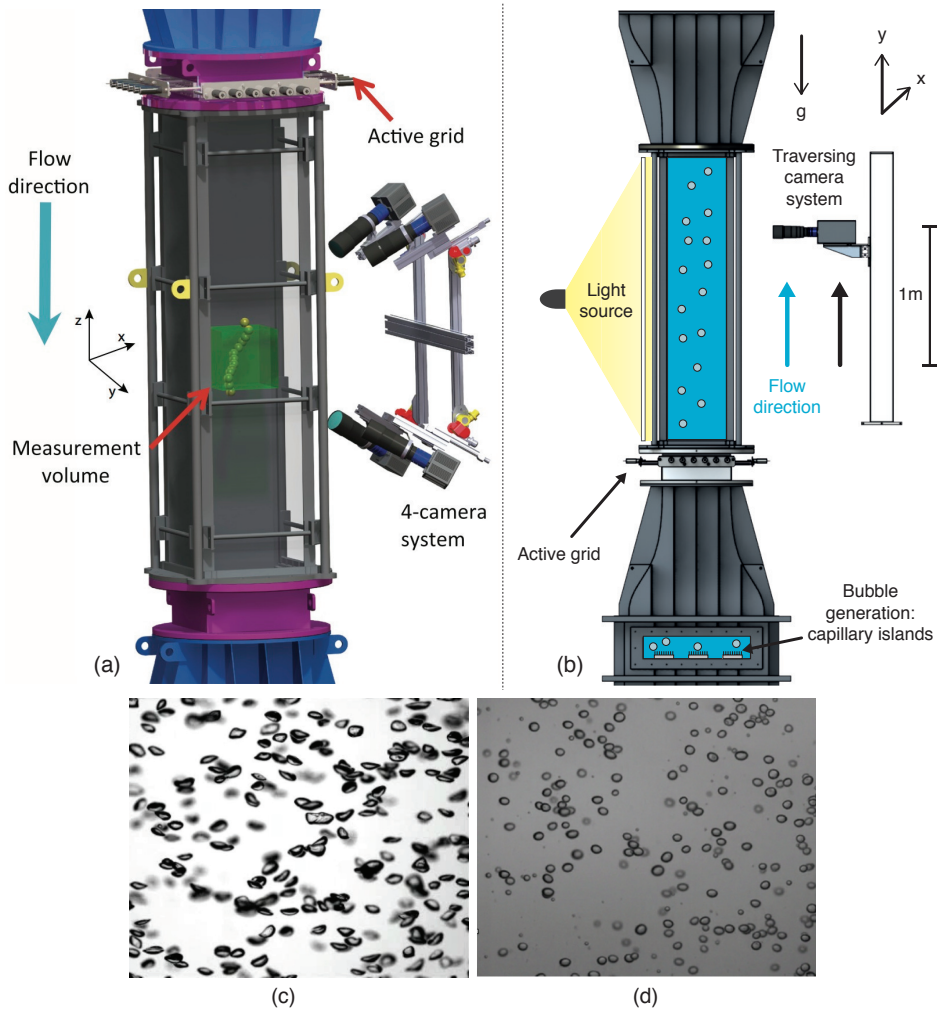

Figure 1.3: The Twente Water Tunnel facility: vertical water tunnel with nearly homogeneous and isotropic turbulence generated by an active-grid. (a) 3D micro-bubble trajectories are captured using a 4-camera arrangement (Chapter 2, Ref. [17]). (b) Bubbles are dispersed from below through capillary islands and the camera moves along with the rising bubbles, allowing the measurement of long-duration Lagrangian trajectories (Chapter 3, Ref. [16]). (c) Freely rising deformable bubbles of diameters $\sim 5mm$ in tap water. (d) Bubbles of diameters $\sim 3mm$ in surfactant solution (from Ref. [16]).

of the European High-performance Infrastructures in Turbulence (EuHIT) consortium. The water tunnel is a vertical closed-loop system where water can be recirculated at different speeds using a pump. An active-grid is used to generate nearly homogeneous and isotropic turbulence when there is a mean flow of water across the grid [21]. Bubbles are injected from below by blowing air through capillary needles, and they rise through an optically transparent measurement section and escape at the top [22, 23]. I have experimentally studied the acceleration statistics of light particles (micro-bubbles) in turbulence (Chapter 2), by implementing the challenging *3D Lagrangian Particle Tracking (LPT)* technique for the first time in our group (see Figure 1.3(a)). This technique allows us to track thousands of micro-bubbles in fully developed turbulence in 3D, with full temporal and spatial resolution [17].

So far I have only discussed small particles, but in real-world applications the dispersed particles are usually larger in size compared to the Kolmogorov length scale. These 'finite-sized' particles are no longer able to follow the fluid motion faithfully, as they filter out the smallest-scale fluctuations. In this context, I studied the accelerations statistics of finite-sized light particles (~ 3 *mm* sized air bubbles in water) in turbulence (Chapter 3). I developed a *sled-based particle tracking system* which moved a high-speed camera along with the bubbles, and provided results with greatly improved statistics (see Figure 1.3(b)). I adapted the *Circular Hough Transform* technique (for the first time in the field) to detect overlapping bubbles in the images. This investigation provided novel insights into the effects of finite-size and gravity on the acceleration variance and intermittency [16]. We compared these experimental results with direct numerical simulations of bubbles in turbulence at comparable Reynolds numbers. The numerical simulations considered the particle finite-size effects by implementing the Faxèn corrections [24]. The finite-sized bubble results discussed in Chapter 3 indicate a complex interplay between gravity and inertia. These experiments also revealed an unexpected influence of gravity on the acceleration statistics, which is usually ignored in numerical simulations except in a few cases (e.g. [25]).

1.3.2 Turbulent bubbly flow

While understanding the physics of dilute systems (1-way coupling) is a key first step, the ensuing step is to study systems where the particle concentration is no longer dilute (2-way coupling or 4-way coupling). This situation, though more complicated than before, is not only of fundamental interest but also has practical applications, for example in the chemical engineering industry where bubble columns are widely used for a variety of purposes - such as cleaning, reactions, etc. This has motivated us to experimentally study a swarm of rising deformable bubbles with and without

the presence of an external active-grid-induced turbulent flow.

In this thesis, we have adopted the Lagrangian approach for the study of dilute systems of light particles in turbulence; i.e. for micro-bubbles in Chapter 2 and finite-sized bubble in Chapter 3. Once the particle concentration becomes significant, the opacity of the flow makes it difficult to employ optical-based experimental techniques like Lagrangian Particle Tracking. In this situation, we are compelled to resort an intrusive technique like hot-film anemometry, which can provide high temporal resolution Eulerian single-point flow measurements. I have adopted the *phase-sensitive* Constant Temperature Anemometry (CTA) technique to measure the liquid velocity fluctuations in a turbulent bubbly flow at significant volume fractions of the bubbles (see Chapter 4). I have investigated a long-standing research issue regarding the transition between the $-5/3$ classical Kolmogorov energy spectrum for a single-phase flow and the well-known -3 pseudo-turbulence spectrum scaling for a swarm of bubbles rising in a quiescent liquid [26].

1.3.3 Particle clustering: 3D Voronoi analysis

We considered non-tracer particles with a different density compared to the carrier fluid; these particles can be of three types - light, heavy and neutrally buoyant. In fully developed turbulent flow, these inertial particles interact with the coherent structures, the vortex filaments. Heavy particles are expelled from the vortex filaments due to centrifugal forces, but light particles continue to be trapped for longer times inside the vortex filaments, while tracers have an intermediate behavior. This not only influences the acceleration statistics (Chapter 2), but also gives rise to a rich preferential clustering morphology, see Figure 1.4. The preferential clustering of particles in turbulence has recently attracted a lot of attention [13, 27, 28] driven by interest in both the fundamental physics and the applications. Particle clustering has been studied using different approaches such as box-counting [29, 30], pair correlation functions [31, 32], the Kaplan-Yorke dimension [27, 33], Minkowski functionals [27] and segregation indicators [34]. These approaches suffer from different drawbacks, and in this thesis we have used a novel approach - *the Voronoi analysis* - to study particle clustering (see Chapter 5).

In the context of turbulence, the Voronoi analysis was first applied to study inertial particle clustering in a two-dimensional (2D) cross-section [28]. The Voronoi analysis is basically a geometric tessellation method, where cells are constructed around particle positions based on information of the neighbouring particles. The key idea is that the local particle concentration is inversely proportional to the Voronoi cell area. The Voronoi cells for randomly distributed particles are known to follow a Gamma distribution, and probability distribution functions (PDFs) for inertial particles reveal

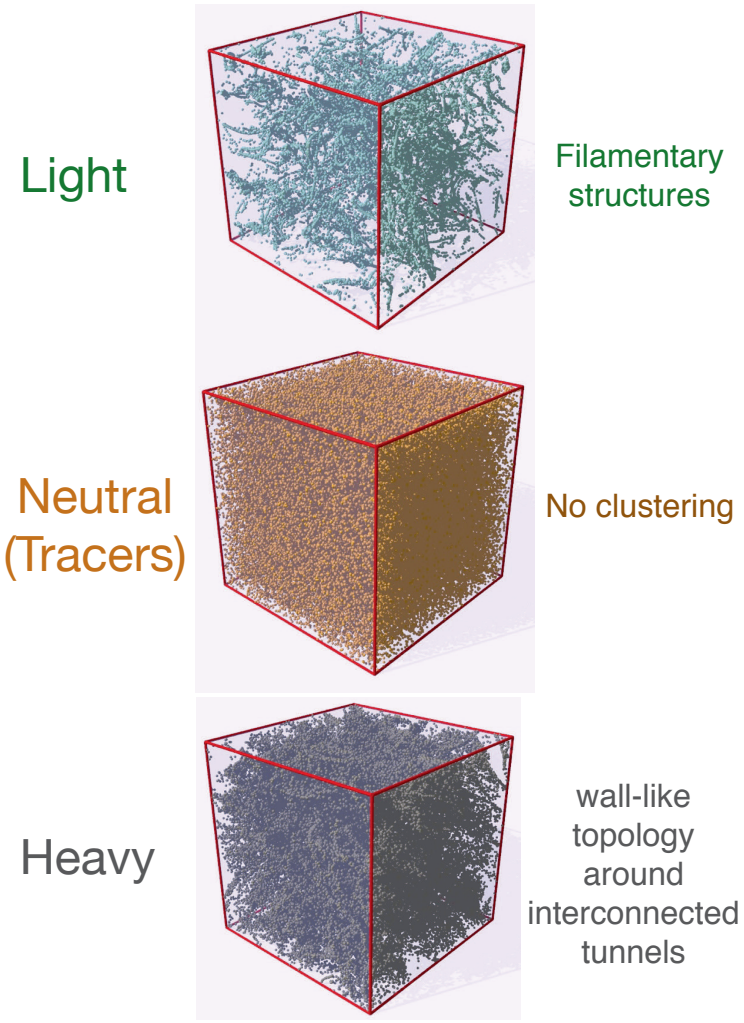

Figure 1.4: Preferential clustering of point-like particles depending on their density; Light particles accumulate in filamentary structures (Top panel), Heavy particles cluster in a wall-like topology (Middle panel) and tracer particles are distributed randomly (Lower panel), i.e. they do not show any clustering behaviour. These clustering snapshots are from a direct numerical simulation (DNS) of point-particles from Calzavarini *et al.*(Ref. [27]).

differences in the tails when compared to PDFs of randomly distributed particles. This information can be exploited to identify clustering in an Eulerian context. We extended the Voronoi analysis to three-dimensions (3D) and studied clustering using both point-particle DNS numerical simulations and micro-bubble experiments in our Water Tunnel [35]. The advantages offered by the Voronoi analysis technique include easy implementation and efficient computation, and no prior selection of an arbitrary length-scale is required. Since a Voronoi cell is defined at a particle position at every time step; for the first time, it is possible to obtain information on the Lagrangian temporal evolution of clusters. Hence, the Voronoi analysis technique offers new insights into the clustering phenomenon from a Lagrangian viewpoint (see Chapter 5).

We have also applied the *3D Voronoi analysis* to investigate the Eulerian clustering morphology of a swarm of freely rising deformable bubbles [36]. The Voronoi analysis was applied on data obtained from fully resolved front-tracking DNS simulations of freely rising bubbles [37]. The Voronoi analysis revealed the key parameter which decides the way the bubbles cluster (see Chapter 6).

1.4 A quick guide through this thesis

In this thesis, we have studied different aspects of light particles in turbulence. In the first two chapters, we elucidate our investigations on bubbles using Lagrangian Particle Tracking (LPT) experiments. In Chapter 2, we describe our experiments on micro-bubbles in turbulence. Here, the goal is to understand the inertial (density) effects. The micro-bubble Lagrangian acceleration statistics from the 3D LPT experiments were compared with results of light, heavy and neutrally buoyant particles in experiments and numerical simulations from other groups. In Chapter 3, we present results from experiments on finite-sized bubbles in turbulence. These experiments were conducted using a moving-sled based 2D LPT technique. We study the effects of finite-size and gravity on the acceleration statistics. In Chapter 4, we describe our turbulent bubbly flow experiments using the phase-sensitive hot-film technique. The key issue here is to understand the transition between the single-phase Kolmogorov turbulent energy spectrum scaling $-5/3$ and the spectrum scaling for freely rising bubbles -3. This is followed by chapters discussing our work on particle clustering using a 3D Voronoi analysis. Chapter 5 describes our clustering results for point-particle DNS simulations and micro-bubble experiments. In Chapter 6, we present results on the clustering morphology of freely rising deformable bubbles, where the data was obtained from front-tracking DNS simulations. Finally, we conclude and summarize the work done in this thesis. In the last two appendices, we present preliminary results on light rigid spheres and light rods in turbulence.

References

[1] J. Dunkel, S. Heidenreich, K. Drescher, H. H. Wensink, M. Bar, and R. E. Goldstein, *Fluid dynamics of bacterial turbulence*, Phys. Rev. Lett. **110**, 228102 (2013).

[2] A. Brandenburg and A. Nordlund, *Astrophysical turbulence modeling*, Rep. Prog. Phys. **74**, 046901 (2011).

[3] R. P. Feynman, R. B. Leighton, and M. L. Sands, *The Feynman lectures on physics, Vol. 1* (Addison Wesley, USA, 1963).

[4] O. Reynolds, *An experimental investigation of the circumstances which determine whether the motion of water shall be direct or sinuous, and of the law of resistance in parallel channels.*, Proc. Roy. Soc. London **35**, 84 (1883).

[5] L. F. Richardson, *Weather prediction by numerical process* (Cambridge University Press, UK, 1922).

[6] A. Kolmogorov, *The local structure of turbulence in incompressible viscous fluid for very large Reynolds number*, Proc. R. Soc. Lond. A **434**, 9 (1991).

[7] A. Kolmogorov, *Dissipation of Energy in the Locally Isotropic Turbulence*, Proc. R. Soc. Lond. A **434**, 15 (1991).

[8] S. Pope, *Turbulent flows* (Cambridge University Press, UK, 2000).

[9] S. Elghobashi and G. C. Truesdell, *On the two-way interaction between homogeneous turbulence and dispersed solid particles. I: Turbulence modification*, Physics of Fluids A: Fluid Dynamics **5**, 1790 (1993).

[10] S. Elghobashi, *On predicting particle-laden turbulent flows*, Applied Scientific Research **52**, 309 (1994).

[11] A. La Porta, G. Voth, A. M. Crawford, J. Alexander, and E. Bodenschatz, *Fluid particle accelerations in fully developed turbulence*, Nature. **409**, 1017 (2001).

[12] D. Lohse, *Particles go with the flow*, Physics **1**, 18 (2008).

[13] F. Toschi and E. Bodenschatz, *Lagrangian properties of particles in turbulence*, Annu. Rev. Fluid Mech. **41**, 375 (2009).

[14] M. Maxey and J. Riley, *Equation of motion for a small rigid sphere in a nonuniform flow*, Phys. Fluids **26**, 883 (1983).

[15] F. Toschi, L. Biferale, G. Boffetta, A. Celani, B. J. Devenish, and A. Lanotte, *Acceleration and vortex filaments in turbulence*, J. Turb. **6**, 15 (2005).

[16] V. N. Prakash, Y. Tagawa, E. Calzavarini, J. Martinez Mercado, F. Toschi, D. Lohse, and C. Sun, *How gravity and size affect the acceleration statistics of bubbles in turbulence*, New J. Phys. **14**, 105017 (2012).

[17] J. Martínez Mercado, V. N. Prakash, Y. Tagawa, C. Sun, and D. Lohse, *Lagrangian statistics of light particles in turbulence*, Phys. Fluids **24**, 055106 (2012).

[18] G. Voth, A. La Porta, A. M. Crawford, J. Alexander, and E. Bodenschatz, *Measurement of particle accelerations in fully developed turbulence*, J. Fluid Mech. **469**, 121 (2002).

[19] L. Biferale, G. Boffetta, A. Celani, B. J. Devenish, A. Lanotte, and F. Toschi, *Multifractal statistics of lagrangian velocity and acceleration in turbulence*, Phys. Rev. Lett. **93**, 064502 (2004).

[20] V. N. Prakash, *Video abstract for: Vivek N Prakash et al, New J. Phys. 14 105017* (New Journal of Physics, http://goo.gl/YGu1M, 2012).

[21] R. Poorte and A. Biesheuvel, *Experiments on the motion of gas bubbles in turbulence generated by an active grid*, J. Fluid Mech. **461**, 127 (2002).

[22] J. Rensen, S. Luther, and D. Lohse, *The effects of bubbles on developed turbulence*, J. Fluid Mech. **538**, 153 (2005).

[23] J. Martínez Mercado, D. Chehata Gómez, D. van Gils, C. Sun, and D. Lohse, *On bubble clustering and energy spectra in pseudo-turbulence*, J. Fluid Mech. **650**, 287 (2010).

[24] E. Calzavarini, R. Volk, M. Bourgoin, E. Leveque, J.-F. Pinton, and F. Toschi, *Acceleration statistics of finite-sized particles in turbulent flow: the role of Faxèn forces*, J. Fluid Mech. **630**, 179 (2009).

[25] I. Mazzitelli and D. Lohse, *Lagrangian statistics for fluid particles and bubbles in turbulence*, New J. Phys. **6**, 203 (2004).

[26] V. N. Prakash, J. Martinez Mercado, F. E. M. Ramos, Y. Tagawa, D. Lohse, and C. Sun, *Energy spectra in bubbly turbulence*, J. Fluid Mech. (submitted) arXiv:1307.6252 (2013).

[27] E. Calzavarini, M. Kerscher, D. Lohse, and F. Toschi, *Dimensionality and morphology of particle and bubble clusters in turbulent flow*, J. Fluid Mech. **607**, 13 (2008).

[28] R. Monchaux, M. Bourgoin, and A. Cartellier, *Preferential concentration of heavy particles: A Voronoi analysis*, Phys. Fluids **22**, 103304 (2010).

[29] J. Fessler, J. Kulick, and J. Eaton, *Preferential concentration of heavy particles in a turbulent channel flow*, Phys. Fluids **6**, 3742 (1994).

[30] A. Aliseda, A. Cartellier, F. Hainaus, and J. Lasheras, *Effect of preferential concentration on the settling velocity of heavy particles in homogeneous isotropic turbulence*, J. Fluid Mech. **468**, 77 (2002).

[31] L. Chen, S. Goto, and J. Vassilicos, *Turbulent clustering of stagnation points and inertial particles*, J. Fluid Mech. **553**, 143 (2006).

[32] E. Saw, R. Shaw, S. Ayyalasomayajula, P. Chuang, and A. Gylfason, *Inertial clustering of particles in high-Reynolds-number turbulence*, Phys. Rev. Lett. **100**, 214501 (2008).

[33] J. Bec, L. Biferale, G. Boffetta, A. Celani, M. Cencini, A. Lanotte, S. Musacchio, and F. Toschi, *Acceleration statistics of heavy particles in turbulence*, J. Fluid Mech. **550**, 349 (2006).

[34] E. Calzavarini, M. Cencini, D. Lohse, and F. Toschi, *Quantifying turbulence-induced segregation of inertial particles*, Phys. Rev. Lett. **101**, 084504 (2008).

[35] Y. Tagawa, J. Martínez Mercado, V. N. Prakash, E. Calzavarini, C. Sun, and D. Lohse, *Three-dimensional Lagrangian Voronoi Analysis for clustering of particles and bubbles in turbulence*, J. Fluid Mech. **693**, 201 (2012).

[36] Y. Tagawa, I. Roghair, V. N. Prakash, M. van Sint Annaland, H. Kuipers, C. Sun, and D. Lohse, *The clustering morphology of freely rising deformable bubbles*, J. Fluid Mech. **721**, R2 (2013).

[37] I. Roghair, M. van Sint Annaland, and J. A. M. Kuipers, *Drag Force and Clustering in Bubble Swarms*, AIChE J. **59**, 1791 (2013).

2

Lagrangian statistics of micro-bubbles in turbulence * †

We study the Lagrangian velocity and acceleration statistics of light particles (micro-bubbles in water) in homogeneous isotropic turbulence. Micro-bubbles with a diameter $d_b = 340$ μm and Stokes number from 0.02 to 0.09 are dispersed in a turbulent water tunnel operated at Taylor-Reynolds numbers (Re_λ) ranging from 160 to 265. We reconstruct the bubble trajectories by employing three-dimensional particle tracking velocimetry (PTV). It is found that the probability density functions (PDFs) of the micro-bubble acceleration show a highly non-Gaussian behavior with flatness values in the range 23–30. The acceleration flatness values show an increasing trend with Re_λ, consistent with previous experiments [1] and numerics [2]. These acceleration PDFs show a higher intermittency compared to tracers [3] and heavy particles [4] in wind tunnel experiments. In addition, the micro-bubble acceleration autocorrelation function decorrelates slower with increasing Re_λ. We also compare our results with experiments in von Kármán flows and point-particle direct numerical simulations with periodic boundary conditions.

*Published as: J. M. Mercado, Vivek N. Prakash, Y. Tagawa, C. Sun, and D. Lohse, Lagrangian statistics of light particles in Turbulence, Phys. Fluids, 24, 055106 (2012).

†Both J. M. Mercado and Vivek N. Prakash equally contributed to this work and are joint first authors.

2.1 Introduction

Multi-phase flows where the carrier fluid transports particles under turbulent conditions are ubiquitous. A thorough understanding of the dynamics of particles (light, neutral, or heavy) in turbulent flows is therefore crucial. In most of these flows, the particles have a finite size and their density is different from that of the carrier fluid. Thus, the particle's dynamic behavior is expected to be different compared to neutral fluid tracers. The two relevant dimensionless parameters are the density ratio $\beta = 3\rho_f/(\rho_f + 2\rho_p)$, where ρ_f and ρ_p are the fluid and particle density, and the Stokes number, which is the ratio of the particle's response time τ_p to the Kolmogorov time scale τ_η, defined as St$= \tau_p/\tau_\eta = a^2/3\beta\nu\tau_\eta$, where a is the particle radius and ν the kinematic viscosity of the carrier fluid.

The Lagrangian approach is naturally suited to study particles in turbulence and has recently attracted much attention (see Ref. [5]). Pioneering Lagrangian particle tracking experiments in fully developed turbulence used silicon strip detectors to measure three-dimensional trajectories of tracer particles (β=1) with high spatial and temporal resolution in a von Kármán flow at high Taylor-Reynolds numbers, Re_λ up to 970 [1, 6, 7]. The particle acceleration PDFs were found to be highly intermittent with flatness values around 55, and could be fitted with either stretched exponentials or log-normal distributions. The high intermittency of the fluid particle acceleration PDFs was also observed in numerical simulations [2, 8–10]. The normalized acceleration PDFs showed a weak dependence on the Re_λ, and this was more prominently seen in the flatness values, which have been found to increase with Re_λ in both experiments [1] and numerics [2].

More recent experimental investigations have focused on studying particles with different density than the carrier fluid [11–14]. Heavy particles ($\beta = 0$) in turbulence were studied using water droplets in wind tunnel experiments at Re_λ=250 [4]. By following the particle motion with a moving camera, their trajectories were obtained in two-dimensions. It was observed that the normalized acceleration PDF was less intermittent than for tracers, with narrower tails. Numerical simulations [15] have confirmed that the acceleration PDF of heavy particles is indeed slightly narrower than that of fluid tracers.

The dynamics of light particles in turbulence (β=3) have been investigated both numerically and experimentally. DNS in the point-particle limit [9] showed very high intermittency in the PDFs of the individual forces acting on bubbles. A direct comparison of the statistics of light, neutral, and heavy particles was done by Volk *et al.* [12], using data from both experiments and point-particle DNS. In their experiments an extended laser Doppler velocimetry technique (extended LDV) was used to measure the particle velocity in a von Kármán flow at high Re_λ=850. The experimental PDFs of

the normalized acceleration for light, neutral, and heavy particles did not reveal a visible difference within the experimental accuracy. In contrast, their numerical results showed that the acceleration PDF of light particles was more intermittent than that of tracers, and heavy particles showed less intermittency than tracers. They also found both in numerics and experiments, that the acceleration autocorrelation function of light particles decorrelates faster than those of neutrally buoyant and heavy particles.

In this chapter, we present an experimental study of the Lagrangian dynamics of light particles in turbulence. A majority of the previous Lagrangian particle tracking experiments focused mainly on tracer particles. Furthermore, grid-generated turbulence experiments in wind tunnels have dealt with either heavy or neutrally buoyant particles [3, 4, 11]. Previous experiments with bubbles [13] measured only one component of the velocity and acceleration in a von Kármán flow. Here, we provide results on the three components of the velocity, acceleration, and autocorrelation statistics of micro-bubbles (β=3) in homogeneous and isotropic turbulence. The micro-bubbles are dispersed in a turbulent water tunnel at moderate Re_λ (160—265), and their size is comparable to the Kolmogorov length scale. In the present experiments, the particle size ratio $\Phi = D/\eta$, where D is the particle diameter, and η is the Kolmogorov length scale, is in the range Φ = 0.8 to 1.9. The effect of finite-particle size on the Lagrangian acceleration statistics has been the subject of many recent investigations (see [1, 16–18]). It has been found that the acceleration statistics do not show significant changes : in experiments [1, 18] for $\Phi < 5$, and in numerics [17] for $\Phi < 2$. In the present chapter, the largest Φ value is ~ 1.9, and thus we conclude that finite-size effects do not play a significant role.

The structure of this chapter is as follows: in section 2.2 we describe the experimental facility and the smoothing algorithm for the particle trajectories. The results are presented in section 2.3, followed by a conclusion and summary in section 2.4.

2.2 Experiments and Data Analysis

2.2.1 Experimental Setup

We conduct experiments in the Twente Water Tunnel, an 8 m long vertical water tunnel designed for studying two-phase flows (see Figure 2.1). By means of an active grid, nearly homogeneous and isotropic turbulence with Re_λ up to 300 is achieved [see 19, 20]. A measurement section with dimensions $2\times0.45\times0.45$ m^3 with three glass walls provides optical access for the three-dimensional particle tracking velocimetry (PTV) system. Micro-bubbles with a mean diameter $d_b = 340 \pm 120$ μm are generated by blowing pressurized air through a ceramic porous plate that is lo-

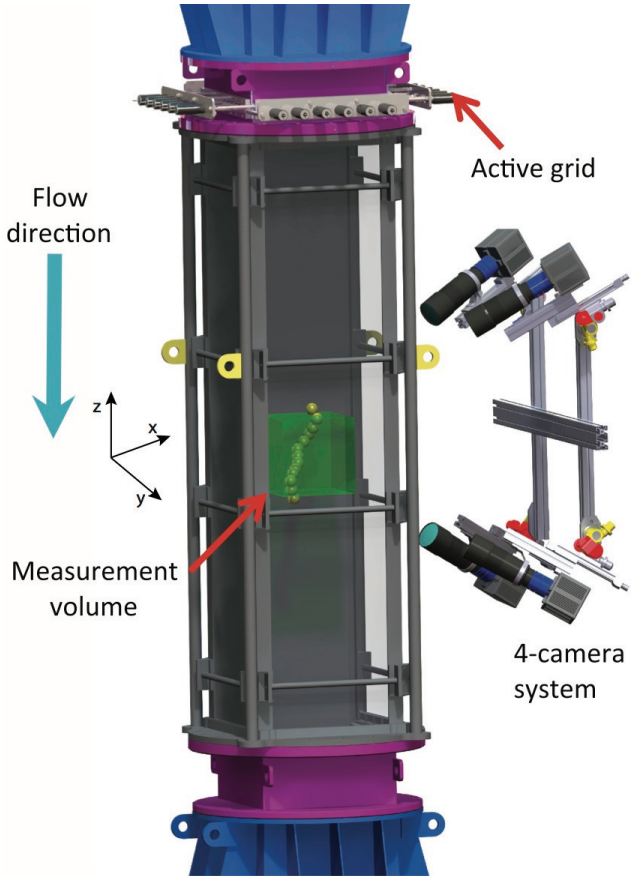

Figure 2.1: The Twente Water Tunnel: an experimental facility for studying two-phase turbulent flows. The picture shows the measurement section and on top the active grid, which allows homogeneous and isotropic turbulent flows upto $\mathrm{Re}_\lambda = 300$, and the 4-camera particle tracking velocimetry (PTV) system to detect the positions of particles in three-dimensions. For illumination we use a high energy, high-repetition rate laser. Micro-bubbles with a diameter $\approx$340 μm are generated above the active grid using a ceramic porous plate and are advected downwards into the measurement volume.

cated in the upper part of the water tunnel. These micro-bubbles are advected downwards by the flow and pass through the measurement section.

Our three-dimensional PTV system consists of four Photron PCI-1024 high-speed cameras that are synchronized with a high-energy (100 W), high-repetition rate (up to 10 kHz) Litron laser (LDY303HE). The four cameras are focused at the center of the test section on a $40 \times 40 \times 40$ mm^3 measurement volume that is illuminated by expanding the laser beam with volume optics. The arrangement of the cameras and laser is such that the four cameras receive forward scattered light from the micro-bubbles. We acquire images at 10,000 frames per second (fps) with a resolution of 256×256 pixels, resulting in a spatial resolution of about 156 μm/ pixel.

The Re_λ is varied by changing the mean flow speed of water in the tunnel. Table 2.1 summarizes the flow properties for the various cases considered. The flow was characterized by measurements using a cylindrical hot-film probe (Dantec R11) with a sampling rate of 10 kHz placed in the center of the imaged measurement volume. The dissipation rate ε was obtained from the Kolmogorov scaling for the second-order longitudinal structure function $D_{LL} = C_2(\varepsilon r)^{2/3}$, with $C_2 = 2.13$ [21]. For each case of mean flow speed in the water tunnel, the dissipation rate is obtained from the value of the plateau region (see Figure 2.2), and other parameters follow.

For the three-dimensional particle tracking, we use the open source code developed at the IfU-ETH group [22]. The error in the determination of the particle's position is within sub-pixel accuracy of 60 μm, corresponding to the tolerance of epipolar matching in three dimensions. In this chapter we focus on the Lagrangian statistics of micro-bubbles, but it is also possible to study particle clustering using the three-dimensional data (see Ref. [23]). Here, the raw particle trajectory is smoothed out with a polynomial fitting method (see section 2.2.2). Velocities and accelerations are obtained by differentiating the particle positions in the filtered trajectory. For the Lagrangian statistics shown in the results, the number of data points (N_{data}) used are larger than 4.5×10^6.

2.2.2 Smoothing method for particle trajectories

Experimental errors in the determination of the particle positions are unavoidable, and obtaining the particles' velocity and acceleration through a time differentiation of their positions would be very sensitive to these experimental errors. Hence, a smoothing of the particle trajectory has to be carried out. This smoothing process is a trade-off between filtering out the experimental noise and retaining the turbulent features of the particle motion. Therefore, the smoothing parameters must be very carefully selected.

In the Lagrangian Particle Tracking community, two different methods have been

Table 2.1: Summary of the flow parameters. V_{mean}: water mean flow speed, $\mathrm{Re}_\lambda = (15u_{rms}^4/\varepsilon\nu)^{1/2}$: Taylor-Reynolds number, u_{rms}: mean velocity fluctuation, $\eta = (\nu^3/\varepsilon)^{1/4}$ and $\tau_\eta = (\nu/\varepsilon)^{1/2}$: are the Kolmogorov's length scale and time scale respectively, L: integral length scale of the flow, ε: mean energy dissipation rate, $St = \tau_p/\tau_\eta$: Stokes number, and N_{data}: number of data points used to calculate the Lagrangian statistics.

V_{mean} m s^{-1}	Re_λ	u_{rms} m s^{-1}	η μm	τ_η ms	L mm	λ mm	ε m^2 s^{-3}	St	N_{data}
0.22	160	0.0161	400	160	64	9.9	39e-6	0.02	$5.5 \cdot 10^6$
0.33	175	0.022	300	90	54	7.8	123e-6	0.04	$9.4 \cdot 10^6$
0.45	195	0.027	250	65	56	7.0	237e-6	0.05	$8.3 \cdot 10^6$
0.57	225	0.035	210	47	58	6.4	450e-6	0.07	$6.5 \cdot 10^6$
0.65	265	0.043	180	35	70	6.0	786e-6	0.09	$4.5 \cdot 10^6$

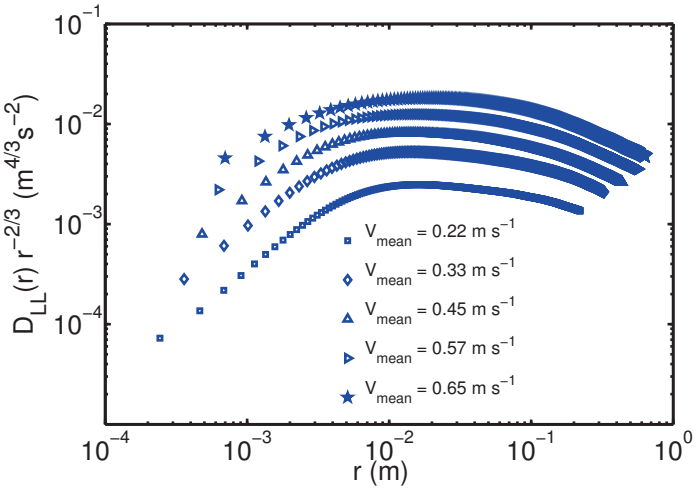

Figure 2.2: Flow parameters characterization from hot-film measurements. Compensated second-order longitudinal structure function $D_{LL}(r)$ calculated in order to estimate dissipation.

used to smoothen particle trajectories in turbulent flows. One method consists of fitting the trajectory to a polynomial of second or higher order [1, 24], whereas the other method uses a Gaussian kernel [4, 6, 16]. We tested both smoothing methods, and obtained very similar results. In the present chapter, we only show results obtained by smoothing the micro-bubble trajectories with a third-order polynomial (also referred as the moving cubic spline method).

The entire signal of the trajectory $x(t)$ is low-pass filtered by fitting a third-order polynomial. Using a fitting window with the particle positions from $t - Ndt$ until $t + Ndt$, where dt is the timestep, the filtered particle position at time i is calculated as follows:

$$x_{i,f}(t) = c_{i,0} + c_{i,1}t + c_{i,2}t^2 + c_{i,3}t^3. \tag{2.1}$$

The Lagrangian velocity and acceleration are obtained by differentiating the particle trajectory:

$$u_{i,f}(t) = c_{i,1} + 2c_{i,2}t + 3c_{i,3}t^2, \tag{2.2}$$

$$a_{i,f}(t) = 2c_{i,2} + 6c_{i,3}t. \tag{2.3}$$

The parameter N determines the length of the time window ($t - Ndt$, $t + Ndt$), and has to be appropriately chosen to ensure that the time fitting window is smaller than the typical turbulent time scale. We explore the effect of N on the r.m.s (root mean square) of the micro-bubble velocity (Figure 2.3a) and acceleration (Figure 2.3b) to find the optimum value for the case of Re_λ=195. One can observe in Figure 2.3a that the r.m.s of the velocity saturates at around $N = 40$, for smaller values of N there is an exponential rise owing to the noise. Since the acceleration is a second-order derived quantity, it is more sensitive to the choice of N as observed in figure 2.3b. Here, we can clearly distinguish two different regions: for small values of $N < 30$ the r.m.s again increases exponentially due to the noise, while at large values of $N > 100$ the a_{rms} reduces considerably as an effect of the over-smoothing. For the data presented in this chapter we have chosen values of N in the range 45—50, which correspond to normalized values of $N/\mathrm{fps} \times \tau_\eta$ in the range 0.03—0.14. It is important to point out that the normalized acceleration PDFs obtained by choosing N in this range (45—50) are similar for each Re_λ. The flatness of the acceleration PDF can also provide a measure to identify the optimal value of N (as shown in Figure 2.3c). We describe the details of the flatness calculation procedure in section 2.3.3. Here, in Figure 2.3c, we see that our chosen optimal value of N = 50 corresponds to the starting point in a region where the flatness values are decreasing with N as a result of over-smoothing. At $N < 10$, the decrease in flatness is an artificial effect arising from the noise. Hence, the optimal value of N is chosen such that we do not over-smoothen the micro-bubble trajectories.

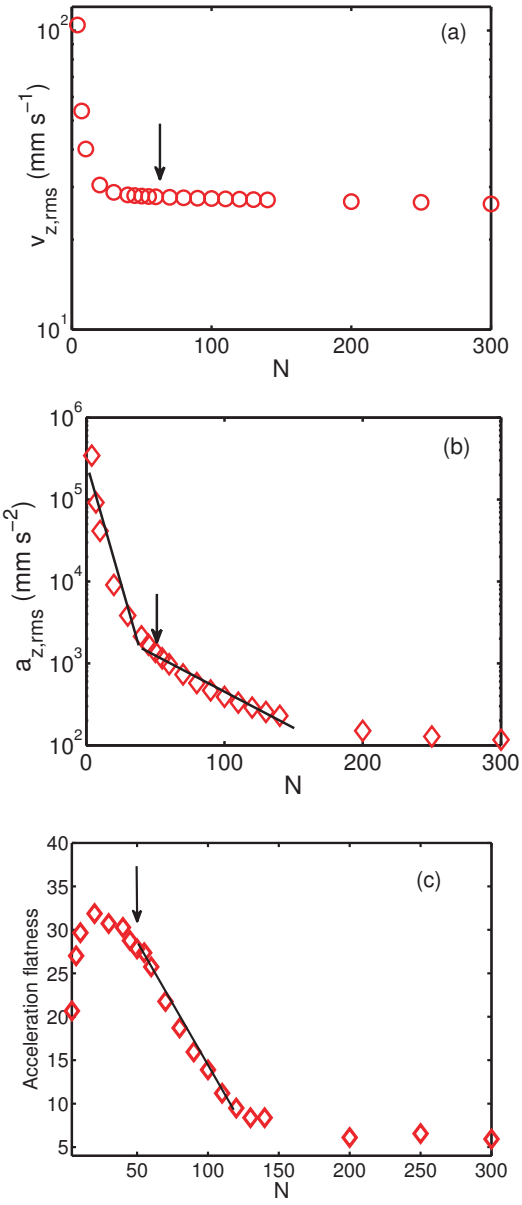

Figure 2.3: r.m.s of the vertical component of the micro-bubble (a) velocity and (b) acceleration, and (c) the acceleration flatness at Re_λ=195 as a function of N for polynomial smoothing. The arrows in the figures indicate the chosen value ($N = 50$) for the smoothing of the trajectories.

Table 2.2: flatness values of the distribution of micro-bubble velocities.

Re_λ	v_x	v_y	v_z
160	3.19 ± 0.13	3.19 ± 0.35	2.79 ± 0.09
175	3.09 ± 0.05	3.08 ± 0.33	2.96 ± 0.14
195	3.12 ± 0.02	3.07 ± 0.06	2.87 ± 0.10
225	3.04 ± 0.04	3.04 ± 0.09	3.25 ± 0.16
265	2.96 ± 0.05	3.01 ± 0.02	2.94 ± 0.06

2.3 Results

2.3.1 PDFs of micro-bubble velocity

In this section we present results on the PDFs of micro-bubble velocity obtained by smoothing the raw trajectories. Figure 2.4a shows the PDF of the three components of the normalized micro-bubble velocity at $\mathrm{Re}_\lambda = 195$. We observe that the velocity distributions of the three components closely follow a Gaussian profile. The flatness values F of these PDFs for different Re_λ (see Table 2.2) are close to that of a Gaussian distribution ($F = 3$). Gaussian-type flatness values have also been reported for neutrally buoyant particles in turbulent von Kármán flows. Voth *et al.* [1] measured velocity distributions close to Gaussian with flatness values in the range $2.8-3.2$, and more recently, Volk *et al.* [16] obtained sub-Gaussian distributions with flatness around $2.4-2.6$. In Figure 2.5a, we show a plot of the r.m.s values of the micro-bubble velocity versus Re_λ. We observe an increasing trend with Re_λ, and the three components are nearly isotropic. We also compare the r.m.s. values obtained from the hot-film data and find a reasonable agreement with the 3D-PTV velocity measurements.

2.3.2 PDFs of micro-bubble acceleration

Contrary to the velocity PDFs, the micro-bubble acceleration PDFs normalized with the r.m.s ($\mathrm{a}/\mathrm{a}_{rms}$) exhibit a strong non-Gaussian behavior. Figure 2.4b shows the PDFs for all the three components of the micro-bubble acceleration at $\mathrm{Re}_\lambda = 195$. We observe that the acceleration PDFs are highly intermittent with stretched tails that extend beyond $5\,\mathrm{a}_{rms}$, indicating that the probability of rare high acceleration events is much higher than for a Gaussian distribution. At this $\mathrm{Re}_\lambda (= 195)$, the acceleration is nearly isotropic as the PDFs of the three components show a good collapse atleast till

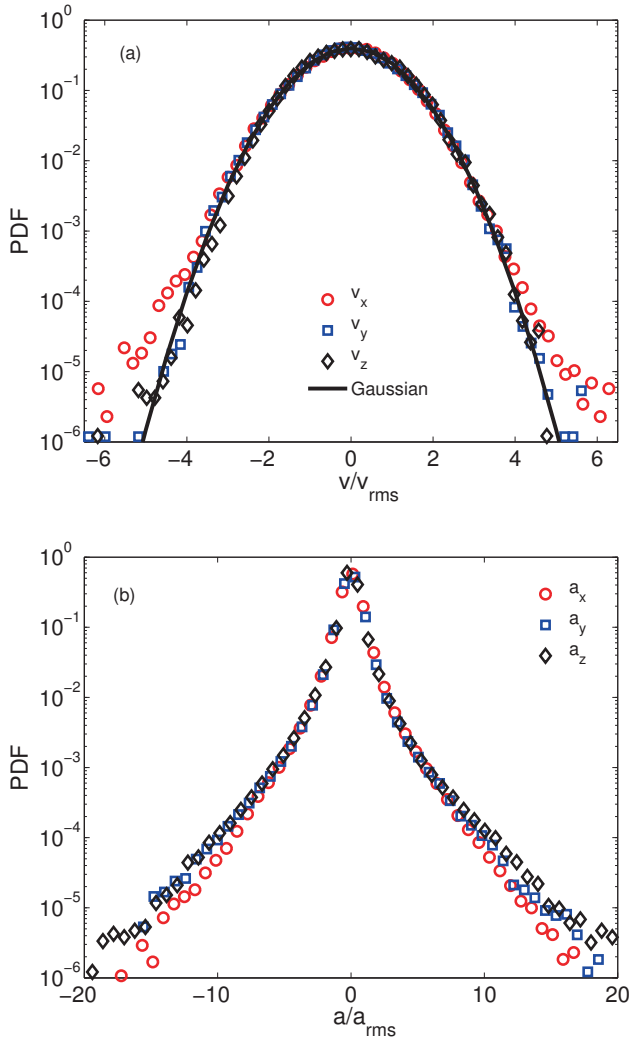

Figure 2.4: (a) PDFs of the three components of micro-bubble velocity at $\mathrm{Re}_\lambda = 195$. The three velocity component distributions are nearly Gaussian compared to the solid line that represents a Gaussian distribution. (b) PDFs of the three components of the normalized micro-bubble acceleration at $\mathrm{Re}_\lambda = 195$. The three components of the acceleration are strongly non-Gaussian, i.e. the tails of the distribution show high intermittency.

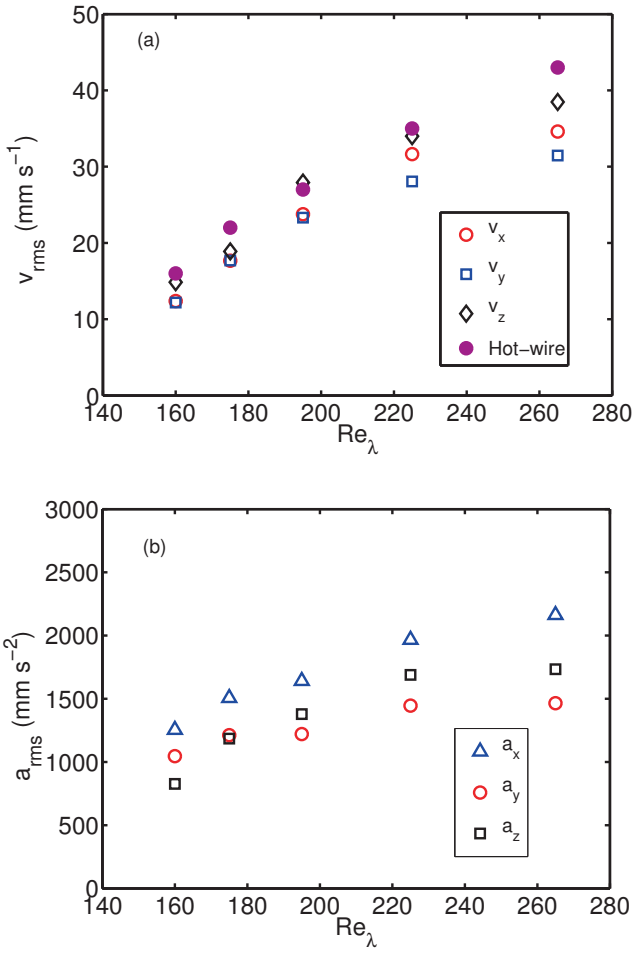

Figure 2.5: (a) r.m.s values of the three components of the micro-bubble velocity for all Re_λ, compared with the hot-wire probe measurements. (b) r.m.s values of the three components of the micro-bubble acceleration for all Re_λ.

$5\,a_{rms}$. We have observed the same trend for the higher Re_λ, whereas for smaller Re_λ, the components of the acceleration (a_x, a_y) in the plane perpendicular to the mean flow direction are not yet isotropic. These components have tails that are slightly narrower than the vertical component (a_z). The flow in the Twente Water Tunnel is not fully isotropic, as has been discussed in Poorte & Biesheuvel [25]. This slight anisotropy is visible in the PDFs, also in the a_x component in Figure 2.4b. In Figure 2.5b, we show the dependence of the acceleration r.m.s values on Re_λ. Again, there is an increasing trend with Re_λ and a visible anisotropy in the three components. In the discussion that follows, we will only present results of the vertical component z (mean flow direction) of the acceleration PDF.

In Figure 2.6, we present the PDFs of the micro-bubble acceleration for all the Re_λ covered in the present study. In order to improve the statistics of the data and obtain a better convergence around the tails, we show the positive part of the averaged PDF, i.e. $(f(a_z) + f(-a_z))/2$, where $f(a_z)$ is the PDF of the vertical component acceleration (a_z). Although the r.m.s of acceleration increases with Re_λ (Figure 2.5b), the acceleration PDFs, normalized by the r.m.s, collapse on top of each other for all Re_λ (see Figure 2.6). Here, we cannot see a clear dependence on Re_λ, but the flatness of these acceleration PDFs better reveals the dependence, and will be discussed in section 2.3.3.

First, we compare our micro-bubble results with experimental data of heavy [4] and tracer particles [3] under similar flow conditions (grid-generated turbulence with a mean flow). Ayyalasomayajula *et al.* [4] conducted experiments with heavy particles (water droplets) in a wind tunnel at St = 0.15 and Re_λ = 250, the corresponding results are shown in figure 2.6a. Subsequently, measurements of tracer particles were also made in the same facility with St = 0.01 and Re_λ = 250 (Ref. [3]) (also shown in figure 2.6a). We observe that the present micro-bubble acceleration PDF shows a higher intermittency than heavy and tracer particles at similar Re_λ and St.

In figure 2.6b, we compare the present data with experiments carried out in von Kármán flows. It is important to note the differences in the flow conditions between grid-generated turbulence and the turbulence generated in between counter-rotating disks. It is known that von Kármán flows have a large-scale anisotropy. Secondly, the confinement conditions are different. These differences could affect the Lagrangian dynamics [11]. Tracer particles in von Kármán flows at Re_λ=140 to 690 [1, 6] show a good agreement with our micro-bubble results for $|a_z/a_{z,rms}| \lesssim 15$ (see the Mordant *et al.* [6] fit in figure 2.6b). But beyond this value our micro-bubble acceleration PDFs are slightly less intermittent. Furthermore, a comparison with the experiments of Volk *et al.* [13] who measured micro-bubble acceleration in von Kármán flow at Re_λ = 850 and St=1.85 is presented in figure 2.6b. Unexpectedly, there is a good agreement

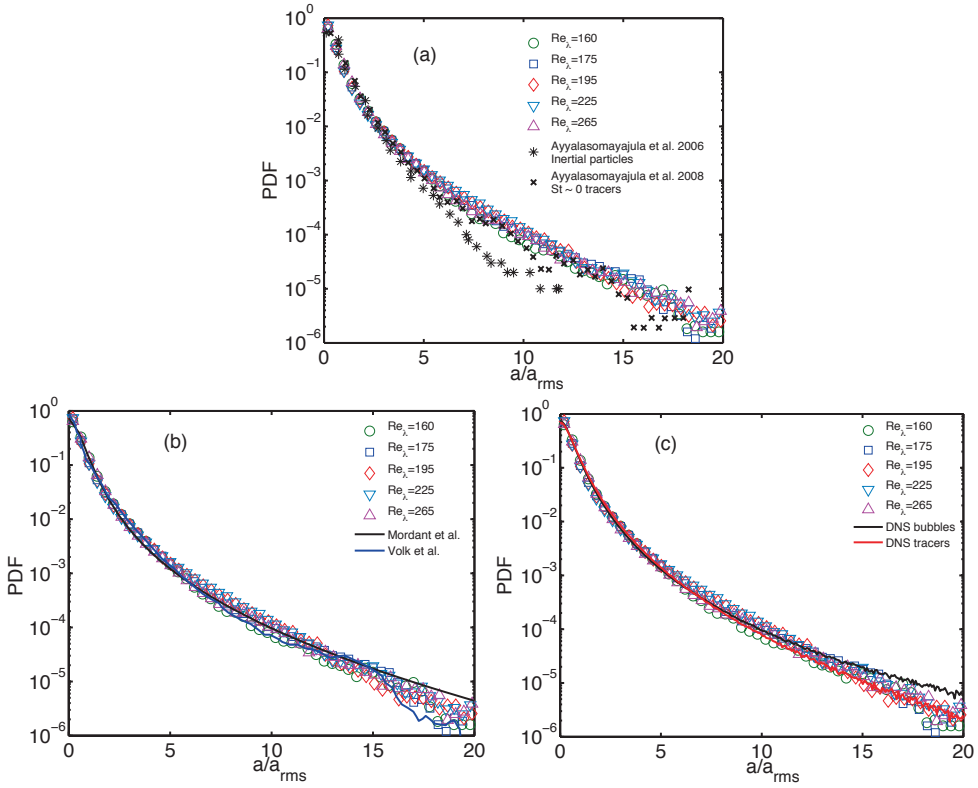

Figure 2.6: PDFs of the vertical component of the normalized micro-bubble acceleration. (a) Comparison with experiments under similar flow conditions (grid-generated turbulence in a wind-tunnel) at Re_λ = 250. Our results are shown with open symbols; stars are heavy particles [4] and black crosses represent tracer particles [3]. (b) Comparison with von Kármán flow results: fit for tracers at $\mathrm{Re}_\lambda = 140 - 690$ [1, 6] is the black line; bubbles at $\mathrm{Re}_\lambda = 850$ [12, 13] are shown with a blue line. (c) Comparison with DNS simulations for point particles at $\mathrm{Re}_\lambda = 180$ (from iCFDdatabase http://cfd.cineca.it): the red line indicates tracers and the black line bubbles.

between the two experiments with very different Re_λ, St, and flow conditions. This could just be a coincidence that both the results agree despite these differences. To arrive at a final conclusion on this issue, more systematic experiments need to be carried out in a wider Re_λ – St parameter space under our experimental conditions.

Figure 2.6c shows the comparison between the present micro-bubble acceleration results with the DNS data for point-like bubbles and tracers in homogeneous and isotropic turbulence at a similar Re_λ=180 and St = 0.1 (data obtained from iCFD-database http://cfd.cineca.it). The simulations considered one-way coupled point particles within a periodic cubic box of size $L = 2\pi$ and with a spatial resolution of 512^3 (for further details on the simulation see Ref. [15]). We observe that our experimental findings agree with both numerical bubbles and tracers when $|a_z/a_{z,rms}| \lesssim 15$ within experimental error. The experimental PDF is closer to the numerical tracers for $|a_z/a_{z,rms}| \gtrsim 15$. A possible reason for the better agreement between experimental micro-bubbles and DNS tracers could be the small St numbers O(0.01) in the present study. Another possible reason is the different flow conditions, in the experiments there is a strong mean flow which is absent in the numerics. In addition, several factors such as the lift force, buoyancy forces, and particle–particle interactions are ignored in the DNS [26]. We emphasize again that in the present chapter, the micro-bubble size is comparable to Kolmogorov scale, hence, we do not expect the finite size effects [17] to play an important role.

2.3.3 Flatness of the micro-bubble acceleration

In order to quantify the intermittency of the acceleration PDFs, statistical convergence of the data is necessary. The number of data points needed for this convergence is crucial, and previous studies have shown that it should at least be $\approx$ O(10^6) (see Refs. [1] and [4]). As shown in table 2.1, our measurements consist of at least 4.5×10^6 datapoints.

The intermittency of the PDFs of the micro-bubble acceleration can be quantified by studying the flatness F:

$$\text{flatness} = \mu_4/\sigma^4, \tag{2.4}$$

where μ_4 is the fourth moment and σ the r.m.s of the distribution. The flatness being a fourth order moment is strongly determined by the tails of the distribution, and hence convergence of the PDFs is required. Even though the number of datapoints used to calculate the PDFs in the present chapter is larger than O(10^6), full convergence has not yet been achieved to calculate directly the flatness from the distribution itself (the largest experimental datasets consist of $\approx$ O(10^8) datapoints [6], whereas for numerics this value can go up to $\approx$ O(10^9) [8]. Consequently, we fit the experimental

PDF to a stretched exponential distribution [6, 27] defined as:

$$f(x) = C\exp\left(\frac{-x^2}{\alpha^2(1+|\frac{\beta x}{\alpha}|^{\gamma})}\right), \tag{2.5}$$

In equation 2.5, $x = \mathrm{a}/\mathrm{a}_{rms}$ is the normalized micro-bubble acceleration, the fitting parameters are α, β and γ and C is a normalization constant. For this fitting procedure and in order to improve the convergence at the tails, we consider the positive part of the averaged PDF, as mentioned above in section 2.3.2.

Figure 2.7a shows the result of the fitting for the micro-bubble acceleration PDF at $\mathrm{Re}_\lambda = 195$. The stretched exponential fits the experimental PDF quite well because the three fitting parameters enable a fine adjustment. In the inset of figure 2.7a, we plot the fourth order moment $(\mathrm{a}/\mathrm{a}_{\mathrm{rms}})^4\mathrm{PDF}(\mathrm{a}/\mathrm{a}_{\mathrm{rms}})$ for the experimental acceleration measurement along with the fitted curve. This type of curve allows for a good convergence test [28]. At the tails of the distribution, convergence is nearly achieved, and the fitted curve nicely sits on top of the experimental data. We have observed a similar behavior for the other measurements at different Re_λ.

Next, we calculate the flatness of the fitted acceleration PDFs as a function of Re_λ, as shown in Figure 2.7b. The flatness is determined directly from the fitted stretched exponential functional for all Re_λ. The errorbars are obtained by finding the difference between the flatness values for half and the entire acceleration datapoints. Figure 2.7c shows that the flatness values of the micro-bubble acceleration PDFs increase in the Re_λ range 160-225 consistent with the experimental results of Voth *et al.*[1] for tracer particles and the numerical results of Ishihara *et al.*[2] for fluid particles. For the highest Re_λ, we have less statistics compared to the other cases as the mean flow speed is the fastest. This might be the reason for the decrease (underestimation) in the flatness value of our data point at $\mathrm{Re}_\lambda = 265$. Clearly, from the collection of all data (Figure 2.7c) one would not expect such a decrease.

2.3.4 Autocorrelation functions

We now present results on the Lagrangian autocorrelation function of the micro-bubble acceleration. In figure 2.8 we compare the autocorrelation for the three components of the acceleration at Re_λ=195, using a time lag normalized with τ_η. We find that the three acceleration components correlate in a similar manner. This nearly isotropic behavior was also found for the other measurements at different Re_λ.

Figure 2.9a shows the autocorrelation of a_z for different Re_λ. It is clear that the microbubble's acceleration correlates for longer times as Re_λ increases. The acceleration autocorrelation function drops to zero rapidly, and the zero-crossing point has

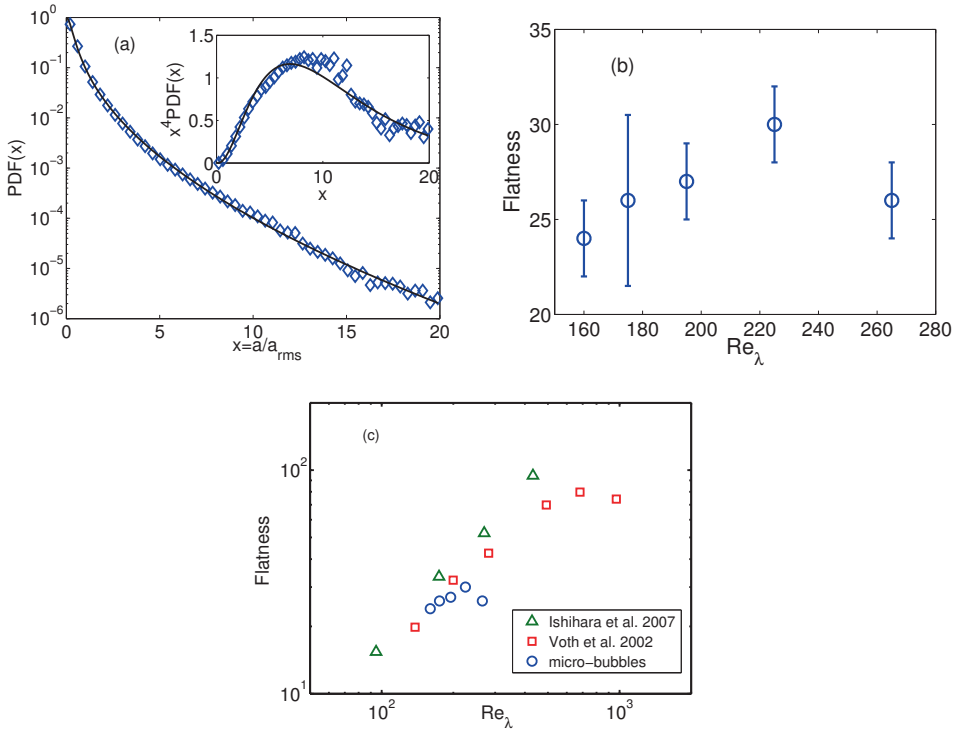

Figure 2.7: (a) PDF of the vertical component of the micro-bubble acceleration at Re_λ=195. Open squares are the experimental data, solid line is the fitted stretched exponential function. The insert shows the plot of the fourth order moment $x^4 PDF(x)$ for experimental data and fit. (b) The flatness value of the fitted PDFs of micro-bubble acceleration as a function of Re_λ. (c) The flatness values versus the Reynolds number. Comparison with Voth *et al.* [1] and Ishihara *et al.* [2] reveals that the present micro-bubble trend agrees well with the data in the literature, at least till $Re_\lambda = 225$.

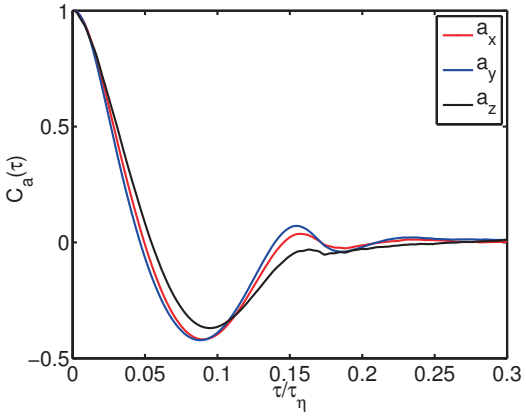

Figure 2.8: Autocorrelation function of the three components of the micro-bubble acceleration at Re_λ=195. The acceleration autocorrelation of the micro-bubbles is nearly isotropic. The time lag is normalized with the Kolmogorov time scale τ_η.

small values: $< 0.1\tau_\eta$. Voth *et al.* [1] and Mordant *et al.* [7] reported values of around $2.2\tau_\eta$ in their experiments with tracers in von Kármán flows at high turbulence intensities ($\mathrm{Re}_\lambda > 690$). The value of $2.2\tau_\eta$ was first found from DNS by Yeung *et al.* [29]. Volk *et al.* [12] performed both micro-bubble and tracer experiments in a von Kármán apparatus, and found that the decorrelation of the microbubbles is smaller than that of tracers at a given Re_λ. We do not yet know the exact reason for the large disparity between $2.2\tau_\eta$ for the fluid particles compared to $0.1\tau_\eta$ for the present micro-bubbles. One possible reason is that our flow conditions are different as we have a strong mean flow.

We study the time at which the autocorrelation function drops to zero for different Re_λ by defining the decorrelation time as:

$$T_D = \int_0^{\tau_0} C_a(\tau) d\tau, \quad \text{with} \quad C_a(\tau_0) = 0,$$

where C_a is the acceleration autocorrelation function. T_D represents the characteristic time for the evolution of the micro-bubble response to changes in the flow conditions. Figure 2.9b shows the dependence of T_D/τ_η on Re_λ for the three components of the micro-bubble acceleration. We observe that T_D/τ_η increases with Re_λ, and that the autocorrelation functions are nearly isotropic as evidenced by the very similar T_D/τ_η values for the different components. In the inset of figure 2.9b, the decorrelation time T_D/τ_η as obtained by Volk *et al.* [12] at Re_λ=850 agrees well with our increasing trend of the decorrelation time with Re_λ. We fit our experimental

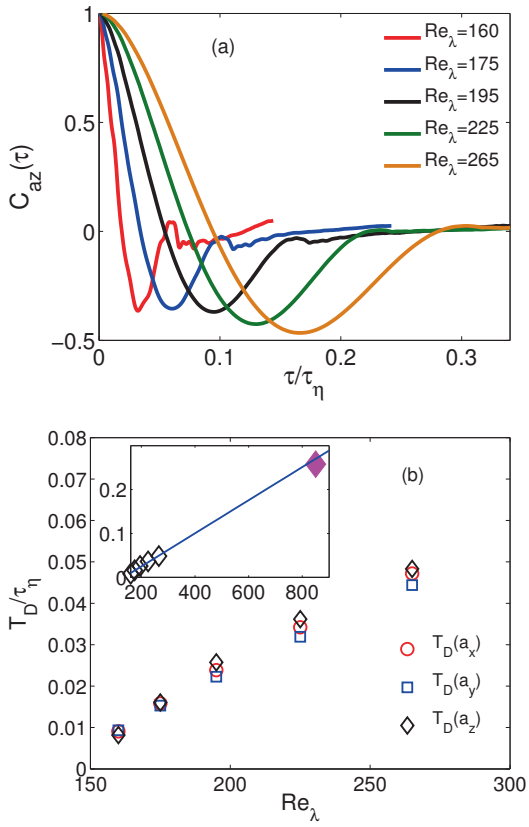

Figure 2.9: (a) Autocorrelation function of the vertical component of the micro-bubble acceleration for the different Re_λ measured. The correlation of the micro-bubble acceleration persists longer with increasing Reynolds number. (b) The decorrelation time T_D/τ_η of the autocorrelation function for the three components of the micro-bubble acceleration as a function of Re_λ. The decorrelation time increases with the turbulent intensity. In the inset, we show also the result of Volk *et al.* [12] at a very high Re_λ=850 (♦), their experimental point agrees with the trend of increasing decorrelation time with turbulent intensity. The linear fit obtained with our experimental data extrapolates a value of $T_D/\tau_\eta = 0.27$ at Re_λ=850, which is slightly higher than their experimental value of $T_D/\tau_\eta = 0.25$.

data of the decorrelation time of a_z to a linear relation $T_D/\tau_\eta = 0.00038\mathrm{Re}_\lambda - 0.051$ that is shown in the inset of figure 2.9b as a solid line. Evaluating these relations at Re_λ=850 gives $T_D/\tau_\eta = 0.27$, which agrees well with their experimental value of

$T_D/\tau_\eta = 0.258$ [12]. More experiments are needed to fill the gap of Re_λ. Very recently, Volk *et al.* [16] found an increase of T_D/τ_η with Re_λ for a fixed particle size, just as we find in our micro-bubble experiments.

2.4 Conclusion

We have presented experimental results on the Lagrangian statistics of micro-bubble velocity and acceleration in homogeneous isotropic turbulence. Three-dimensional PTV was employed to obtain the micro-bubble trajectories. The PDFs of micro-bubble velocity closely follow a Gaussian distribution with flatness $F \approx 3$, independent of Re_λ. But the acceleration PDFs are highly non-Gaussian with intermittent tails. Although the acceleration PDFs themselves do not show a clear dependence on Re_λ, the flatness values reveal a clear trend. We fit the experimental acceleration PDFs to a stretched exponential function and estimate the flatness based on the fitting. The flatness values were found to be in the range of 23–30 and show an increasing trend with Re_λ. This trend is consistent with previous experimental [1] and numerical [2] results.

A comparison of our results with experiments in von Kármán flows [1, 6, 12, 13] suggest that the present micro-bubble acceleration PDF is similar to tracers and bubbles (in von Kármán flows) for very different Re_λ. However, there are significant differences in the flow conditions between the two experimental systems. Therefore, it is more relevant to compare our results with previous investigations in similar flow conditions, i.e. grid-generated turbulence. We find that the acceleration PDFs of our micro-bubbles are more intermittent as compared to heavy and tracer particles in wind tunnel experiments at similar St and Re_λ [3, 4].

Compared to DNS simulations in the point particle limit, our micro-bubble acceleration PDFs show a reasonable agreement with both numerical tracers and bubbles, but in the tails our data has a better match with numerical tracers. One possible reason is the differences in flow conditions between the experiments and numerics. Another possibility is that the St in our experiments are small (0.02—0.09). It will be interesting to study the acceleration statistics of finite-sized bubbles at large St in turbulent flows.

We also calculate the autocorrelation function of the micro-bubble acceleration, and observed that the decorrelation time increases with Re_λ. This finding is consistent with other experimental investigations [12, 16] at very high Reynolds number. More experimental data is needed to fill the gap of Re_λ in order to further study the scaling behavior.

References

[1] G. Voth, A. La Porta, A. M. Crawford, J. Alexander, and E. Bodenschatz, *Measurement of particle accelerations in fully developed turbulence*, J. Fluid Mech. **469**, 121 (2002).

[2] T. Ishihara, Y. Kaneda, M. Yokokawa, K. Itakura, and A. Uno, *Small-scale statistics in high-resolution direct numerical simulation of turbulence: Reynolds number dependence of one-point velocity gradient statistics*, J. Fluid Mech. **592**, 335 (2007).

[3] S. Ayyalasomayajula, Z. Warhaft, and L. R. Collins, *Modeling inertial particle acceleration statistics in isotropic turbulence*, Phys. Fluids. **20**, 095104 (2008).

[4] S. Ayyalasomayajula, A. Gylfason, L. R. Collins, E. Bodenschatz, and Z. Warhaft, *Lagrangian Measurements of Inertial Particle Accelerations in Grid Generated Wind Tunnel Turbulence*, Phys. Rev. Lett. **97**, 144507 (2006).

[5] F. Toschi and E. Bodenschatz, *Lagrangian properties of particles in turbulence*, Annu. Rev. Fluid Mech. **41**, 375 (2009).

[6] N. Mordant, A. M. Crawford, and E. Bodenschatz, *Experimental Lagrangian acceleration probability density function measurement*, Physica D **193**, 245 (2004).

[7] N. Mordant, A. M. Crawford, and E. Bodenschatz, *Three-Dimensional Structure of the Lagrangian Acceleration in Turbulent Flows*, Phys. Rev. Lett. **93**, 214501 (2004).

[8] L. Biferale, G. Boffetta, A. Celani, B. J. Devenish, A. Lanotte, and F. Toschi, *Multifractal statistics of lagrangian velocity and acceleration in turbulence*, Phys. Rev. Lett. **93**, 064502 (2004).

[9] I. Mazzitelli and D. Lohse, *Lagrangian statistics for fluid particles and bubbles in turbulence*, New J. Phys. **6**, 203 (2004).

[10] F. Toschi, L. Biferale, G. Boffetta, A. Celani, B. J. Devenish, and A. Lanotte, *Acceleration and vortex filaments in turbulence*, J. Turb. **6**, 15 (2005).

[11] N. M. Qureshi, U. Arrieta, C. Baudet, A. Cartellier, Y. Gagne, and M. Bourgoin, *Acceleration statistics of inertial particles in turbulent flow*, Eur. Phys. J. B **66**, 531 (2008).

[12] R. Volk, E. Calzavarini, G. Verhille, D. Lohse, N. Mordant, J.-F. Pinton, and F. Toschi, *Acceleration of heavy and light particles in turbulence: Comparison between experiments and direct numerical simulations*, Physica D **237**, 2084 (2008).

[13] R. Volk, N. Mordant, G. Verhille, and J.-F. Pinton, *Laser Doppler measurement of inertial particle and bubble accelerations in turbulence*, Europhys. Lett. **81**, 34002 (2008).

[14] M. Gibert, H. Xu, and E. Bodenschatz, *Inertial effects on two-particle relative dispersion in turbulent flows*, Europhys. Lett. **90**, 64005 (2010).

[15] J. Bec, L. Biferale, G. Boffetta, A. Celani, M. Cencini, A. Lanotte, S. Musacchio, and F. Toschi, *Acceleration statistics of heavy particles in turbulence*, J. Fluid Mech. **550**, 349 (2006).

[16] R. Volk, E. Calzavarini, E. Leveque, and J.-F. Pinton, *Dynamics of inertial particles in a turbulent von Kármán flow*, J. Fluid Mech. **668**, 223 (2011).

[17] E. Calzavarini, R. Volk, M. Bourgoin, E. Leveque, J.-F. Pinton, and F. Toschi, *Acceleration statistics of finite-sized particles in turbulent flow: the role of Faxèn forces*, J. Fluid Mech. **630**, 179 (2009).

[18] R. D. Brown, Z. Warhaft, and G. A. Voth, *Acceleration Statistics of Neutrally Buoyant Spherical Particles in Intense Turbulence*, Phys. Rev. Lett. **103**, 194501 (2009).

[19] J. Rensen, S. Luther, and D. Lohse, *The effects of bubbles on developed turbulence*, J. Fluid Mech. **538**, 153 (2005).

[20] J. Martínez Mercado, D. Chehata Gómez, D. van Gils, C. Sun, and D. Lohse, *On bubble clustering and energy spectra in pseudo-turbulence*, J. Fluid Mech. **650**, 287 (2010).

[21] K. R. Sreenivasan, *On the universality of the Kolmogorov constant*, Phys. Fluids **7**, 2778 (1995).

[22] K. Hoyer, M. Holzner, B. Lüthi, M. Guala, A. Liberzon, and W. Kinzelbach, *3D Scanning Particle Tracking velocimetry*, Exp. in Fluids **39**, 923 (2005).

[23] Y. Tagawa, J. Martínez Mercado, V. N. Prakash, E. Calzavarini, C. Sun, and D. Lohse, *Three-dimensional Lagrangian Voronoi Analysis for clustering of particles and bubbles in turbulence*, J. Fluid Mech. **693**, 201 (2012).

[24] B. Lüthi, A. Tsinober, and W. Kinzelbach, *Lagrangian measurement of vorticity dynamics in turbulent flow*, J. Fluid Mech. **528**, 87 (2005).

[25] R. Poorte and A. Biesheuvel, *Experiments on the motion of gas bubbles in turbulence generated by an active grid*, J. Fluid Mech. **461**, 127 (2002).

[26] E. Calzavarini, M. Kerscher, D. Lohse, and F. Toschi, *Dimensionality and morphology of particle and bubble clusters in turbulent flow*, J. Fluid Mech. **607**, 13 (2008).

[27] S. Grossman and D. Lohse, *Intermittency exponents*, Europhys. Lett. **21**, 201 (1993).

[28] F. Belin, P. Tabeling, and H. Willaime, *Exponents of the structure function in a low temperature helium experiment*, Physica D **93**, 52 (1996).

[29] P. K. Yeung and S. B. Pope, *Lagrangian statistics from direct numerical numerical simulations of isotropic turbulence*, J. Fluid Mech. **207**, 531 (1989).

3

How gravity and size affect the acceleration statistics of bubbles in turbulence *

We report the results of the first systematic Lagrangian experimental investigation in a previously unexplored regime of very light (air bubbles in water) and large particles ($D/\eta >> 1$) in turbulence. Using a traversing camera setup and particle tracking, we study the Lagrangian acceleration statistics of ~ 3 mm diameter (D) bubbles in a water tunnel with nearly homogeneous and isotropic turbulence generated by an active-grid. The Reynolds number (Re_λ) is varied from 145 to 230, resulting in size ratios, D/η in the range of 7.3–12.5, where η is the Kolmogorov length scale. The experiments reveal that gravity increases the acceleration variance and reduces the intermittency of the PDF in the vertical direction. Once the gravity offset is subtracted, the variances of both the horizontal and vertical acceleration components are about 5 ± 2 times larger than the one measured in the same flow for fluid tracers. Moreover, for these light particles, the experimental acceleration PDF shows a substantial reduction in intermittency at growing size ratios, in contrast to neutrally buoyant or heavy particles. All these results are closely matched by numerical simulations of finite-size bubbles with the Faxén corrections.

*Published as: Vivek N. Prakash, Y. Tagawa, E. Calzavarini, J. M. Mercado, F. Toschi, D. Lohse, and C. Sun, How gravity and size affect the acceleration statistics of bubbles in turbulence, New J. Phys. 14, 105017, (2012).

3.1 Introduction

Suspensions of particulate materials, drops or bubbles carried by vigorously turbulent flows occur frequently both in the realm of natural phenomena (e.g. cloud formation) and in industrial applications (e.g. combustion in engines). In order to quantify the statistical properties of such suspensions a prototype problem is often considered: the one of a dilute suspension of spherical particles in incompressible, statistically homogeneous and isotropic turbulence [1–3]. In this simple form the problem is defined by a set of three dimensionless parameters $[Re_\lambda, \Gamma, \Xi]$, respectively the Reynolds number based on the Taylor scale of the carrying flow, the particle to fluid mass density ratio ($\Gamma \equiv \rho_p/\rho_f$) and the particle to dissipative-length ratio ($\Xi \equiv D/\eta$). Interesting theoretical questions concern how far the particle statistical properties (e.g. moments, probability density functions (PDFs), correlations) of position, velocity and acceleration depart from the Lagrangian properties of the fluid. The goal is to understand how such observables vary as a function of the control parameters.

Numerical studies have attempted to see how closely the approximate equations of Lagrangian dynamics – which were known for a long time – are able to capture the dynamics. Since full numerics (e.g. physalis [4], front tracking [5]) are too expensive for high Re_λ, most simulations use a point particle (PP) model [6–8], also known as the Maxey-Riley-Gatignol model [9, 10]. In the real world, there are many situations where the particle size is larger than the Kolmogorov length scale of turbulence ($\Xi \gg 1$). Therefore, a considerable body of recent work ([11–17]) has been dedicated to the characterization of these so-called *finite-sized* particles. Numerical simulations with Faxén corrections (FC) to the point-particle approach [14] correctly capture two important features from the experimental data for neutrally buoyant and heavy finite-sized particles [11–13, 15–17]: the acceleration PDF of the finite-size particles in general show less intermittency than those of fluid tracers; and their acceleration variance decreases with increasing size ratio. However, for light particles ($\Gamma < 1$), the Faxén corrected numerics [14] remarkably indicate an opposite trend for the acceleration statistics at growing Ξ: an initial increase of acceleration variance and intermittency, followed by a decrease. These predictions for light particles are awaiting experimental verification.

However, these experiments are highly challenging in terms of the infrastructure needed, techniques and analysis, but are of great importance for a fundamental understanding of particles in turbulence.

In this chapter, we present the first systematic experimental investigation in the regime ($\Gamma \ll 1, \Xi > 1$) of the parameter-space, i.e. very light and large particles (see Fig. 3.1 for a summary of all the currently available measurements). For such an investigation, we use air bubbles, which are dispersed in a turbulent water flow.

We track these bubbles using a traversing camera system which can perform two-dimensional (2D) recordings of the vertical and one horizontal component of the bubble trajectories. The experiments are compared to numerical simulations based on the particle Lagrangian equations with Faxén correction [14]. We also experimentally study the effects of gravity, as it could be important at lower Re_λ, and very few numerical studies [18] have taken gravity into account.

The chapter is organized as follows: in section 3.2, we describe in detail the experimental setup (sec. 3.2.1), the bubble deformability and size distribution (sec. 3.2.2). Next, we present results on the velocity statistics (sec. 3.3) and the acceleration statistics (sec. 3.4). The effects of gravity and size on the acceleration statistics are discussed in sections (sec. 3.4.1) and (sec. 3.4.2), followed by the conclusions in section 3.5.

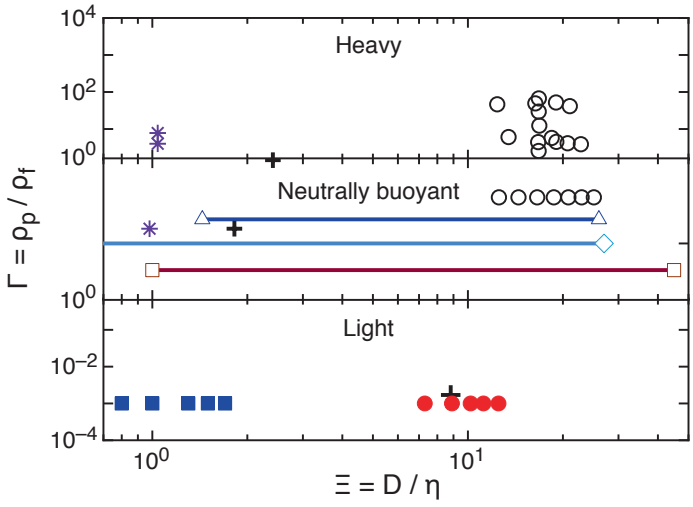

Figure 3.1: Parameter space of the density ratio versus size ratio for particles in turbulence, from data available in literature: △ - Voth *et al.* [11], ○ - Qureshi *et al.* [13], + Volk *et al.* [19], ◇ Brown *et al.* [15], ∗ Gibert *et al.* [16], □ Volk *et al.* [17], ■ Martinez *et al.* [20], • Present work. Majority of previous studies have focused on $\Gamma \geq 1$, here we explore the $\Gamma \ll 1$ case.

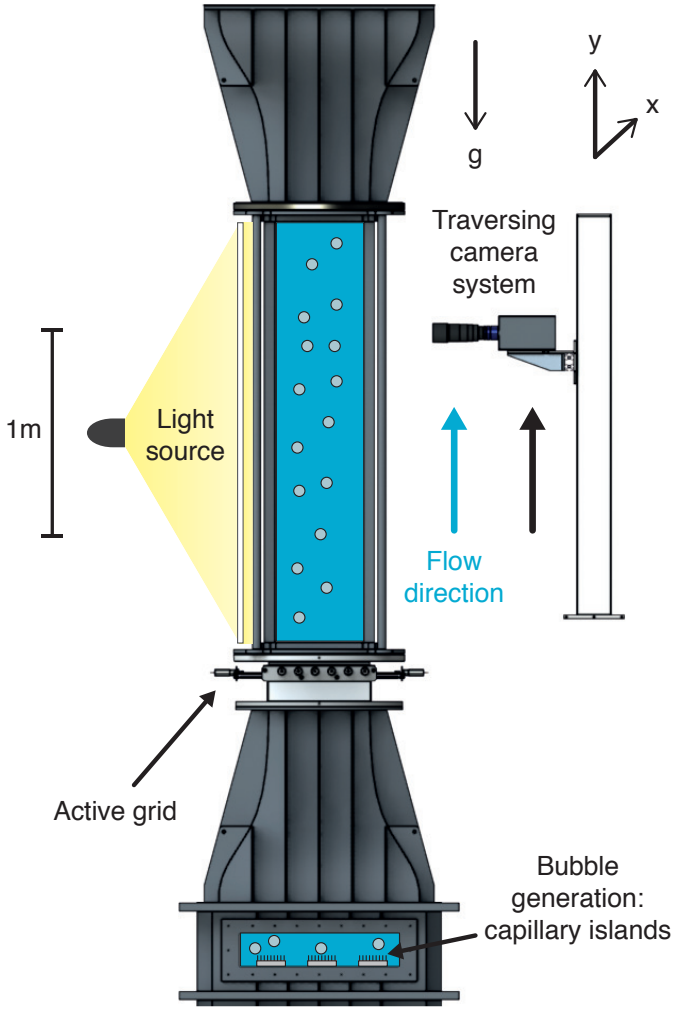

Figure 3.2: The Twente Water Tunnel facility: vertical water tunnel with nearly homogeneous and isotropic turbulence generated by an active-grid. Bubbles are dispersed from below through capillary islands and the flow is in the upward direction. The camera moves upward at preset speeds, along with the bubbles, allowing the measurement of long-duration trajectories.

3.2 Experiments and analysis

3.2.1 Experimental setup

In our experiments, air bubbles in water, $\Gamma \approx 10^{-3}$, are dispersed in a turbulent flow in the 8*m* high Twente Water Tunnel (TWT) facility (see Fig. 3.2). Nearly homogeneous and isotropic turbulence is generated by the flow of water through an active grid [21]. An optically transparent measurement section of dimensions $2\times0.45\times0.45$ m^3 is located downstream of the active grid. We recently reported results on ~ 0.3 *mm* sized bubbles ([20, 22]) using the same experimental facility (see also [23, 24]). Here, one important modification is made: the position of the active grid is switched from the position on top of the measurement section to its bottom. Furthermore, the direction of the water flow through the active grid is now upwards. The bubbles are generated by blowing air through capillary islands (diameter 500 μm) placed below the active grid. The bubbles rise through the measurement section along with the imposed water flow and escape through an open vent on top of the water tunnel. A surfactant (Triton X-100) is added to the tap water to reduce the bubble deformability [25] (more details follow in section 3.2.2). Re_λ is varied from 145–230 by changing the mean flow speed of water in the tunnel. The flow characterization is done using a hot-film probe placed in the center of the measurement volume [20]. The 2D Lagrangian particle tracking experiments are carried out using a high-speed camera (Photron SA1.1) at an image acquisition rate of 5000 frames per second (fps) with a resolution of 768×768 pixels. The camera is focused on a 1-2 cm thick plane in the middle of the measurement section and the illumination is provided from the opposite side by a halogen light source placed behind a diffusive plate. The camera is mounted on a traverse system (Aerotech L-ATS62150 linear stage) which enables precise movement in the vertical direction at preset velocities.

The detection of the bubble centers in the images is a non-trivial task because the bubbles often overlap or go out of focus (see Fig. 3.3). However, the circular Hough transform method [26] is successfully used to detect more than 90% of the bubbles (which are in focus) in the images. The Hough transform is a technique for extracting features in images, and has been used widely in the field of computer vision and digital image processing. During image processing, edge-detection algorithms are used to extract attributes from images, and these are followed by linking procedures (such as the Hough transform) to assemble edge pixels into useable edges [27]. Initially, the technique was used for line detection and then extended to circles and ellipses, and eventually to arbitrary shapes [28].

A 2D Particle Tracking code is used to obtain the bubble trajectories over time. The data processing approach is the same as in Martinez *et al.* [20]. The fitting win-

dow lengths (N) of the trajectory smoothing for the micro-bubble experiments (see Ref. [20] for more details) and present experiments have been chosen to be consistent. The fitting window length is $N = 15$ for the present experiments at 5000 fps acquisition rate, and $N = 30$ for the micro-bubble experiments at 10,000 fps acquisition rate.

3.2.2 Bubble deformability and size distribution

A surfactant (Triton X-100) is added to the tap water to reduce the bubble deformability. The small amount of surfactant (< 1 ppm) used in the present experiments is much below the critical micelle concentration, so the change in flow properties is negligible [29]. Although the addition of surfactant reduces the surface tension by a few percent, it leads to another competing effect, namely the suppression of bubble coalescence at the source of injection. This second effect is more dominant and as a result we see a reduction of the bubble size [25].

Figure 3.3 shows the difference between bubbles in tap water and in a surfactant solution. We clearly see a big difference in the shapes and sizes of the bubbles. The deformation is greatly reduced in the presence of surfactant, thanks to the smaller size. Nonetheless, in Fig. 3.3, the bubbles still appear to be deformed and anisotropic, but the effect is much less than without surfactants: the addition of surfactants leads to a *reduced* deformability of the bubbles and not to a perfect spherical shape. The principal-axis deformation ratios, defined as b/a, where a, b are the major and minor axis lengths of the best-fitting ellipse, are more than $1/2$. For example, the deformation ratio in the case of $\mathrm{Re}_\lambda = 170$ ($\Xi = 8.9$), is 0.75 ± 0.15 - which indicates small deformability, approaching a circle. The images in Fig. 3.3 are instantaneous snapshots from the experiments. It must be noted that the deformation of real bubbles is strongly time dependent, and the addition of surfactant significantly reduces this deformation over time. Thus, the addition of the surfactant renders the images amenable to processing, which is otherwise a nearly impossible task.

The bubble diameter has a weak dependence on Re_λ, as shown in Fig. 3.4. We select the peak values of the distribution as the characteristic bubble diameter; $D = 3.15, 2.90, 2.70, 2.55, 2.50$ mm (with absolute deviations $\sim \pm 0.3$ mm, see Fig. 3.4) at $\mathrm{Re}_\lambda = 145$, 170, 195, 215, and 230, respectively. This variation in Re_λ changes the Kolmogorov length scale (η), and the corresponding size ratios are $\Xi = 7.3$, 8.9, 10.2, 11.2, and 12.5.

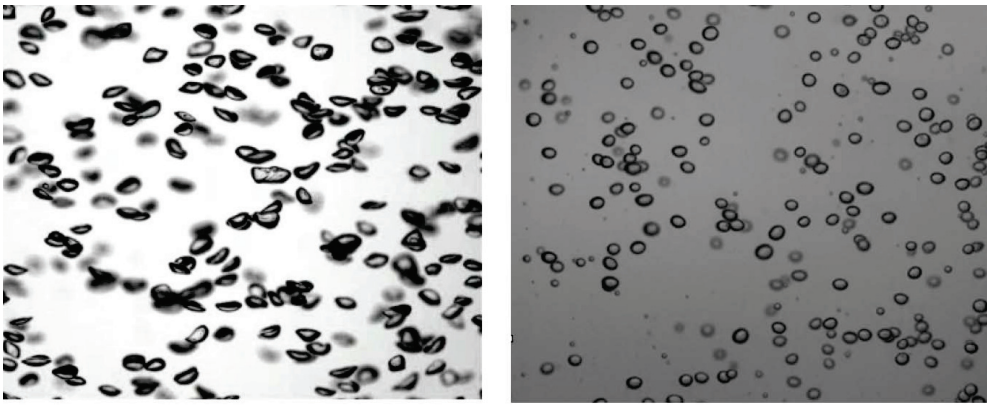

Figure 3.3: Left panel: rising bubbles of diameters $\sim 5mm$ in tap water. Right panel: bubbles of diameters $\sim 3mm$ in surfactant solution (with < 1 ppm Triton X-100).

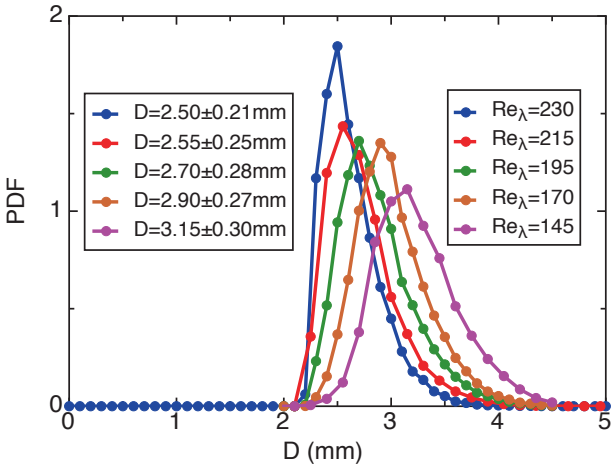

Figure 3.4: Distribution function of bubble diameters, D, at different Re_λ.

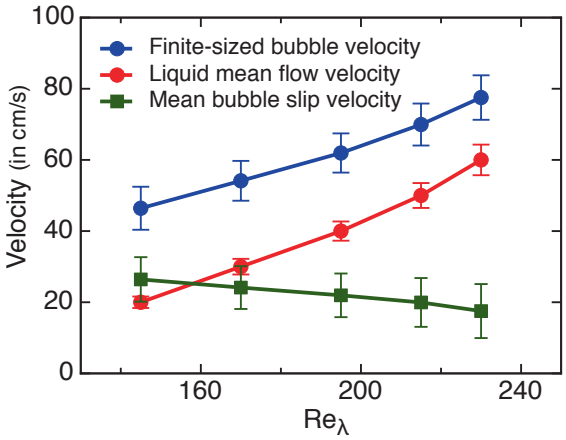

Figure 3.5: Finite-sized bubble slip velocity at different Re_λ.

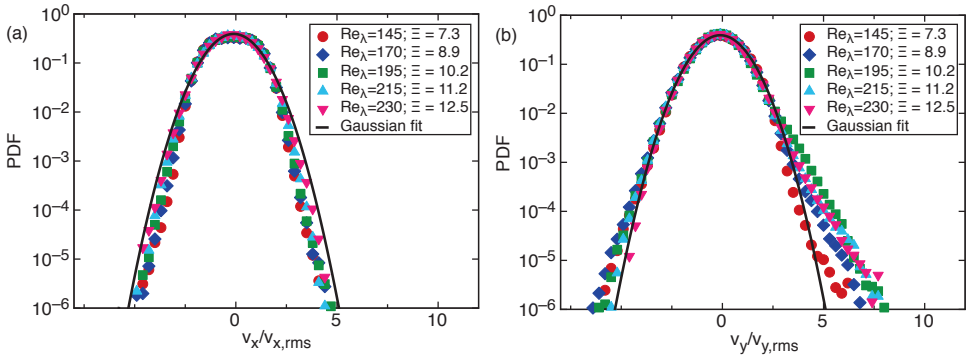

Figure 3.6: Velocity PDFs of the finite-sized bubbles at different Re_λ (and Ξ), (a) horizontal component, v_x (b) vertical component, v_y. The solid line in (a) and (b) represents a Gaussian distribution fit. The velocity PDF in (a) is mostly sub-Gaussian and in (b) we see more intermittency than a Gaussian profile.

3.3 Results - Velocity Statistics

In the present experiments, the bubble motion and liquid mean flow are both upwards. The terminal velocity of the ~ 3 mm bubbles in the absence of a liquid mean flow (still liquid) is determined from our experiments to be 25 cm s^{-1}. In the presence of a liquid mean flow, the bubbles attain their terminal velocity and then feel the turbulence of the surrounding liquid flow. In Fig. 3.5 we show the actual mean rise velocities of the bubbles (measured from the present experiments) compared to the liquid mean flow speeds. The bubbles experience a so-called 'slip' and are able to rise with velocities higher than the liquid mean flow. We quantify this 'mean bubble slip velocity' by defining it as the difference between the bubble rise velocity and the liquid mean flow velocity. The variation of this mean slip velocity with Re_λ is shown in Fig. 3.5. We see a decrease of the mean bubble slip velocity with increase in Re_λ. This decreasing trend might be due to the decreasing bubble size at higher Re_λ.

We now present here results on the probability distribution functions (PDFs) of the finite-sized bubble velocity obtained from the present experiments. Fig.3.6(a) and (b) show the PDF of the horizontal (x) and vertical (y) components of the normalized bubble velocity at the different Re_λ (and Ξ) covered in the present study. We observe that the x-component velocity distributions (Fig. 3.6(a)) follow sub-Gaussian statistics (flatness values: $2.27 - 2.78$) and the y-component velocity distributions (Fig. 3.6(b)) show a slightly higher intermittency compared to the Gaussian profile (flatness values: $2.89 - 3.77$). The vertical component velocity distributions are also asymmetric, owing to the effects of gravity. In previous experiments on finite-sized neutrally buoyant particles in turbulent von Kármán flows, Volk *et al.* [17] have obtained sub-Gaussian velocity distributions with flatness around $2.4-2.6$, but in the past, Gaussian-type flatness values ($2.8-3.2$) have also been reported [11]. The reason for the deviations of the velocity distributions from Gaussianity is still an open question.

3.4 Results - Acceleration statistics

3.4.1 Acceleration statistics: Gravity effect

We first address the effect of gravity on the acceleration statistics. Since the buoyancy is proportional to bubble volume, while the laminar viscous drag grows with the linear size of the bubble, it is clear that for growing bubble sizes and fixed turbulence intensity (growing Ξ), buoyancy at some point shall dominate. The opposite is true for the case of fixed bubble size but increasing Reynolds numbers (again growing Ξ) in our experiments, where buoyancy loses its dominance at higher Re_λ. In summary,

it is acceptable to neglect the buoyancy force only for small bubbles $\Xi \lesssim 1$ [20], or for large Re_λ, as we find later.

One may expect that the buoyancy force will produce *asymmetry* on the vertical component statistics because buoyancy will add up to the upward acceleration events and will subtract from the downward events. However, we find that the asymmetry is almost negligible. Firstly, we find that the mean value of vertical component of acceleration (y) is essentially zero, as it is for the horizontal one (x): $\langle a_x \rangle \simeq \langle a_y \rangle = 0 \pm 0.2g$, where g is the acceleration due to gravity. Secondly, we observe that the probability density function (PDF) shape is only very weakly asymmetric; we indeed estimate the skewness, $S(a_i) \equiv \langle a_i^3 \rangle / \langle a_i^2 \rangle^{3/2}$, and find $|S(a_x)| \leq 0.01$ and $|S(a_y)| \leq 0.1$. The skewness is comparable to the values found for $\Xi < 2$ bubbles (from now on called microbubbles) studied in the same setup [20]. We can conclude that if any asymmetry is present it must be very weak.

The buoyancy force, however, produces a robust *anisotropy*: different statistics for the vertical and the horizontal acceleration components. This influence of gravity is clearly visible in the second statistical moments of acceleration, shown in Fig 3.7(a), where the variance $\langle a_i^2 \rangle$ is plotted. We find that $\langle a_y^2 \rangle \gg \langle a_x^2 \rangle$ for all $\Xi > 7.3$ bubbles, while from the same figure it is evident that microbubbles have much closer variance values for the three Cartesian components. If one calls a_y' the vertical acceleration component in absence of gravity and assumes that $\langle a_y^2 \rangle = \langle (a_y' - g)^2 \rangle$, one gets $\langle a_y'^2 \rangle = \langle a_y^2 \rangle - g^2$, since $\langle a_y' \rangle = 0$ because of isotropy. As can be seen from figure 3.7(a), this produces a reasonable collapse of the x-y data $\langle a_y^2 \rangle - g^2 \simeq \langle a_x^2 \rangle$. We emphasize that the collapse observed for the second order moment is non-trivial. It means that the statistical effect of gravity seems to be additive on the vertical direction with no effect on the horizontal component. An immediate consequence is that the effect of hydrodynamic forces coupling different Cartesian directions, as for example the lift force, turns out to be unimportant here.

As mentioned above, we have found that the acceleration variance $\left\langle a_y^2 \right\rangle$ in the vertical direction is augmented by an offset (or a correction factor) that depends on g^2. Although we have found that the offset of $\sim g^2$ seems to work well for the present finite-sized bubbles, we do not yet have a physical understanding of the origin of this correction. When one examines the equations governing the motion of bubbles in a turbulent flow (Maxey-Riley-Gatignol equations) [9, 10] including gravity; the corresponding acceleration variance offset would then be $\sim 4g^2$, which does not work for the present data. Clearly, there seems to be a complex interplay between gravity and inertia, and more experimental and numerical work is needed before we can arrive at solid conclusion on the gravity correction factor. These corrections will be explored in detail in future work.

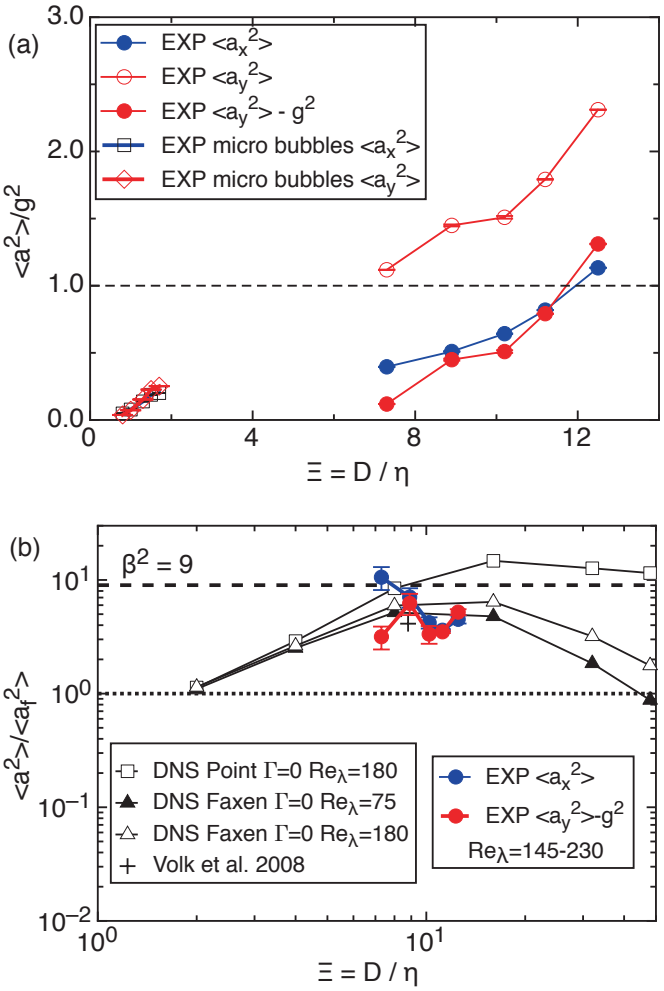

Figure 3.7: (a) The single-component acceleration variance normalized by the gravitational acceleration for large bubbles and for micro-bubbles [20]. (b) The normalized acceleration variance versus the size ratio. Legend : The present large bubble results (●) are represented with errorbars, along with a gravity offset for the vertical component a_y. (□): PP DNS of bubbles [14] (△ & ▲): bubbles from DNS with FCs [14], (+) : single experimental point for bubbles [19].

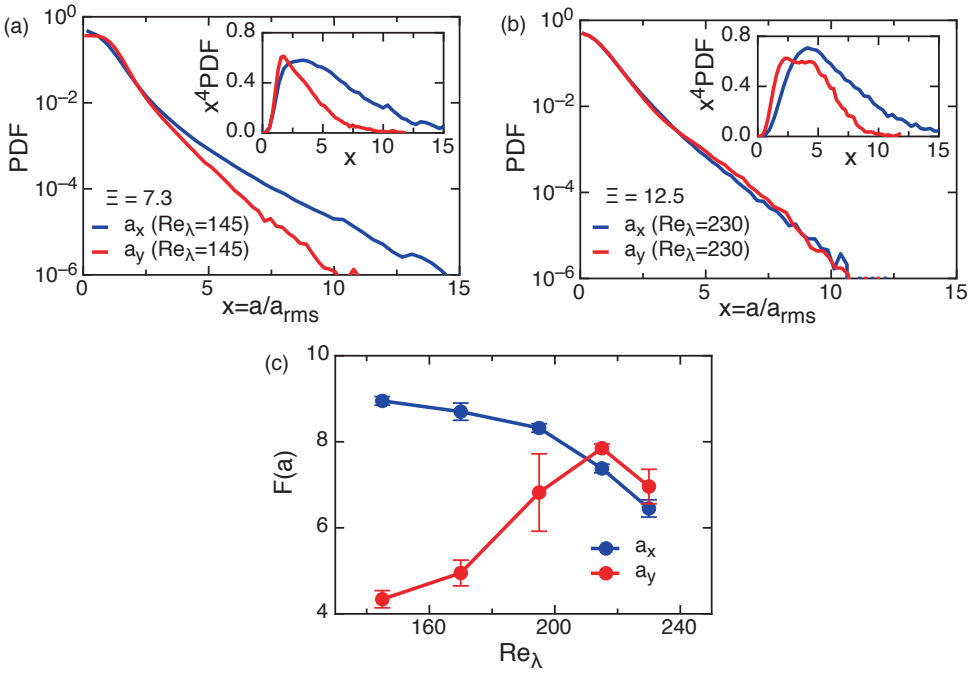

Figure 3.8: Normalized bubble acceleration PDFs of a_x and a_y components at $\mathrm{Re}_\lambda = (a)145$ and (b) 230, which are respectively the smallest and the largest Re_λ considered in our experiments. As expected, at the lower Re_λ the tails of the normalized PDF (in other words the flatness) of the vertical component are reduced compared to the horizontal one, while at the higher Re_λ the anisotropy is negligible. The insets in (a) and (b) show the fourth-order convergence test. (c) The acceleration flatness for the present bubbles (with errorbars) versus Re_λ.

The finite-sized bubble acceleration PDFs and the flatness values at two selected cases of Re_λ are shown in Fig. 3.8. The quality of statistics in the present experimental data is seen in the insets of Figs. 3.8(a) and (b), which demonstrate that the fourth-order moments are well converged. Hence, we can calculate the flatness directly from the distribution without resorting to a fitting procedure (e.g. as in Volk *et al.* [17]). In Fig. 3.8(c), we observe that the flatness values of a_y at $\mathrm{Re}_\lambda \leq 195$ are less than those of a_x. At higher Re_λ (≥ 215), the flatness values of a_x and a_y become comparable, and the corresponding PDFs show a nice collapse in Fig. 3.8(b). The decreased intermittency in the vertical component a_y for the low Re_λ (seen in Fig. 3.8(a)) is due to gravity. Apparently, there are two regimes: at lower Re_λ, gravity has an effect on the acceleration statistics in the vertical direction, which is no longer the case at higher Re_λ.

3.4.2 Acceleration Statistics: Size effect

Once the statistical influence of buoyancy has been disentangled, we now study how the gravity-less acceleration variance changes at increasing Ξ, in other words we study the purely hydrodynamic size-effect on particles which are lighter than the surrounding fluid. It is convenient to look at the relative change of the bubble acceleration variance with respect to fluid tracers $\langle a_{i,f}^2 \rangle$. For $a_{i,f}$ we use here the acceleration of the microbubbles as found in Ref. [20], because given their small size, $\Xi < 2$, they behave almost like Lagrangian tracers. Furthermore, the Re_λ numbers studied in the present experiments are very close to the ones analyzed in Ref. [20] and the flow conditions are the same. Fig. 3.7b reports such a normalized acceleration variance $\langle a_i^2 \rangle / \langle a_{i,f}^2 \rangle$ versus the size ratio Ξ. We see that both acceleration components reach a level of 5 ± 2 times the variance measured in the same flow for fluid tracers. They are also in agreement with the previous single experimental datapoint of Ref. [19]. To have an interpretation of this measurement we compare it with the results from numerical simulations at similar Re_λ. Fig. 3.7b reports results from two different types of Lagrangian particle simulations, first the so called point-particle (PP) simulation that only takes into account the hydrodynamic effects of added mass and Stokes-drag, and a second simulation which adds on Faxén corrections (FC) to the mentioned terms [14, 30]. The PP model predicts for $\Xi \to \infty$ an asymptotic limit of normalized acceleration variance which is 9 times that for tracers (as a result of the dominance of the added-mass term). From Fig 3.7b, we deduce that for $\Xi \approx 10$ in the PP model, it is about 15 times the value for tracers, reflecting that we are not yet in the asymptotic limit. For larger Ξ the results from the PP model indeed seem to approach the asymptotic value of normalized acceleration variance of 9. Faxén corrections to the added mass term reduce the value at $\Xi = 10$ which is about

7. Fig 3.7b clearly shows that numerical simulations of Faxén corrected finite-sized bubbles show a good agreement with the experimental measurements (contrary to the PP model which overestimates the result). The present results are the first systematic measurements to confirm that the acceleration variance increases with finite-size for bubbles, matching the FC numerical simulations [14]. Note again that the trend is very different for the case of neutrally buoyant particles and heavy particles, for which the normalized acceleration variance is always ≤ 1 [14, 17] It must also be noted that the acceleration statistics have been found not to show appreciable changes for $\Xi < 5$ in experiments [11, 15, 20] and for $\Xi < 2$ in numerics [14]. Hence, the numerical results are only shown in the regime $\Xi > 2$, where the Faxén corrections start playing a role.

Making statements on the fourth order statistical moments of acceleration based on experimental measurements is a delicate endeavor, see e.g. the detailed analysis by Volk *et al.* [19]. To study the finite-size effects on the bubble acceleration, in the following we will focus only on the PDF shape of the normalized $x-$acceleration, $a_x/\langle a_x \rangle_{\mathrm{rms}}$, which is not directly affected by gravity. In Fig. 3.9(a) first we plot such a curve for microbubbles [20] and see that its shape falls on the one for fluid tracers, and on $\Xi < 2$ bubbles, from DNS at similar Re_λ. This is an evidence of both the above mentioned passive nature of microbubbles and of the similarity between turbulence realized in the Twente Channel flow and the one produced in homogeneous and isotropic DNS. In the same panel we see that, in sharp contrast, the finite-sized bubbles show a strongly reduced intermittency. It is the first time that such a substantial change in intermittency at growing size ratios is experimentally observed: neither for solid neutrally buoyant particles [15, 17], nor for heavier bubbles [13] was it detected before.

In order to clarify further the magnitude of such an effect, in Fig. 3.9(b) we compare the acceleration PDF from the DNS simulations with Faxén corrections and the present experiments. There is an initial increase of flatness in the DNS simulations for $\Xi \lesssim 8$, which probably reflects the limitations of the Faxén corrections. For $\Xi \gtrsim 7-8$ both the numerics and the experiments show a significant reduction of the tails of the PDF. However, the DNS appears to underestimate its functional behavior by approximately a factor 2-3 in the size parameter Ξ. The reason for this discrepancy is presently unclear. One reason could be that the simulations neglect the two way coupling and are just approximated in the implementation of Faxén terms. Another possible reason for the discrepancy which deserves further study is the deformability of real bubbles. The deformation process absorbs/releases energy from/to the turbulent environment, a process which may have an effect on acceleration statistics. These issues motivate further investigations to better understand light particles

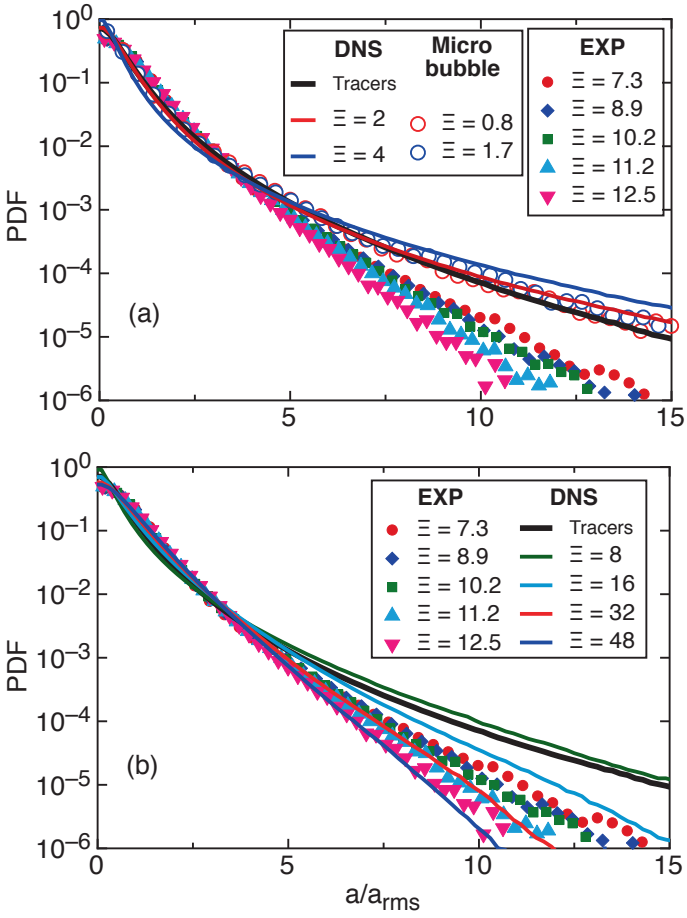

Figure 3.9: The normalized acceleration PDFs of the horizontal component $|a_x|$, from the present bubble experiments (EXP), microbubble measurements [20], and numerical simulations (DNS) with the Faxén model at $\mathrm{Re}_\lambda = 180$ [14]. (a) Comparison with results for point-like particles; DNS Tracers, microbubbles, and Faxén DNS of bubbles for $\Xi \leq 4$. (b) Comparison with Faxén DNS of larger bubbles, $\Xi \geq 8$.

in turbulence.

3.5 Conclusion

We performed measurements of Lagrangian acceleration in the previously unexplored regime of large (compared to η) and very light (with respect to ρ_f) particles in turbulence. Bubbles of size ~ 3 *mm* diameter (D) were tracked in turbulent flow conditions in a water tunnel. The explored range of Reynolds number (Re_λ) and size ratios, $\Xi = D/\eta$ were 145–230, and 7.3–12.5, respectively.

Gravity produces anisotropy in the acceleration statistics of the vertical component – it adds a g^2 offset to the variance, and decreases the intermittency of PDF, at lower Re_λ. It was found that the interaction between gravity and inertia is complex, and this deserves further study.

The acceleration variances clearly indicate the finite-size effect, and the results are in good agreement with DNS simulations with the Faxén corrections. The intermittency of experimental PDF decreases with increasing Ξ. However, the PDF obtained from the Faxén corrected numerics shows a difference of factor $\sim$ 2-3 in Ξ compared to the experiments. The reason for this discrepancy between numerics and experiments deserves further study. To improve the current understanding, in the future we plan to study rigid hollow spheres in the turbulent water flow, and to vary their diameters, D, at fixed Re_λ numbers.

References

[1] F. Toschi and E. Bodenschatz, *Lagrangian properties of particles in turbulence*, Annu. Rev. Fluid Mech. **41**, 375 (2009).

[2] A. La Porta, G. Voth, A. M. Crawford, J. Alexander, and E. Bodenschatz, *Fluid particle accelerations in fully developed turbulence*, Nature. **409**, 1017 (2001).

[3] D. Lohse, *Particles go with the flow*, Physics **1**, 18 (2008).

[4] A. Prosperetti and H. Oguz, *Physalis: A New o(N) Method for the Numerical Simulation of Disperse Systems: Potential Flow of Spheres*, J. Comput. Phys. **167**, 196 (2001).

[5] G. Tryggvason, B. Bunner, A. Esmaeeli, D. Juric, N. Al-Rawahi, W. Tauber, J. Han, S. Nas, and Y. Jan, *A Front-Tracking Method for the Computations of Multiphase Flow*, J. Comput. Phys. **169**, 708 (2001).

[6] A. Arneodo and *et al.*, *Universal intermittent properties of particle trajectories in highly turbulent flows*, Phys. Rev. Lett. **100**, 254504 (2008).

[7] R. Volk, E. Calzavarini, G. Verhille, D. Lohse, N. Mordant, J.-F. Pinton, and F. Toschi, *Acceleration of heavy and light particles in turbulence: Comparison between experiments and direct numerical simulations*, Physica D **237**, 2084 (2008).

[8] L. Biferale, E. Bodenschatz, M. Cencini, A. S. Lanotte, N. T. Ouellette, F. Toschi, and H. Xu, *Lagrangian structure functions in turbulence: A quantitative comparison between experiment and direct numerical simulation*, Phys. Fluids **20**, 065103 (2008).

[9] M. Maxey and J. Riley, *Equation of motion for a small rigid sphere in a nonuniform flow*, Phys. Fluids **26**, 883 (1983).

[10] R. Gatignol, *The Faxèn formulae for a rigid particle in an unsteady non-uniform stokes flow*, J. Mec. Theor. Appl. **1**, 143 (1983).

[11] G. Voth, A. La Porta, A. M. Crawford, J. Alexander, and E. Bodenschatz, *Measurement of particle accelerations in fully developed turbulence*, J. Fluid Mech. **469**, 121 (2002).

[12] N. M. Qureshi, M. Bourgoin, C. Baudet, A. Cartellier, and Y. Gagne, *Turbulent Transport of Material Particles: An Experimental Study of Finite Size Effects*, Phys. Rev. Lett. **99**, 184502 (2007).

[13] N. M. Qureshi, U. Arrieta, C. Baudet, A. Cartellier, Y. Gagne, and M. Bourgoin, *Acceleration statistics of inertial particles in turbulent flow*, Eur. Phys. J. B **66**, 531 (2008).

[14] E. Calzavarini, R. Volk, M. Bourgoin, E. Leveque, J.-F. Pinton, and F. Toschi, *Acceleration statistics of finite-sized particles in turbulent flow: the role of Faxèn forces*, J. Fluid Mech. **630**, 179 (2009).

[15] R. D. Brown, Z. Warhaft, and G. A. Voth, *Acceleration Statistics of Neutrally Buoyant Spherical Particles in Intense Turbulence*, Phys. Rev. Lett. **103**, 194501 (2009).

[16] M. Gibert, H. Xu, and E. Bodenschatz, *Inertial effects on two-particle relative dispersion in turbulent flows*, Europhys. Lett. **90**, 64005 (2010).

[17] R. Volk, E. Calzavarini, E. Leveque, and J.-F. Pinton, *Dynamics of inertial particles in a turbulent von Kármán flow*, J. Fluid Mech. **668**, 223 (2011).

[18] I. Mazzitelli and D. Lohse, *Lagrangian statistics for fluid particles and bubbles in turbulence*, New J. Phys. **6**, 203 (2004).

[19] R. Volk, N. Mordant, G. Verhille, and J.-F. Pinton, *Laser Doppler measurement of inertial particle and bubble accelerations in turbulence*, Europhys. Lett. **81**, 34002 (2008).

[20] J. Martínez Mercado, V. N. Prakash, Y. Tagawa, C. Sun, and D. Lohse, *Lagrangian statistics of light particles in turbulence*, Phys. Fluids **24**, 055106 (2012).

[21] R. Poorte and A. Biesheuvel, *Experiments on the motion of gas bubbles in turbulence generated by an active grid*, J. Fluid Mech. **461**, 127 (2002).

[22] Y. Tagawa, J. Martínez Mercado, V. N. Prakash, E. Calzavarini, C. Sun, and D. Lohse, *Three-dimensional Lagrangian Voronoi Analysis for clustering of particles and bubbles in turbulence*, J. Fluid Mech. **693**, 201 (2012).

[23] J. Martínez Mercado, D. Chehata Gómez, D. van Gils, C. Sun, and D. Lohse, *On bubble clustering and energy spectra in pseudo-turbulence*, J. Fluid Mech. **650**, 287 (2010).

[24] J. Rensen, S. Luther, and D. Lohse, *The effects of bubbles on developed turbulence*, J. Fluid Mech. **538**, 153 (2005).

[25] S. Takagi and Y. Matsumoto, *Surfactant Effects on Bubble Motion and Bubbly Flows*, Annu. Rev. Fluid Mech. **43**, 615 (2011).

[26] T. Peng, *Detect circles with various radii in grayscale image via Hough Transform* (MATLAB Central File Exchange, 9168, www.mathworks.com, 2005).

[27] R. C. Gonzalez, R. E. Woods, and S. L. Eddins, *Digital image processing using MATLAB* (Pearson Education, Inc., NJ, USA, 2004).

[28] D. H. Ballard, *Generalizing the Hough Transform to Detect Arbitrary Shapes*, Pattern Recognition **13**, 111 (1981).

[29] S. Takagi, T. Ogasawara, M. Fukuta, and Y. Matsumoto, *Surfactant effect on the bubble motions and bubbly flow structures in a vertical channel*, Fluid Dyn. Res. **41**, 065003 (2009).

[30] E. Calzavarini, R. Volk, E. Leveque, J.-F. Pinton, and F. Toschi, *Impact of trailing wake drag on the statistical properties and dynamics of finite-sized particle in turbulence*, Physica D **241**, 237 (2012).

4

Energy spectra in bubbly turbulence *

We conduct experiments in a turbulent bubbly flow to study the unknown nature of the transition between the classical -5/3 energy spectrum scaling for a single-phase turbulent flow and the -3 scaling for a swarm of bubbles rising in a quiescent liquid and of bubble-dominated turbulence. The bubblance parameter [1, 2], which measures the ratio of the bubble-induced kinetic energy to the kinetic energy induced by the turbulent liquid fluctuations before bubble injection, is used to characterise the bubbly flow. We vary the bubblance parameter from $b = \infty$ (pseudo-turbulence) to $b = 0$ (single-phase flow) over 2-3 orders of magnitude: $\approx O(0.01, 0.1, 5)$ to study its effect on the turbulent energy spectrum and liquid velocity fluctuations. The experiments are conducted in a multi-phase turbulent water tunnel with air bubbles of diameters 2-4 mm and 3-5 mm. An active-grid is used to generate nearly homogeneous and isotropic turbulence in the liquid flow. The liquid speeds and gas void fractions (α) are varied to achieve the above mentioned b parameter regimes. The experiments employ a phase-sensitive Constant Temperature Anemometry (CTA) technique, which provides in-situ *flow information to help discard bubble collisions. The probability distribution functions (PDFs) of the liquid velocity fluctuations show deviations from the Gaussian profile for $b > 0$, i.e. when bubbles are present in the system. The PDFs are asymmetric with higher probability in the positive tails. The*

*Submitted to J. Fluid Mech. as: Vivek N. Prakash, J. M. Mercado, F. E. M. Ramos, Y. Tagawa, D. Lohse, and C. Sun, Energy spectra in bubbly turbulence, (2013). arXiv: 1307.6252

net liquid fluctuations in the system slightly increase with the b parameter (when $b < 1$) and then saturate for $b > 1$. The energy spectra are found to follow the -3 subrange scaling not only in the well-established case of pseudo-turbulence, but in all cases where bubbles are present in the system ($b > 0$), in the present parameter regime. It is remarkable that this -3 scaling is followed even for small b parameter values ($b \sim O(0.01)$). This implies that the bubbles are extremely efficient in leaving their spectral signature in the flow, presumably due to the long lifetime of the bubbles' wake. The -3 spectrum scaling thus seems to be a generic feature of turbulent bubbly flows.

4.1 Introduction

Turbulent bubbly flow has important industrial applications such as in chemical industries and steel plants [3]. A fundamental understanding of the influence of bubbles on turbulence is crucial for better designs and optimal utilization of resources [4, 5]. The fundamental question we study in this chapter is: How do bubbles modify the turbulence? - i.e. what is their effect on the turbulent energy spectrum and liquid velocity fluctuations. The source of energy input in turbulent bubbly flows can have a contribution from both bubbles and some other external forcing (which affect the liquid fluctuations). Depending on this source of energy input, we can have various regimes in turbulent bubbly flows. The bubblance parameter "b" was introduced [1, 2] to distinguish between the regimes of pseudo-turbulence (i.e. turbulence driven solely by bubbles rising in a quiescent fluid) and turbulence induced by liquid fluctuations alone. The bubblance parameter is defined as a ratio of the bubble-induced kinetic energy to the kinetic energy induced by the turbulent liquid alone without bubbles:

$$b = \frac{1}{2}\frac{\alpha U_r^2}{u_0'^2}, \tag{4.1}$$

where, α is the bubble concentration (void fraction), U_r is the bubble rise velocity in still water, and u_0' is the typical turbulent liquid fluctuation in the absence of bubbles. The extreme cases are b = 0 for single-phase turbulent flow (i.e. bubbles being absent in the flow) and b = ∞ for pseudo-turbulence.

Pioneering measurements by [1] used hot-wire and Laser Doppler Anemometry (LDA) in a turbulent bubbly flow to show that the classical *-5/3* Kolmogorov energy spectrum exponent is progressively substituted by a *-8/3* exponent with increasing gas fraction α. They proposed that the steeper spectrum originates from the immediate dissipation of bubble wakes. They also put forward arguments based on dimensional analysis that the energy spectrum exponent is *-3* for pseudo-turbulence.

From the definition of the bubblance parameter, one would expect different spectral scaling behaviour depending on the energy input that is more dominant. For $b << 1$ the active-grid-induced turbulent fluctuations would be more dominant and hence the spectrum exponent would be close to *-5/3* (Kolmogorov). When $b >> 1$, the bubble-induced fluctuations would be important and the exponent would be closer to *-3* (see [2] for a review). Recent experiments [e.g. 6] have conclusively found that the energy spectrum exponent is close to *-3* for the pseudo-turbulent case (b = ∞). Other experiments in the wake of a swarm of rising bubbles (b = ∞) also found a spectral exponent ∼ *-3* [7]. Although a few early studies [e.g. 8, 9] have reported a spectrum scaling of *-5/3* for b = ∞, recent work have clearly established that the pseudo-turbulence spectrum scaling is close to *-3* [6, 10, 11]. In fact, the *-3* spectrum scaling is found to be robust even if the bubble size is changed, or if higher viscosity liquids are used instead of water. The recent study by [10] suggests that the specific details of the hydrodynamic interactions among bubbles do not influence the way in which the pseudo-turbulent fluctuations are produced. The current understanding is that the bubble-induced turbulence mainly results from the bubble wakes. The importance of the bubble wakes on the *-3* spectrum scaling has also been established using numerical simulations by comparing the spectrum scalings between point-like bubble simulations [12] and fully-resolved simulations of freely rising deformable bubbles [13], with the former one giving *-5/3* due to the absence of wakes, and the latter fully-resolved simulations giving *-3* as the spectral scaling exponent.

A new approach proposed by Risso *et al.* [14] is to decompose the total liquid fluctuations into two contributions: spatial and temporal parts. Experiments with rising bubbles can only measure the sum of the spatial and the temporal fluctuations; and the two contributions cannot be easily distinguished. However, experiments with a fixed array of spheres distributed randomly in a uniform flow have been able to separately study the two contributions [14]. These experiments have suggested that the spatial contribution is dominant over the temporal part upto bubble Reynolds numbers ∼ 1000. Recent numerical simulations have found that the spectra of both the spatial and temporal contributions result in a *-3* scaling [11]. In the present work, we add external turbulence using an active-grid to the system of rising bubbles by varying the b parameter.

Previous work has mainly been concerned with the extreme values of the b parameter, i.e. either pseudo-turbulence ($b = \infty$) or single-phase turbulence (b = 0). Our focus in this chapter is to study what happens *in between these extremes* $b = \infty$ and $b = 0$ as the energy spectrum scaling and the liquid velocity fluctuation statistics are not well known for large ranges of intermediate b. In this chapter, we thus want to systematically analyse the flow as a function of the b parameter between the cases

of single-phase turbulence ($b = 0$), turbulence with some bubbles ($0 < b < 5$). The b parameter is varied over 2-3 orders of magnitude, namely from 0.01 to 5, and the pseudo turbulent case $b = \infty$ is also included.

In the next section, we describe the experimental setup, tools and methods used. This is followed by the results section where we describe our findings for the liquid velocity fluctuations and energy spectra. We provide an interpretation of our results in the discussion section and summarise our work.

4.2 Experiments

4.2.1 Experimental setup

The experiments are carried out in the Twente Water Tunnel (TWT) facility, which is an $8m$-high vertical water tunnel (see Figure 4.1). The measurement section of the TWT (dimensions: $2m \times 0.45m \times 0.45m$) is made of transparent glass to provide optical access for flow visualization and measurements. We place the phase-sensitive CTA (hot-film) probe in the centre of this measurement section, more details on this technique are discussed in the next section. An active-grid is used to generate nearly homogeneous and isotropic turbulent flow in the liquid phase and it is placed below the test section [15–17]. Air bubbles are generated by blowing air through islands of capillary needles that are located below the measurement section. A U-tube setup mounted in the measurement section is used to measure the gas void fraction α (see Ref. [2, 6] for more details). The bubbles pass through the active-grid, rise through the measurement section and eventually escape through an open vent at the top of the TWT. The liquid mean flow is driven by a pump which recirculates the water throughout the TWT. The bubbles rise along with the upward mean flow in the measurement section; in other words, the system is a co-flowing turbulent upward bubbly flow.

In the present experiments, the b parameter:

$$b = \frac{1}{2}\frac{\alpha U_r^2}{u_0'^2} \tag{4.2}$$

is varied by changing: (i) the volume flow rate of air (i.e. equivalent to changing the gas void fraction α) through the capillary islands, (ii) the magnitude of the mean flow speed of water in the upward direction (to effectively change the turbulence intensity u_0'). In equation 4.1, U_r is the typical bubble rise velocity (in still water), and for both set 1 and set 2 we assume $U_r \approx 23$ cm s^{-1} [18].

We vary the bubble diameter by changing the inner diameter of the capillary needles in the bubble generating islands. Air bubbles of diameter 3-5 mm and 2-4

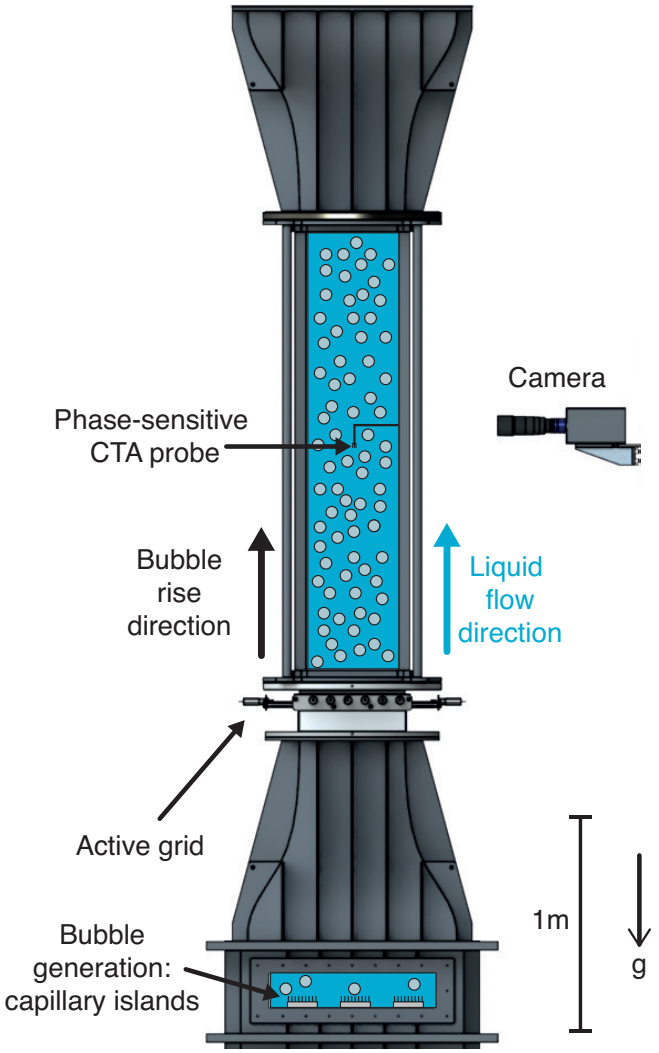

Figure 4.1: The Twente Water Tunnel (TWT) facility: A vertical multiphase water tunnel where homogeneous and isotropic turbulence is generated by an active-grid. Air is blown through capillary islands located below the measurement section to generate bubbles. The bubble rise direction and liquid flow are both in the upward direction, and the phase-sensitive CTA probe measures the liquid velocity fluctuations.

set 1				set 2			
b	α %	u_0' cm s^{-1}	U_l cm s^{-1}	**b**	α %	u_0' cm s^{-1}	U_l cm s^{-1}
∞	2	0	0	∞	2	0	0
∞	1.17	0	0	∞	1.5	0	0
4.13	1	0.8	10	∞	1	0	0
2.06	0.5	0.8	10	∞	0.8	0	0
1.03	1	1.6	20	∞	0.5	0	0
0.78	0.75	1.6	20	4.13	1	0.8	10
0.52	0.5	1.6	20	2.06	0.5	0.8	10
0.17	0.67	3.2	40	1.03	1	1.6	20
0.08	0.3	3.2	40	0.78	0.75	1.6	20
0.03	0.17	4	50	0.52	0.5	1.6	20
0.01	0.083	4.8	60	0.37	0.8	2.4	30
0	0	2.4	30	0.23	0.5	2.4	30
				0.21	0.2	1.6	20
				0.15	0.6	3.2	40
				0.08	0.3	3.2	40
				0.03	0.2	4	50
				0	0	2.4	30

Table 4.1: Experimental parameters, set 1: 3-5 mm bubbles, set 2: 2-4 mm bubbles

mm are produced using capillary needles of inner diameter 500 μm and 120 μm, respectively. We classify our experiments into two sets based on the bubble diameter - experiments with bubbles of diameter 3-5 mm belong to set 1, and experiments with bubbles of diameter 2-4 mm are referred to as set 2 (see Table 4.1).

We obtain b parameter values from ∞ to 0 by varying the void fraction (2 to 0%) and the mean flow velocity (0 to 60 cm s^{-1}). Table 4.1 lists all the different parameters varied in the present experiments. The turbulent flow properties (e.g. u_0') are characterised by combined CTA - LDA (Laser Doppler Anemometry) measurements of only the liquid phase at different mean flow speeds (for details see [17]).

In order to visualise the flow, a Photron-PCI 1024 high-speed camera was focused on a vertical plane at the centre of the measurement section. We acquired two-dimensional images of each experiment using the camera (at $1000Hz$) and some of these snapshots are shown in Figure 4.2. The $b = \infty$ experiments are shown in Figure 4.2(a) and (b) where the gas void fractions are α = 2% and 1%, respectively.

The dense nature of the flow at such void fractions is evident: the flow is opaque and the phase-sensitive CTA probe is barely visible. As we proceed to look at the other cases in Figure 4.2(c)-(f), α decreases, and the liquid mean flow speeds (U_l) increase, corresponding to a decrease in the b parameter from ∞ to 0.03. In our experiments, the bubbles must pass through the active-grid, which consists of randomly oscillating steel flaps ($\approx$ few rotations per second) to generate the required turbulence. At any given instant of time, the active grid is 50% transparent (open) to the flow. Hence, the bubbles face a slight obstruction and sometimes interact with the steel flaps. The obstruction has a local effect which is negligible when considering the overall flow, and the CTA probe is located sufficiently far away ($\approx 1m$) from the active-grid. The bubble-flap interaction, however, causes fragmentation of the bubbles and results in a decrease of the diameter of the bubbles. This bubble diameter decrease becomes apparent at higher liquid mean flow speeds (U_l), as seen in Figure 4.2(c)-(f).

We obtain a quantitative measurement of the bubble diameter using the images acquired (Figure 4.2) from the individual experiments. The bubbles highly deform over time, and given the dense nature (high α) of the flows, there is currently no reliable automated image processing algorithm available to accurately determine the bubble diameter. Hence, we had to resort to a manual procedure - where individual bubble boundaries are marked using mouse-clicks in the open-source ImageJ software. An ellipse is fitted to the deformed bubble boundaries, and the equivalent bubble diameter is calculated as: $d_b = \sqrt[3]{d_l^2 d_s}$, where d_l and d_s are the long and short axes of the ellipsoidal bubble. In each experiment, we measure the diameters of $\approx 50-100$ bubble samples, and then take the mean value of the distribution to be the equivalent diameter of the bubble. In Figure 4.3 we observe that the bubble diameter decreases with a decrease in the b parameter (increasing liquid mean flow speeds). The decrease in the bubble diameters at higher liquid mean flow speeds is mainly due to the fragmentation of the bubbles (as described above) (also see [16]). Here, the error bars represent the standard deviation of the measured distribution of bubble diameters.

At high mean flow speeds, air is entrained from an open vent at the top of the TWT because of oscillations of the free-surface exposed to the atmosphere. The entrained air unavoidably results in micro-bubbles which are fed back into the measurement section and contaminate the flow. These entrained micro-bubbles pose a problem at mean flow speeds higher than 30 cm s^{-1}, and are visible (as very small bubbles) in Figure 4.2(e) and (f). It is necessary to account for these micro-bubbles in the data analysis, and this issue will be discussed further below.

The present experiments in the pseudo-turbulence regime ($b = \infty$) for set 1, are essentially the same as the measurements carried out in [6], and serve as a reference

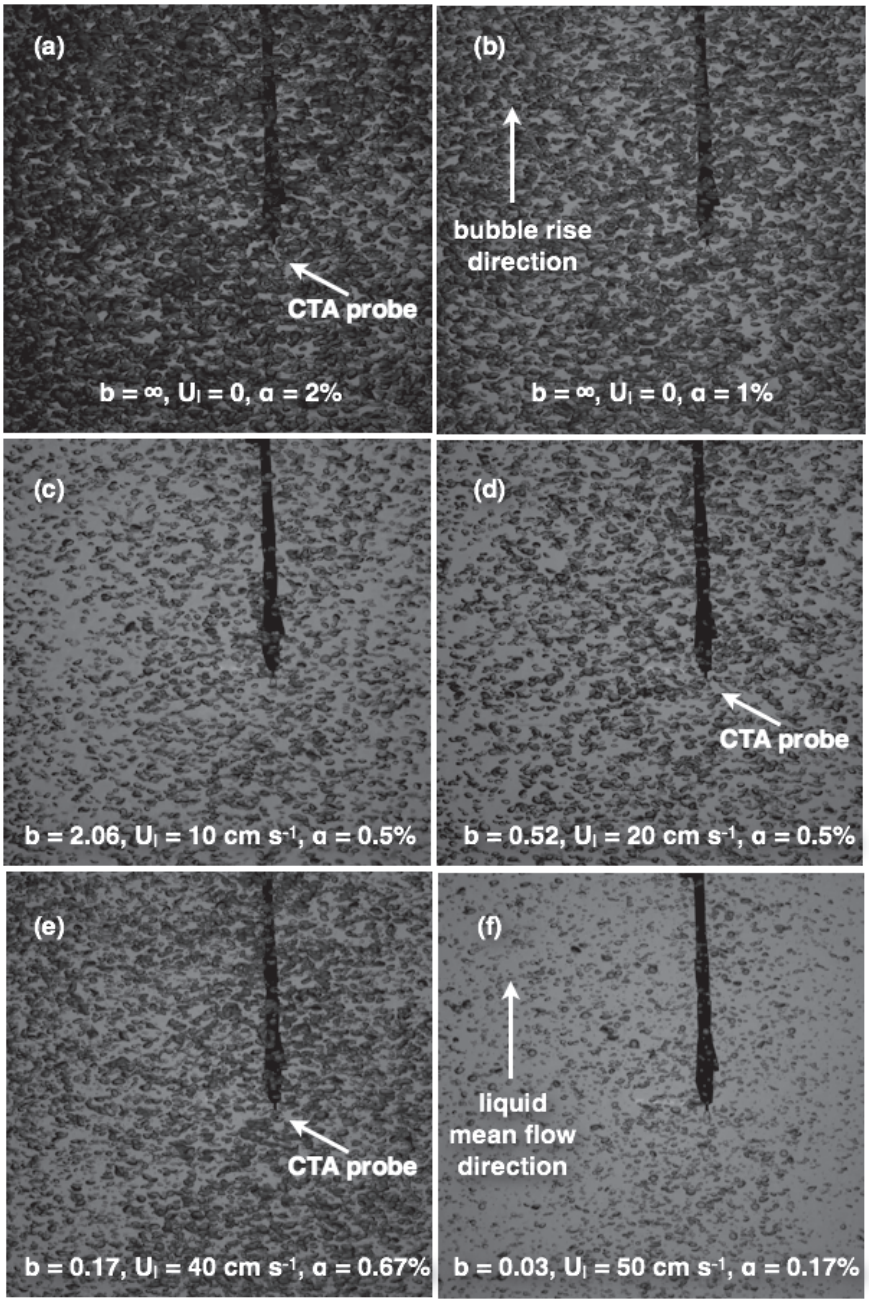

Figure 4.2: Snapshots from the experiments (set 1, see Table 4.1) at different conditions.

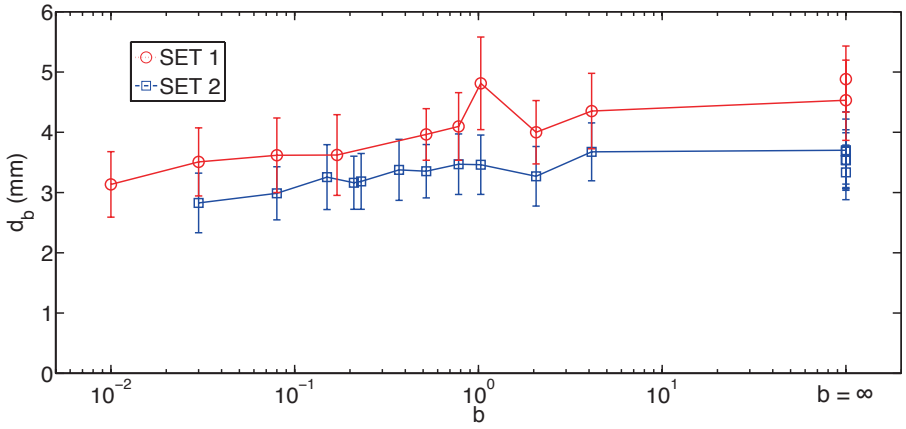

Figure 4.3: Bubble diameter versus the b parameter. The error bars are estimated based on the standard deviations.

case for the data analysis and results. For this case of freely rising bubbles in a quiescent liquid, the bubble-based Reynolds number $Re = d_b U_r/\nu \approx 1000$ [6], where ν is the kinematic viscosity of water (1×10^{-6} m^2 s^{-1}).

4.2.2 Phase-sensitive constant temperature anemometry

Hot-film anemometry is a preferred technique in single-phase turbulent flows, but its application in bubbly flows is not straightforward. Since it is an intrusive technique, bubble-probe interactions result in disturbances in the hot-film time series voltage signal. Various methods have been developed in the past to remove these 'bubbly spikes' [2, 19, 20], so as to exclusively analyse only the liquid fluctuation segments measured by the hot-film probe. For example, a threshold method was used by Zenit [19] and Martinez Mercado *et al.* [20] and a pattern-recognition method was used by Rensen *et al.* [2]. These methods essentially come up with an indicator function that labels the gas and liquid phase separately. However, a much better approach to eliminate the bubbly spikes from the CTA signal is to measure the indicator function *in-situ* during the experiments. This can be done by attaching optic fibres with a diameter of $\sim$100 μm close to the hot-film probe (at a distance $\sim$1 mm) to detect the gas phase. Light is continuously passed through the optic fibre, and when a bubble collides with the probe, the change in refractive index of the gas phase results in a signal change. This technique, called the phase-sensitive Constant Temperature Anemometry (CTA) was developed by van den Berg *et al.* [21] and is used in Martinez Mercado *et al.* [6] and Mendez-Diaz *et al.* [10]. This method can be used to

directly detect and remove the bubbly spikes in the hot-film signal.

In this work, we follow almost the same experimental procedure and analysis as in Martinez Mercado *et al.* [6], but the important difference here is that we vary the b parameter over a wide range to cover the regimes between pseudo-turbulence ($b = \infty$) and single-phase turbulent flow ($b = 0$). The phase indicator function obtained using information from the optic fibre signal labels the liquid fluctuations and bubble collisions separately. This is used to remove the bubbly spikes and separate the segments containing only liquid fluctuations from the time series signal for further analysis. The power spectrum was calculated for each segment of liquid fluctuation and averaged to obtain the spectrum for a particular case of b. The phase-sensitive CTA probe is calibrated by simultaneous measurement of absolute velocities of the single-phase using a DANTEC Laser Doppler Anemometry (LDA) setup (as in Ref. [16, 17]). The standard King's law fit is used for the voltage-velocity data. The acquisition rate was 10 kHz and the measurements were carried out for a duration of 1 hour in each case.

The phase-sensitive CTA technique works very well for pseudo-turbulent bubbly flows where the bubble diameters are in the range $\sim$ 2-5 mm. However, when micro-bubbles collide with the CTA probe, the optic fibres will not be able to register the collision. The reasons for this are two-fold: (i) the micro-bubbles are small in size ($\lesssim 300\ \mu$m diameter), and (ii) the separation distance between the CTA probe and the optical fibres is larger ($\sim$ 1 mm) than the micro-bubble size. As we mentioned before, micro-bubbles cause a contamination in the present experiments when the mean flow speeds exceed 30 cm s^{-1}. In these experiments, we inevitably use a threshold method to remove the micro-bubble collisions, in addition to the phase information obtained from the optic fibres. Further, to keep the data analysis consistent, the combination of the optical fibres and the threshold method is also used in all the experiments except pseudo-turbulence, where only the optical fibres are used.

4.3 Results and discussion

4.3.1 Liquid velocity statistics

The liquid velocity time-series signal was measured using the phase-sensitive CTA technique at different b parameter values. We now consider the statistics of these liquid velocity fluctuations using the separated segments of the signal which are free from the bubble collisions. In Figure 4.4, we present the normalized liquid velocity probability distribution functions (PDFs) for the different values of b covered in the present work, including both set 1 and set 2 experiments (see Table 4.1). The liquid velocity PDF for single-phase turbulent liquid ($b = 0$) at a mean flow of 30

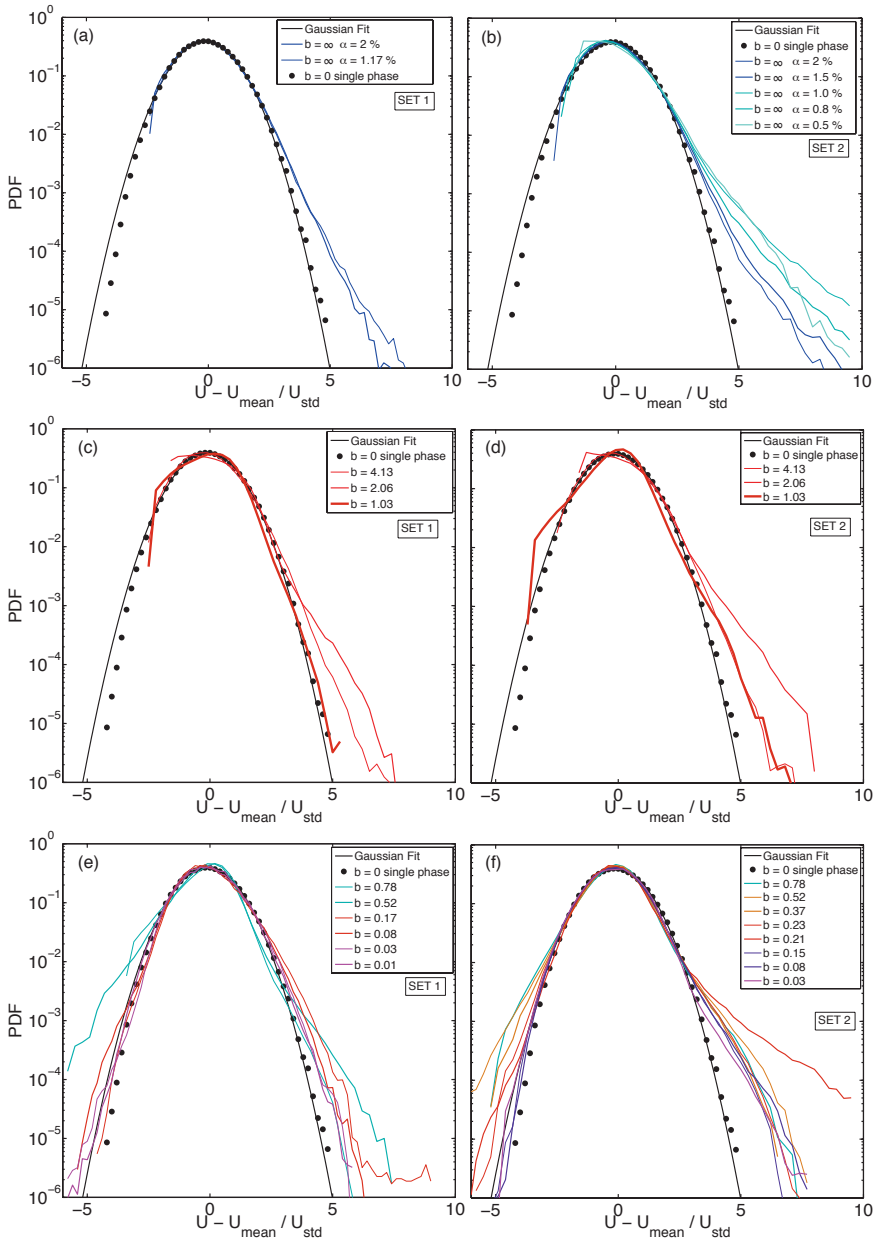

Figure 4.4: The liquid velocity PDFs for different b, left panel: set 1, right panel: set 2. (a, b) represent $b = 0, \infty$, (c, d) $b = 0$ and > 1, (e,f) $b = 0$ and < 1. All the bubbly flow cases show deviations from the Gaussian profile with enhanced probability of upward fluctuations.

cm s^{-1} (Taylor Reynolds numbers $Re_\lambda = 170$) (black dots) closely follows Gaussian statistics. This single-phase result serves as the reference case. The liquid velocity PDFs for the cases with bubbles (b > 0) are asymmetric and show a deviation from Gaussian behavior. The positive tails of the PDFs show higher probability compared to the Gaussian profile. This is probably because of flow entrainment in the wake of the rising bubbles, which leads to a larger probability of upward fluctuations [7, 22].

The velocity PDFs for the two pseudo-turbulence cases in the set 1 experiments ($b = \infty, \alpha = 2, 1.17$ %) show higher upward fluctuations and almost collapse (Figure 4.4(a)). In the pseudo-turbulent cases ($b = \infty$) of the set 2 experiments, the velocity PDFs also show a clear deviation from the Gaussian distribution, with more upward fluctuations (Figure 4.4(b)). Within these experiments ($b = \infty$), for different void fractions ($\alpha = 2\%, 1.5\%, 1\%, 0.8\%, 0.5\%$) there is no clear trend, but all the cases show an asymmetric profile compared to the purely liquid phase ($b = 0$). As the b parameter decreases to $b = 4.13$–1.03 in the set 1 experiments (Figure 4.4(c)), we see both increases and decreases in the positive tails compared to the pseudo-turbulent cases. In the set 2 experiments, at $b = 4.13$–1.03 (Figure 4.4(d)), the results are comparable to the pseudo-turbulence cases (Figure 4.4(b)). In Figure 4.4(e), for the set 1 experiments, the b parameter values are in the range $b = 0.78$–0.01. Although we do not observe a clear trend on the dependence of the PDF shape on the b parameter, it is clear that the positive tails of the PDFs show more upward fluctuations compared to the Gaussian profile, as far as bubbles are present in the system. The velocity PDFs corresponding to the set 2 experiments with b parameter values 0.78–0.03 (Figure 4.4(f)) in general show a reasonable collapse (except the $b = 0.21$ case). Similar to the set 1 results, the upward fluctuations of the liquid velocity PDFs in general decrease as the b parameter values decrease and start approaching the purely liquid phase ($b = 0$). All the bubbly flow cases ($b > 0$) show a deviation from the Gaussian profile, and are asymmetric with the positive tails showing a higher probability of upward fluctuations.

We further examine the statistics of the liquid velocity fluctuations for different values of the b parameter. In Figure 4.5, we plot the standard deviation values of the liquid fluctuations for each case of the b parameter. In Figure 4.5, as we move towards the left ($b \to 0$), the energy induced by the liquid mean flow starts to become dominant, and as we move towards the right ($b \to \infty$), the energy induced by the bubbles is dominant. The net liquid fluctuations in the system, measured by the standard deviation of the liquid fluctuations, slightly increase with increase in the b parameter up to $b \approx 1$ (as indicated in Figure 4.5), and then saturate. When $b < 1$, the externally-induced turbulent energy (resulting from the active-grid) weakly decreases the net fluctuations with decrease in the b parameter. When $b > 1$, the bubble-induced

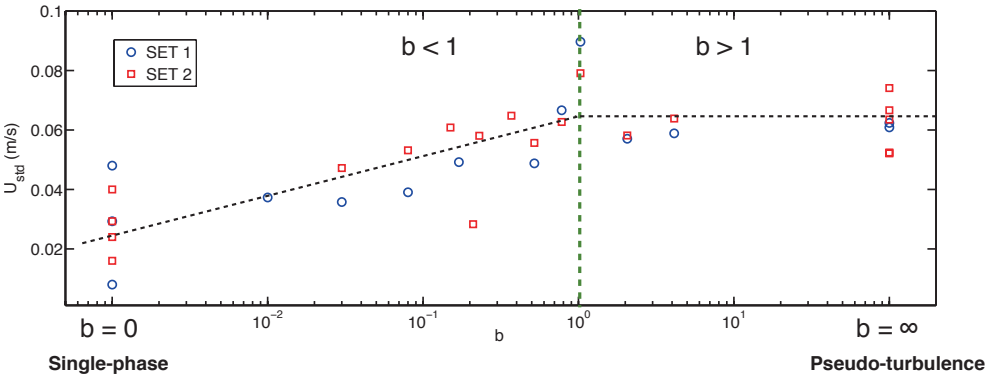

Figure 4.5: Liquid velocity fluctuation statistics at different b parameter values. For $b < 1$, the net liquid fluctuations weakly increase with the b parameter. For $b > 1$, there is no clear dependence on the b parameter.

kinetic energy dominates and there is no dependence of the fluctuations on the b parameter. This implies that adding the active-grid-induced external turbulence to a bubbly flow does not significantly change the total liquid fluctuations. There is a reasonable agreement between the trends shown by the two datasets (set 1 and set 2) in the present study. We discuss results on the velocity PDFs and energy spectra at three regimes based on the classification in Figure 4.5: the pseudo-turbulence regime ($b = \infty$), the mixed regime $b > 1$ ($b \sim O(1)$), and the mixed regime approaching single-phase $b < 1$ ($b \sim O(0.1, 0.01)$).

4.3.2 Energy Spectra

We will now focus on the turbulent energy spectrum of the liquid velocity fluctuations at the different regimes of b. The energy spectrum scaling is well-established for the standard cases of single-phase turbulence ($b = 0$): the classical Kolmogorov *-5/3* scaling (apart from intermittency corrections, Ref. [23]), and for pseudo-turbulence ($b = \infty$): a *-3* scaling [1, 6, 10, 11, 13]. Here, we want to investigate how the spectrum scaling changes from pseudo-turbulence (*-3*) to single-phase turbulence (*-5/3*). The energy spectrum (Power Spectral Density, PSD) was calculated for individual segments of the liquid fluctuations (free from bubbly spikes) using the Welch method (using hamming windows) at fixed frequencies, and then averaged over all the liquid segments in the measurement to obtain the final result (as in Ref. [6]). The segments selected for the spectrum calculation must have a certain minimum length to properly resolve all the frequencies; segments that are too short will lack information on

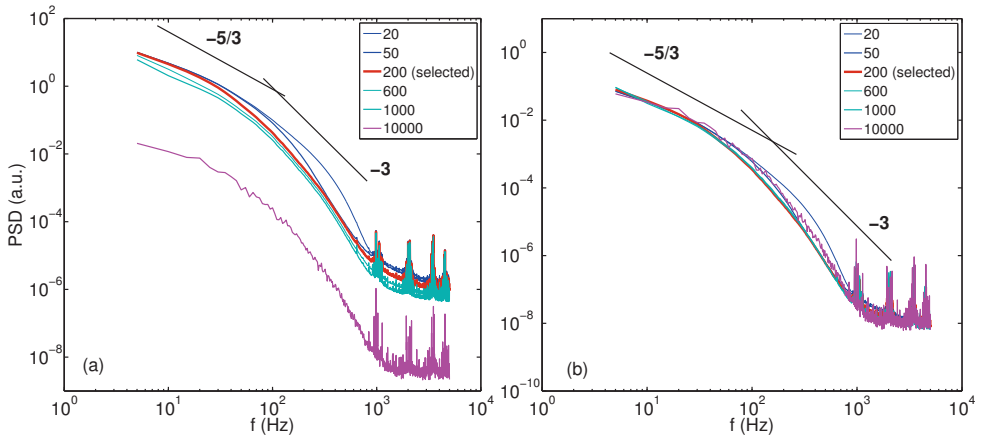

Figure 4.6: Minimum sample size criterion for the calculation of the energy spectrum, for the case $b = 0.23$ (set 2) (a) non-normalised spectra (b) normalised spectra. The different coloured lines are the spectra obtained with various sample sizes, as shown in the legend. The normalised spectrum (b) does not change when the sample size is sufficiently long. A sample size of 200 is found to be optimal in the present work with the sampling frequency of 10 kHz.

the large length-scales (low frequencies) and will simply add to the high frequency components of the spectrum (noise). We investigate the effect of varying this minimum sample size criterion on the spectrum for a selected case of $b = 0.23$ (set 2); the results are shown in Figure 4.6. We observe drastic changes in the spectra depending on the value of the minimum sample length. In Figure 4.6(a) we show the spectra directly obtained from the calculation. Both the amplitude and the scaling change; with a monotonic decrease in energy with increase in sample length. This is expected because when we increase the minimum sample length considered, we have fewer segments considered and the average energy decreases. In the extreme case of minimum sample length of 10000 data points ($\sim$1s), the spectrum looks noisy as it was averaged only over 80 segments. For the present data, we have selected an optimal minimum sample length of 200 data points ($\sim$0.02s), which nicely resolves all the frequencies (the spectrum is averaged over 14500 segments). In Figure 4.6(b), we show the same spectra after normalising the area under the curve to be equal to unity. We observe that the selected value of 200 is an optimal value; the extreme values (20, 10000) show deviations in the scaling. In the sections that follow, we present results for the normalised spectra in all the cases of b parameter as it allows us to focus solely on changes in the scaling. The energy in the non-normalised spectra depends

on the number of samples considered in the averaging, and this can differ in each experiment as it depends on the flow conditions; hence, we normalise the spectra.

The spectra for different values of b are shown in Figure 4.7. The shown spectra are the calculated PSD (in arbitrary units) per frequency versus the frequency (in Hz), and they are normalised so that the area under the curve equals unity. The solid lines are drawn to aid comparison of the present results with the two 'standard' power law scalings (*-3* and *-5/3*). We also show these spectra compensated with the *-5/3* and *-3* scaling in Figures 4.8(a),(b) and (c),(d) respectively. The single-phase turbulent spectrum is shown in all the cases and serves as a reference case. As expected, the single-phase spectrum ($b = 0$, black solid line) shows a good agreement with the Kolmogorov *-5/3* scaling in the inertial range (at lower frequencies, large length scales), and rapidly drops in energy as we move towards the dissipative range (higher frequencies, smaller length scales).

We first consider the bubbly spectra in the pseudo-turbulence regime ($b = \infty$) from the set 1 experiments (see Table 4.1) in Figure 4.7(a). These pseudo-turbulence cases, $b = \infty$, α = 2% and 1.17% nicely follow the *-3* scaling, with a clear deviation from the single-phase spectrum, confirming previous results (e.g. [6, 10, 11]). It is believed that the *-3* spectrum sub-range at intermediate length scales originates from the wakes of the rising bubbles. We mark the characteristic frequency of the freely rising bubbles (set 1): $f_{b1} \approx U_r/2\pi d_{b1} \approx 9 \simeq O(10)$ Hz, where, $U_r \simeq 23$ cm s^{-1} [18] is the bubble rise velocity in still water, and d_{b1} = 5-3 mm is the range of bubble diameters (see Figure 4.3). This frequency f_{b1} represents a transition (or cut-off) frequency where the bubbly spectra change slope from *-5/3* (Kolmogorov) to *-3* (pseudo-turbulence). The bubbly spectra follow the *-5/3* (Kolmogorov) scaling till the transition frequency f_{b1}, beyond which they follow the *-3* pseudo-turbulence scaling. In Figure 4.7(b), we compare these pseudo-turbulence results (set 1 experiments) to a different size distribution (set 2 experiments) of the bubbles (see Table 4.1). All of the $b = \infty$ cases in the set 2 experiments with $\alpha = 2, 1.5, 1, 0.8, 0.5\%$, nicely follow the *-3* spectrum scaling beyond the transition frequency f_{b2} (also see the *-3* compensated plot - Figure 4.8(d)). Here, the characteristic bubble frequency is $f_{b2} \approx U_r/2\pi d_{b2} \approx 12 \simeq O(10)$ Hz, where, $U_r \simeq 23$ cm s^{-1} [18] is the bubble rise velocity in still water, and d_{b2} = 4-2 mm is the bubble diameter for the set 2 experiments (see Figure 4.3). These results once again confirm the typical pseudo-turbulence *-3* energy spectrum scaling for freely rising bubbles. Hence, for length scales smaller than the bubble size ($f > f_b$), the turbulence induced by the bubble wakes results in a *-3* scaling and for larger length scales ($f < f_b$), the classical Kolmogorov *-5/3* scaling seems to hold.

We now depart from the pseudo-turbulent case and get into mixed regimes which are in between pseudo-turbulence and single-phase. For b parameter values in the

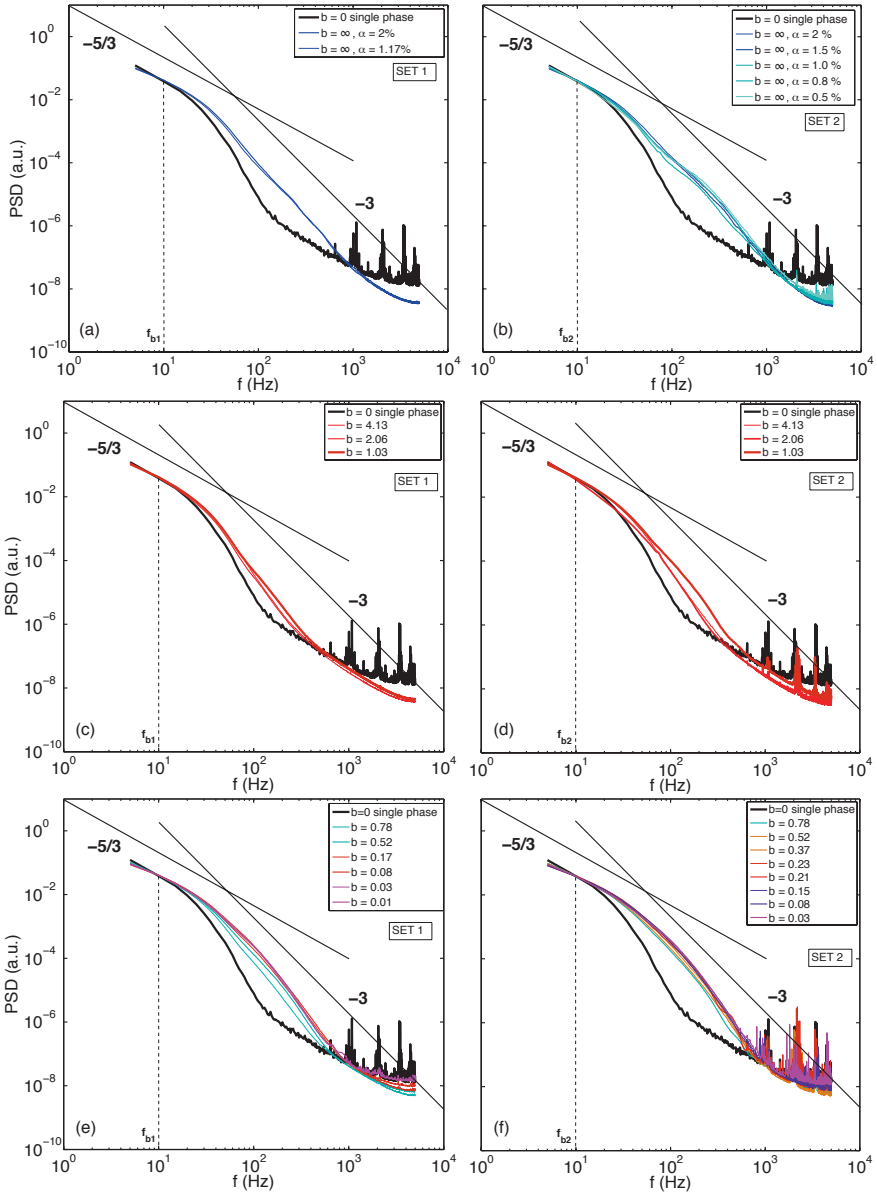

Figure 4.7: The normalised energy spectra at different b, left panel: set 1, right panel: set 2. (a, b) represent $b = 0, \infty$, (c, d) $b = 0$ and > 1, (e,f) $b = 0$ and < 1. All the bubbly flow cases show deviation from the *-5/3* Kolmogorov single-phase spectrum beyond the transition frequency (at 10 Hz as indicated with the dotted line), and reasonably follow the *-3* scaling.

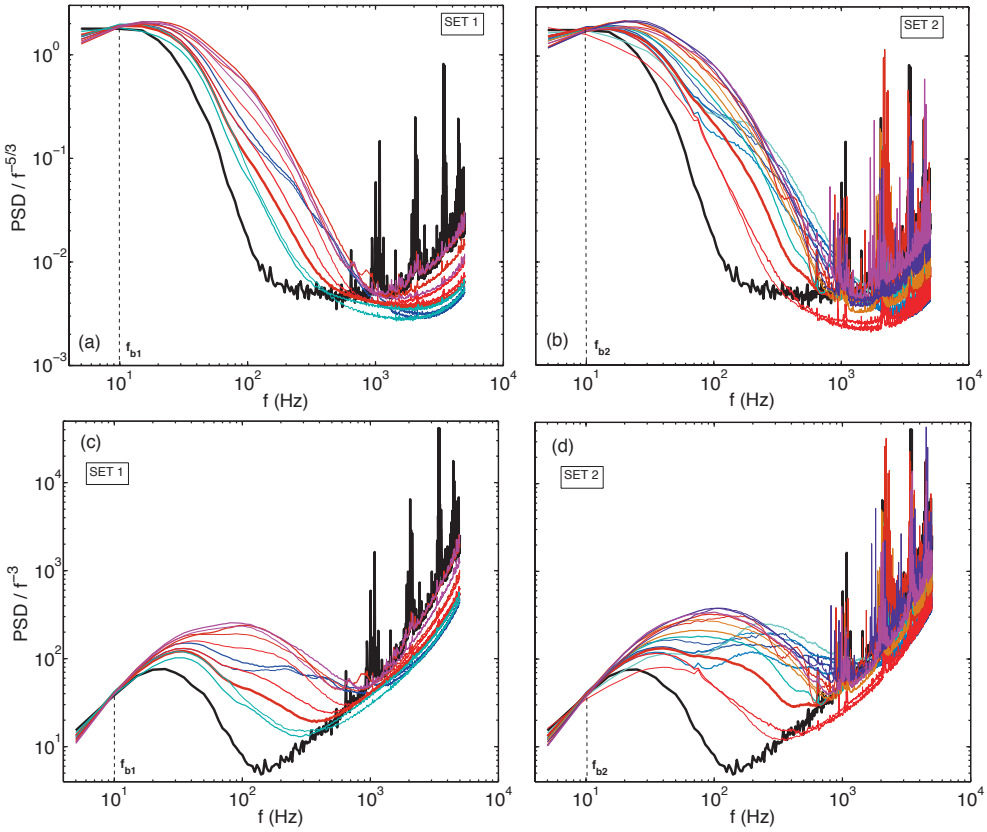

Figure 4.8: The compensated energy spectra at different b. left panel: set 1, right panel: set 2. (a,b) spectra compensated with *-5/3*, (c,d) spectra compensated with *-3*. The thick black lines indicate the single phase case. The colours for the bubbly flow cases correspond to the scheme in Fig 4.7. As observed in (c,d), all the bubbly flow cases roughly exhibit the *-3* scaling.

order of 1, i.e. for $b > 1$, the net fluctuations did not show a change when the b parameter changes from pseudo-turbulence ($b = \infty$) to $b \sim O(1)$ (Figure 4.5), then the question is whether there is a change in the spectra? The spectrum results for the set 1 experiments ($b = 4.13, 2.06, 1.03$) and set 2 experiments ($b = 4.13, 2.06, 1.03$) are shown in Figure 4.7(c) and (d) respectively. We observe that the spectra do not change significantly as compared to the pseudo-turbulent case. Although there is a very slight energy decrease at frequencies around 100 Hz compared the pseudo-turbulent cases, the *-3* scaling still holds.

At b parameter values less than 1 ($b < 1$), we have previously seen (in Figure 4.5) that the net liquid velocity fluctuations show a weak decrease with decreasing b parameter value. In this regime, the surrounding liquid turbulence starts to have a dominant contribution. Hence, it is interesting to study how the spectra eventually approach the single-phase scaling behaviour. We now look at the spectral results for b parameter values in the order of ∼O(0.1,0.01). Figure 4.7(e) shows the spectrum results for the set 1 experiments with b parameter values $b = 0.78 - 0.01$. Surprisingly, we observe that the *-3* scaling is still followed in all the cases beyond the transition frequency f_{b1}. We can also observe a very slight increase in energy at the intermediate scales (around frequencies $\sim$ 100 Hz) as the b parameter decreases from $b = 0.78$ to $b = 0.01$, but the *-3* scaling does not change much. In the set 2 experiments (Figure 4.7(f)), we cover more cases of the b parameter, $b = 0.78 - 0.03$, and find that the results are very similar to the set 1 experiments (Figure 4.7(e)). Once again, there is a gradual energy increase at the intermediate scales as b parameter decreases from $b = 0.78$ to $b = 0.03$, but the *-3* scaling is followed nicely. In the cases at low $b \sim O(0.01)$, the active-grid-induced turbulence dominates the flow, but remarkably the spectra still show a reasonable *-3* subrange scaling. This finding suggests that even a small 'contribution' of turbulent flow by bubble wakes is sufficient to modify the spectral properties, due to the long lifetime of the bubble wakes. The two experimental sets with different bubble diameters (set 1 and set 2) have revealed essentially similar results and trends.

4.4 Discussion and summary

We have systematically varied the bubblance parameter from $b = \infty$ to $b = 0.01$, and studied in detail the liquid velocity PDFs and energy spectra. The liquid velocity PDFs for the bubbly cases ($b > 0$) show asymmetry, and more upward fluctuations compared to a Gaussian profile. When $b < 1$, the net liquid fluctuations reveal a weak dependence with the b parameter; a slight decrease in the fluctuations with decrease in b. We then looked at the effect of varying the bubblance parameter on the energy

spectrum scaling. We have seen in Figure 4.7 that the energy spectra for all the cases (both set 1 and set 2) with bubblance parameter $b > 0$ follow the *-5/3* Kolmogorov spectrum scaling at the large length-scales (see Figure 4.8(a,b)). Beyond the transition frequency, all the bubbly spectra roughly exhibit the *-3* subrange scaling (see Figure 4.8(c,d)), which has been associated with the bubble wakes. In our experiments, we have added active-grid-induced turbulence to the configuration of rising bubbles to change the b parameter. The active-grid-induced turbulence has a weak influence on the velocity fluctuations, but why doesn't it have an influence on the turbulent energy spectra? We will look for clues to answer this question by probing deeper into the physics of bubbly flows.

Risso and co-workers proposed that multi-body wake-interaction mechanisms can be studied by decomposing the velocity fluctuations into spatial and temporal contributions [11, 14, 24]. Denoting the spatial averaging by brackets, and time averaging by an overbar, the total variance of the velocity can be decomposed into two contributions:

$$\left\langle u^2 \right\rangle = \left\langle \overline{u}^2 \right\rangle + \left\langle u'^2 \right\rangle . \tag{4.3}$$

The first contribution $\left\langle \overline{u}^2 \right\rangle$ is associated with the spatial variations of the time averaged velocity. This spatial contribution is characterised by the random spatial distribution of the bubbles, and is not influenced by turbulence. The second contribution $\left\langle u'^2 \right\rangle$ is related to temporal fluctuations, and changes with the turbulence intensity. It is evident that the spatial and temporal contributions correspond to different physical mechanisms. Although it would be beneficial to decompose their separate contributions, this is currently not possible in the present experiments because the bubbles do not rise at constant velocity and move relative to each other. However, such a decomposition was accomplished using experimental investigations of an array of fixed spheres [14]. They found that the spatial contribution is more dominant than the temporal one in the vertical direction (see Figure 5 in Ref. [14]) up to Reynolds numbers ~ 1000. It was deduced that the spatial contributions are mainly responsible for the enhancement of the wake decay, in other words, the *-3* subrange scaling. Risso [24] theoretically showed that the superposition of independent random bubble disturbances may generate a continuous spectrum with a *-3* subrange. Recently Riboux *et al.* [11] numerically found that both the spatial and temporal contributions exhibited the *-3* subrange, which might be an explanation for why it is always observed in experiments. In our experiments, we vary the active-grid-induced turbulence intensity (and b parameter) by changing the mean flow speed. According to the discussion above, this means that we mainly change the temporal contributions, while the spatial contribution dominates in the explored parameter regime (at bubble Reynolds numbers ~ 1000). In our experiments, it is not possible to control (or

vary) the dominant spatial contribution. This is probably why we see the robust *-3* subrange for turbulent bubbly flow in a wide variety of conditions ($b > 0$) over 2-3 orders magnitude change in the b parameter. Hence, the *-3* spectrum scaling seems to be a generic feature in turbulent bubbly flow. Remarkably, the *-3* spectrum scaling is followed even at very small b parameter values (~ 0.01); i.e. when the void fraction is as low as 0.1%. Hence, the bubbles are able to modify the spectra very efficiently, even though they are present in small numbers, due to the long lifetime of their wakes. However, at extremely small bubble concentrations $\alpha \ll 0.1\%$ and $b \ll 0.01$ the Kolmogorov-like single-phase spectrum should be recovered, but we have no hint when this will happen. It would be relevant to find this transition in future work. The bubble concentration of the transition regime may be so small that optical methods like laser doppler anemometry (LDA) or particle image velocimetry (PIV) may become applicable, and even numerical approaches with fully-resolved wakes might be suitable for this purpose. In any case, it will be interesting to test until what limit of the b parameter the *-3* scaling still holds.

References

[1] M. Lance and J. Bataille, *Turbulence in the liquid phase of a uniform bubbly air–water flow*, J. Fluid Mech. **222**, 95 (1991).

[2] J. Rensen, S. Luther, and D. Lohse, *The effects of bubbles on developed turbulence*, J. Fluid Mech. **538**, 153 (2005).

[3] W. D. Deckwer, *Bubble column reactors*, 1st ed. (Wiley, UK, 1992).

[4] J. Magnaudet and I. Eames, *The Motion of High-Reynolds-Number Bubbles in Inhomogeneous Flows*, Ann. Rev. Fluid Mech. **32**, 659 (2000).

[5] P. Ern, F. Risso, D. Fabre, and J. Magnaudet, *Wake-induced oscillatory paths of freely rising or falling bodies*, Ann. Rev. Fluid Mech. **44**, 97 (2012).

[6] J. Martínez Mercado, D. Chehata Gómez, D. van Gils, C. Sun, and D. Lohse, *On bubble clustering and energy spectra in pseudo-turbulence*, J. Fluid Mech. **650**, 287 (2010).

[7] G. Riboux, F. Risso, and D. Legendre, *Experimental characterization of the agitation generated by bubbles rising at high Reynolds number*, J. Fluid Mech. **643**, 509 (2010).

[8] Z. Cui and L. Fan, *Turbulence energy distributions in bubbling gas-liquid and gas-liquid-solid flow systems*, Chem. Eng. Sci. **59**, 1755 (2004).

[9] R. Mudde, J. Groen, and H. van der Akker, *Liquid velocity field in a bubble column: LDA experiments*, Chem. Eng. Sci. **52**, 4217 (1997).

[10] S. Mendez-Diaz, J. C. Serrano-Garcia, R. Zenit, and J. A. Hernandez-Cordero, *Power spectral distributions of pseudo-turbulent bubbly flows*, Phys. Fluids **25**, 043303 (2013).

[11] G. Riboux, D. Legendre, and F. Risso, *A model of bubble-induced turbulence based on large-scale wake interactions*, J. Fluid Mech. **719**, 362 (2013).

[12] I. Mazzitelli and D. Lohse, *Evolution of energy in flow driven by rising bubbles*, Phys. Rev. E **79**, 066317 (2009).

[13] I. Roghair, J. Martínez Mercado, M. Van Sint Annaland, J. A. M. Kuipers, C. Sun, and D. Lohse, *Energy spectra and bubble velocity distributions in pseudo-turbulence: numerical simulations vs. experiments*, Int. J. Multi. Flow **37**, 1 (2011).

[14] F. Risso, V. Roig, Z. Amoura, G. Riboux, and A. Billet, *Wake attenuation in large Reynolds number dispersed two-phase flows*, Phil. Trans. R. Soc. A **366**, 2177 (2008).

[15] R. Poorte and A. Biesheuvel, *Experiments on the motion of gas bubbles in turbulence generated by an active grid*, J. Fluid Mech. **461**, 127 (2002).

[16] V. N. Prakash, Y. Tagawa, E. Calzavarini, J. Martinez Mercado, F. Toschi, D. Lohse, and C. Sun, *How gravity and size affect the acceleration statistics of bubbles in turbulence*, New J. Phys. **14**, 105017 (2012).

[17] J. Martínez Mercado, V. N. Prakash, Y. Tagawa, C. Sun, and D. Lohse, *Lagrangian statistics of light particles in turbulence*, Phys. Fluids **24**, 055106 (2012).

[18] R. Clift, J. R. Grace, and M. E. Weber, *Bubbles, Drops and Particles* (Academic, NY, USA, 1978).

[19] R. Zenit, D. Koch, and A. Sangani, *Measurements of the average properties of a suspension of bubbles rising in a vertical channel*, J. Fluid Mech. **429**, 307 (2001).

[20] J. Martínez Mercado, C. Palacios Morales, and R. Zenit, *Measurements of pseudoturbulence intensity in monodispersed bubbly liquids for $10<Re<500$*, Phys. Fluids **19**, 103302 (2007).

[21] T. van den Berg, W. D. Wormgoor, S. Luther, and L. D., *Phase-Sensitive Constant Temperature Anemometry*, Macromol. Mater. Eng. **296**, 230 (2011).

[22] F. Risso and K. Ellingsen, *Velocity fluctuations in a homogeneous dilute dispersion of high-Reynolds-number rising bubbles*, J. Fluid Mech. **453**, 395 (2002).

[23] S. Pope, *Turbulent flows* (Cambridge University Press, UK, 2000).

[24] F. Risso, *Theoretical model for k^{-3} spectra in dispersed multiphase flows*, Phys. Fluids **23**, 011701 (2011).

5

Three-dimensional Lagrangian Voronoï analysis for clustering of particles and bubbles in turbulence * †

Three-dimensional Voronoï analysis is used to quantify the clustering of inertial particles in homogeneous isotropic turbulence using data sets from numerics in the point particle limit and one experimental data set. We study the clustering behavior at different density ratios, particle response times (i.e. Stokes numbers St) and two Taylor-Reynolds numbers (Re_λ = 75 and 180). The Probability Density Functions (PDFs) of the Voronoï cell volumes of light and heavy particles show a different behavior from that of randomly distributed particles —i.e. fluid tracers—implying that clustering is present. The standard deviation of the PDF normalized by that of randomly distributed particles is used to quantify the clustering. The clustering for both light and heavy particles is stronger for the higher Re_λ. Light particles show maximum clustering for St around $1-2$ for both Taylor-Reynolds numbers. The experimental dataset shows reasonable agreement with the numerical results. The results are

*Published as: Y. Tagawa, J. M. Mercado, Vivek N. Prakash, E. Calzavarini, C. Sun, and D. Lohse, Three-dimensional Lagrangian Voronoi analysis for clustering of particles and bubbles in turbulence, J. Fluid Mech. 693, 201-215 (2012).

†Vivek N. Prakash contributed to the analysis, discussions and writing. The numerical simulations are from Enrico Calzavarini.

consistent with previous investigations employing other approaches to quantify the clustering. We also present the joint PDFs of enstrophy and Voronoï volumes and their Lagrangian autocorrelations. The small Voronoï volumes of light particles correspond to regions of higher enstrophy than those of heavy particles, indicating that light particles cluster in higher vorticity regions. The Lagrangian temporal autocorrelation function of Voronoï volumes shows that the clustering of light particles lasts much longer than that of heavy or neutrally buoyant particles. Due to inertial effects arising from the density contrast with the surrounding liquid, light and heavy particles remain clustered for much longer times than the flow structures which cause the clustering.

5.1 Introduction

The distribution of particles transported by turbulent flows is a current research topic with implications in diverse fields, such as process technology [1], cloud formation [2], and plankton dynamics [3]. In most of the cases, the particles have a finite size and a different density than the carrier fluid, i.e. they have inertia. These inertial particles cannot totally follow the fluid motion and distribute inhomogeneously within the turbulent flow, leading to clustering or preferential concentration [4]. The two relevant dimensionless parameters describing the dispersed inertial particles in the fluid are the density ratio $\beta = 3\rho_f/(\rho_f + 2\rho_p)$, where ρ_f and ρ_p are the densities of the carrier fluid and particle, respectively, and the Stokes number, St$= \tau_p/\tau_\eta$, where $\tau_p = a^2/3\beta\nu$ is the particle relaxation time, τ_η is the typical timescale of the flow, which for a turbulent flow is the Kolmogorov time scale, a is the particle radius, and ν is the kinematic viscosity of the fluid.

In recent years, both numerical and experimental studies have quantified the clustering of particles by employing different approaches like statistical analysis of single-point measurements [5], box-counting method [6, 7], pair correlation functions [8, 9]), Kaplan-Yorke dimension [10, 11], Minkowski functionals [11] and segregation indicators [11, 12]. It is not possible to obtain global information on bubble clustering from a single-point analysis [5]. Methods like box-counting and pair correlation functions, although useful, require the selection of an arbitrary length scale that affects the quantification of the clustering. The Kaplan-Yorke dimension, based on the calculation of the Lyapunov exponents, quantifies the contraction of a dynamical system by considering the separation rates of particle trajectories. Nevertheless, it does not provide global morphological information. Minkowski functionals, originally used to provide complete morphological information of the large-scale distribution of galaxies [13], have been applied to study the clustering of particles in turbu-

lent flows [11]. Calzavarini *et al.* [11] found that light particles cluster in filamentary structures, whereas heavy particles have a wall-like topology around interconnected tunnels, and obviously no clustering was observed for neutrally buoyant tracers. In the above numerical simulations and experiments, the strongest clustering was found for particles with St $\approx$ O(1). The problem with Minkowski-type analysis is that it is numerically expensive, and it does not provide information on the Lagrangian evolution of the clusters.

An alternative mathematical tool that can be used to study clustering is the Voronoï tessellation, which has been used in astronomy as a tool to characterize clustering of galaxies [14]. Recently, Monchaux *et al.* [15] have applied a Voronoï analysis to quantify the clustering of heavy particles in grid-generated turbulence. This Voronoï approach does not require the selection of an arbitrary length scale for a fixed particle number, and it can provide information on the Lagrangian statistics of clustering [15]. Monchaux *et al.* [15] have obtained two-dimensional particle positions by imaging a turbulent flow in a wind tunnel seeded with droplets. The Voronoï cells are defined based on the positions of the particles within the measurement domain. One can quantify the clustering by calculating the probability density function (PDF) of the normalized areas of the Voronoï cells. The PDF will have a different shape for inertial particles when compared to the corresponding PDF of randomly distributed particles. The main difference is observed at the small and large values of normalized areas, where the PDF of heavy particles has a higher probability than for randomly distributed particles. There is a central region where there is no significant difference between the PDFs of heavy particles and randomly distributed ones. The values of normalized areas at which the PDF deviates from the randomly distributed particles can be used as thresholds to classify Voronoï cells that belong either to clusters or voids. Monchaux *et al.* [15] report a maximum preferential concentration for St around unity, in agreement with other methods that have been used to study clustering.

The objective of the present chapter is to extend the work of Monchaux *et al.*[15] to: (i) three-dimensions and (ii) a much larger range of density ratios (including light, heavy, and neutrally buoyant particles) and Stokes numbers, i.e. we quantify particle clustering by applying 3D Voronoï analysis both for numerical and experimental data sets of particles and bubbles. Moreover, we (iii) correlate the clustering behavior of different particles with local turbulent flow quantities and (iv) study the Lagrangian temporal evolution of the clusters.

Table 5.1: Summary of the simulation and experimental parameters, where N is the size of the numerical domain, Re_λ is the Taylor-Reynolds number, η, τ_η are the Kolmogorov length and time scales, respectively, and $N_{particles}$ is the number of particles in the simulations, and the time-averaged particle number in the measurement volume for the experiment.

	N	Re_λ	η	τ_η	$N_{particles}$	St
Simulation A	128	75	0.0332	0.1104	1.0×10^3	0.1 - 4.0
Simulation B	512	180	0.001	0.0483	6.4×10^4	0.1 - 4.1
Experiment	-	162	288 μm	80 ms	1.3×10^3	0.04 ± 0.02

5.2 Experimental and Numerical Datasets and Voronoï analysis

5.2.1 Datasets

The numerical scheme for a dilute suspension (neglecting particle collisions) of point particles in homogeneous and isotropic turbulence is described as follows [11, 16]:

$$\frac{dv}{dt} = \beta \frac{D}{Dt} u(x(t),t) - \frac{1}{\tau_p}(v - u(x(t),t)) \tag{5.1}$$

where $v = dx/dt$ is the particle velocity and $u(x(t),t)$ the velocity field. The dimensionless numbers used to model the particle motion are the density difference between the particle and the fluid β and the Stokes number St. The values of β = 0, 1 and 3 correspond to very heavy particles, neutrally buoyant tracers, and very light particles (bubbles in water), respectively. When St = 0, the particles perfectly follow the fluid flow behaving as fluid tracers. As summarized in table 5.1, we explore a parameter space of β = 0, 1, and 3 and St ranging from 0.1 to 4.0 consisting of 24 values at Re_λ = 75 with the spatial resolution of $N = 128^3$. For Re_λ = 180 with $N = 512^3$, we study 5 different values of St = 0.1, 0.6, 1.6, 2.6, and 4.1 (from iCFD-database http://cfd.cineca.it; Calzavarini *et al.* [11]). The simulation of the Navier-Stokes equation is based on a 2/3 de-aliased pseudo-spectral algorithm with 2^{nd} order Adams–Bashforth time-stepping (for details see Bec *et al.* [10]). Simulations have been performed in a cubic box of side $L = 2\pi$ with periodic boundary conditions. The forcing adopted acts only at the largest scale, it is implemented by keeping constant the kinetic energy content in of the smallest shell ($|k| \leq 1$) in Fourier space. The intensity of the forcing is adjusted in such a way to have a turbulent dissipative scale (η)

of about 0.8 lattice grids in real space. Particle dynamics is evolved with time steps $O(10)$ times smaller than the smallest Stokes time, leading to an accurate resolution of the particle trajectories. Tri-linear interpolation is used to determine the value of the velocity field at the particle position. The numerical code was also validated by comparison against an independent code implementing different temporal integration scheme, different particles interpolation and different large scale forcing [17]. The simulations extends over few O(1) large-eddy-turnover times, this is enough for particles to reach a statistically steady distribution. In the present analysis, we fix the number of particles ($N_{particles}$) for given Reynolds numbers: 1000 particles for the simulation with the domain size of 128^3 at Re_λ = 75, and 6.4×10^4 particles for the simulation of 512^3 at Re_λ = 180. The number of particles normalized by the corresponding domain volume, i.e. the volume concentrations of the particles, for the two Re_λ are identical. In one particular case of Re_λ =75 and St = 0.6, the particle number is varied from 100 to 1×10^5.

We conduct experiments in the Twente Water Tunnel (TWT), an 8 m long vertical water tunnel designed for studying two-phase flows. By means of an active grid, nearly homogeneous and isotropic turbulence with Re_λ up to 300 can be achieved. A measurement section with dimensions $2\times0.45\times0.45$ m^3 with three glass walls provides optical access for the three-dimensional particle tracking velocimetry (PTV) system. Micro-bubbles with a mean radius of 170 $\pm$60 μm are generated by blowing pressurized air through a ceramic porous plate that is located in the upper part of the water tunnel. These micro-bubbles are advected downwards by the flow passing through the measurement section. In our three-dimensional particle tracking velocimetry (3D-PTV) micro-bubble experiments, we use a 4-camera system to get micro-bubble positions in the active-grid-generated turbulence in the TWT. The experimental data are collected for a duration of 6 seconds (three times the large eddy turnover time) at an acquisition rate of 1,000 fps. For the experimental data, Re_λ = 162, β = 3 and St = 0.04 $\pm$ 0.02, and the time-averaged number of particles inside the measurement volume of 70mm $\times$ 70mm $\times$70mm is 1.3×10^3 (for further details, see Refs. [18, 19]).

5.2.2 Voronoï analysis

The Voronoï diagram is a spatial tesselation where each Voronoï cell is defined at the particle location based on the distance to the neighboring particles [20]. Every point in a Voronoï cell is closest to the particle position compared to the neighboring particles, the exceptions are the vertices, borderlines and facets (see figure 5.1). Therefore, in regions where particles cluster, the volume of the Voronoï cells is smaller than that of the cells in neighboring regions. Hence, the volume of the Voronoï cells is in-

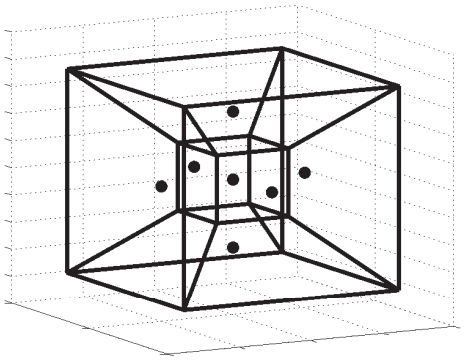

Figure 5.1: An example of a 3D Voronoï tesselation. The dots represent the particle position and lines represent the borders of the Voronoï cells.

versely proportional to the local particle concentration. The PDF of the Voronoï volumes normalized by the mean volume for randomly distributed particles can be well described by a Γ-distribution [21] (see figure 5.2). In the three-dimensional case, the Γ-distribution has the following prefactor and exponent:

$$f(x) = \frac{3125}{24} x^4 \exp(-5x). \tag{5.2}$$

Here x is the Voronoï volume normalized by the mean volume. Particles which are not randomly distributed will have a PDF that deviates from this Γ-distribution, indicating preferential concentration. The Voronoï cells of particles located near the edges of the domain are ill-defined, i.e. they either do not close or close at points outside of the domain. These cells at the border of the domain are not considered for the analysis.

5.3 Results

First, we present results on the effect of the density ratio (β) on the clustering, followed by the effect of the Stokes number (St) and the number of particles ($N_{particles}$). Then, we show how the volume of Voronoï cells ($\mathscr{V}$) and enstrophy are related. Finally, we present results on the Lagrangian autocorrelations of Voronoï volumes and enstrophy.

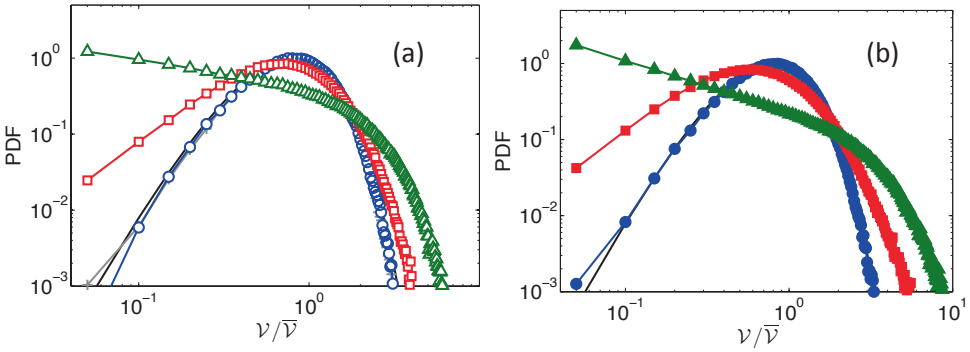

Figure 5.2: The normalized Voronoï volume PDFs for heavy (squares), neutrally buoyant (circles), and light particles (triangles) at St = 0.6 from direct numerical simulation (DNS) at (a) $Re_\lambda = 75$, and (b) $Re_\lambda = 180$. The thick line shows the Γ-distribution (eq. 5.2) for randomly distributed particles [21]; the PDF of the neutrally buoyant particles agrees well with the randomly distributed particles (+). Both heavy and light particles show clustering, however light particles show the maximum clustering.

5.3.1 Density effect

Here we study the clustering behavior of particles of different β at a fixed St for two different Re_λ. Figure 5.2 shows the PDFs of the Voronoï volumes ($\mathcal{V}$) normalized by their averaged volume ($\bar{\mathcal{V}}$), $\mathcal{V}/\bar{\mathcal{V}}$, for heavy, neutrally buoyant, and light particles of St = 0.6 at Re_λ =75 (Fig. 5.2 (a)), and 180 (Fig. 5.2 (b)). It clearly shows that the trends in the probability density functions are similar for both Re_λ. The PDF of neutrally buoyant particles follows the Γ-distribution (eq. 5.2) quite well, reflecting that neutrally buoyant particles do not have any preferential concentration. In contrast, the PDFs of light and heavy particles clearly show a different behavior compared to the randomly distributed particles. We observe that the probability of finding either small or large Voronoï volumes is higher for both light and heavy particles. The two regions of small and large volumes can be used to identify clusters and voids. The strongest clustering is observed for light particles, as the probability of finding small Voronoï volumes is the highest. Owing to the density difference, light particles accumulate in vortex filaments due to centrifugal forces [22–24], while heavy particles concentrate in regions of intense strain [10]. Here, although the heavy particles show clustering, it is less compared to light particles. These results are consistent with the Minkowski analysis by Calzavarini *et al.* [11].

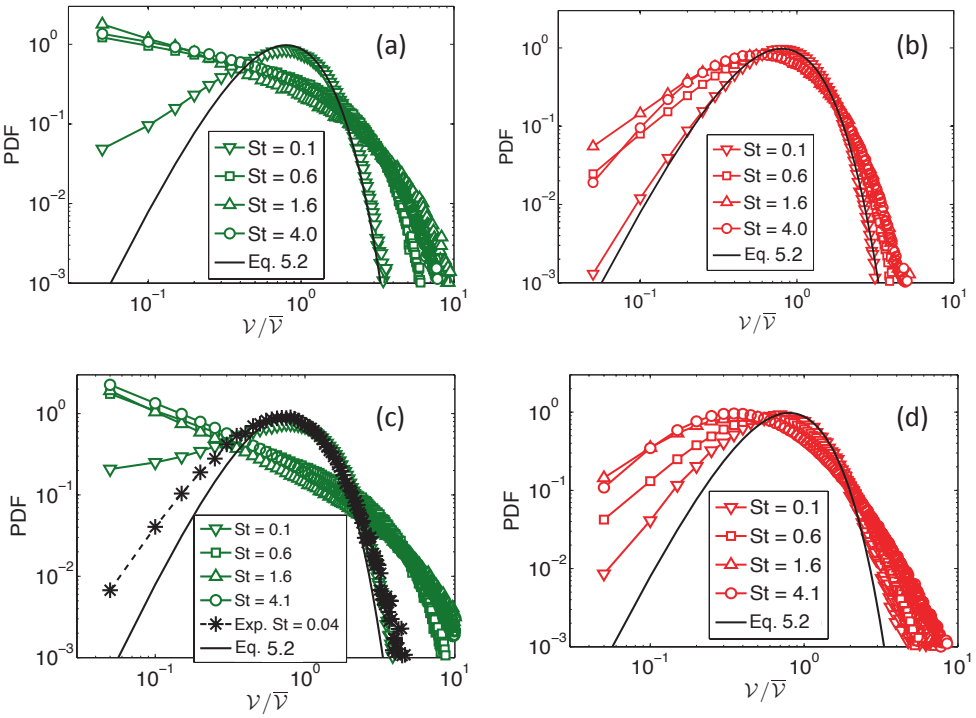

Figure 5.3: The normalized Voronoï volume PDFs for different St ranging from 0.1 to 4 in the numerics for (a) light particles β=3 at $Re_\lambda = 75$, (c) light particles β=3 at $Re_\lambda = 180$, (b) heavy particles β=0 at $Re_\lambda = 75$, and (d) heavy particles β=0 at $Re_\lambda = 180$. The stars in (c) correspond to the experimental result with St = 0.04 $\pm$ 0.02 at $Re_\lambda = 162$.

5.3.2 Stokes number effect

In this section, we study the effect of St on the clustering behavior for the three types of particles. We study the clustering behavior of the particles by examining the deviations of their Voronoï volume PDFs from the $\Gamma-$distribution.

Figure 5.3 shows PDFs of light (β=3) and heavy (β=0) particles for different St at Re_λ of 75 and 180. Firstly, we discuss the clustering of light particles as shown in Fig. 5.3 for Re_λ of (a) 75 and (b) 180. Both Reynolds numbers give a similar trend with increasing St. When St increases, the probability of finding clusters and voids increases up to a value of St = 1.6, after which the dependence becomes weaker for both Re_λ. We note that the experimental result, shown with stars in Fig. 5.3 (c), for

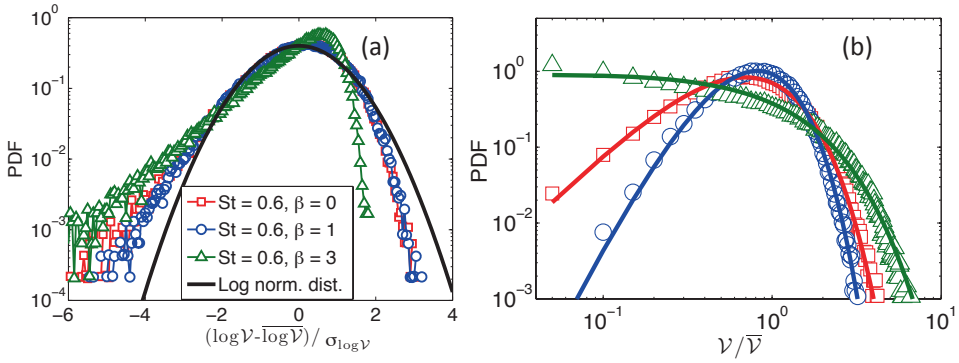

Figure 5.4: The comparison between log-normal and Γ−distribution of Eq. 5.3 fitting for the PDF of the 3D Voronoï volumes. Open symbols represent heavy (squares), neutrally buoyant (circles), and light particles (triangles) at St = 0.6 from DNS at $Re_\lambda = 75$; the lines represent (a) log-normal, and (b) Γ−distribution.

micro-bubbles with St = 0.04 ± 0.02 agrees reasonably well with the trend of the numerical data for light particles. In any case, for these small Stokes numbers, the PDF of the Voronoï volumes is still qualitatively similar to that of tracers. Another important feature of the light particle PDF is that the highest probability occurs at the smallest volume and decreases monotonically with increasing volume for St in the range of 0.6 to 4. As studied by Calzavarini *et al.* [11], bubbles in this range of St tend to get trapped in vortex filaments, leaving void regions. Thus, most of the bubbles are concentrated in small regions and there are few bubbles outside these small regions.

In general, the clustering of heavy particles is weaker as compared to that of light particles. For heavy particles, as shown in Fig. 5.3 (b,d), as St increases, the probability of finding clusters and voids increases up to a value of St = 1.6; then the St dependence changes for different Re_λ and is discussed below.

Monchaux *et al.* [15] found that the Voronoï area statistics of heavy particles can be well fitted by a log-normal distribution. For comparison, figure 5.4 (a) shows that the log-normal fitting for the PDFs of the present 3D Voronoï volumes for the three different type of particles. It is clear that the Voronoï volume statistics cannot be characterized well by the log-normal function, not even for the neutrally buoyant particles. However, the PDFs for all type of the particles can be fitted very well by

the $\Gamma-$distribution (see figure 5.4 (b)) with only one fitting parameter σ:

$$f(x) = \frac{1}{\sigma^{\frac{2}{\sigma^2}}\Gamma(\frac{1}{\sigma^2})} x^{\frac{1}{\sigma^2}-1} \exp^{-\frac{x}{\sigma^2}} \tag{5.3}$$

where, σ is the standard deviation of the Voronoï volumes. Hence σ provides a proper statistical quantification of Voronoï volumes.

In order to quantify the clustering using a single number, we use the standard deviation σ of the normalized Voronoï volume distributions. In figure 5.5 (a), we plot σ normalized by the standard deviation of the Voronoï volumes for randomly distributed particles σ_Γ. The magnitude of the indicator σ/σ_Γ distinguishes the behavior of light, neutrally buoyant, and heavy particles. A higher value of the indicator reflects stronger clustering for a given Re_λ. For neutrally buoyant particles there is no observed clustering, hence the indicator value is constant at 1. Heavy particles show clustering and the indicator value saturates at St $\approx$ 1-2 at Re_λ =75. However, the indicator value continuously increases with St at the higher Reynolds number of Re_λ =180, and the absolute value of the indicator σ/σ_Γ is larger for higher Re_λ. This indicates that the clustering of heavy particles is stronger at higher Re_λ for a given St. Fig. 5.5 (a) shows that the absolute value of the indicator σ/σ_Γ for light particles is also larger for higher Re_λ, revealing a stronger clustering for light particles at higher Re_λ. The reason for the Reynolds number effect could be because of the changing range of length scales of the vortex filaments which affect the clustering. At higher Re_λ, there is a wider range of clustering length scales resulting in a Voronoï volume distribution with a higher value of standard deviation. The curves corresponding to light particles show the strongest clustering, with a peak at St $\approx 1-2$ for both Re_λ = 75 and 180. This clustering result has a consistent trend with that of the Kaplan-Yorke analysis [11].

We also add the data point for the standard deviation of the experimental Voronoï volume PDF as shown in figure 5.5. Although the mean value of the indicator σ/σ_Γ for the experimental data is higher than those from the numerical simulations of light point particles, there is a good agreement with the numerical trend within the experimental error bar. More experimental data at larger Stokes numbers, i.e. larger bubbles, will be needed to come to a final conclusion on this issue.

5.3.3 Effects of the number of particles

In principle, one can expect different behaviors depending on the number density of particles. In the simulation dataset A, there are 10^5 particles available for one special case of Re_λ = 75 and St = 0.6. Using this snapshot, we study the effects of

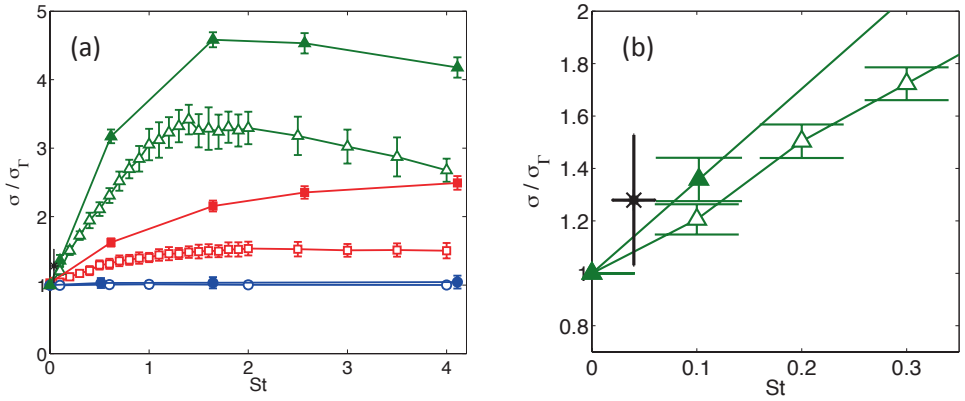

Figure 5.5: (a) Normalized standard deviation σ/σ_Γ (indicator) of the Voronoï volume distributions versus St for the two different Re_λ from DNS data. The symbols correspond to heavy (squares), neutrally buoyant (circles), and light particles (triangles). Open and filled symbols represent data at $Re_\lambda = 75$ and $Re_\lambda = 180$, respectively. The value of the indicator for neutrally buoyant particles remains constant at 1, i.e. clustering is not observed, whereas light particles show the most clustering with a peak at St ≈ 1.5 for both Re_λ. The experimental result of micro-bubbles is plotted with the star. (b) An enlarged plot showing only the results for light particles.

the particle number on the value of the clustering indicator σ/σ_Γ. We subsample data from this snapshot by selecting the required number particles and computing the Voronoï statistics. This subsampling procedure is randomized and then carried out at least 100 times for each case of particle number. Figure 5.6 shows the effect of varying the number of particles on the clustering indicator σ/σ_Γ and the error bars represent the standard deviation of all the subsamples of a given number of particles. In the present data set, the mean distances of particles are: 34.47η for $N_{particles}$=10^2, 16η for $N_{particles}$=10^3, 3.44η for $N_{particles}$=10^5, which are all above 1η. Hence, we are always studying situations where the mean particle distances are in the inertial range.

As shown in figure 5.6, for light and heavy particles the value of the indicator increases as the number of the particles is increased. The evolution of the value of the indicator σ/σ_Γ is steeper with increasing number of particles, and there seems to be no plateau region where the indicator value saturates. We do not understand the exact reason for this particle number dependence. One possible reason could be that the clusters have a complicated structure [11]. However, for a given number of particles, the indicator does show a consistent trend: a stronger clustering for light particles, weaker clustering for heavy particles, and no clustering for neutrally buoyant particles. Moreover, the error of the indicator calculated at $N_{particle}$ = 1000 is less than 4%. Therefore, at a fixed number of particles, the clustering indicator σ/σ_Γ of the Voronoï volume is robust. In the analysis that follows, we use the data of $N_{particles}$ = 1000 for the simulation with the domain size of $N = 128^3$ at Re_λ = 75 (simulation A).

5.3.4 Relation between the volume of the Voronoï cell and enstrophy

We relate the Voronoï volumes for the three different type of particles with turbulent flow quantities. A natural property for this comparison would be the enstrophy $\Omega = \omega^2/2$ (where ω is vorticity). Benzi *et al.* [25] have shown that different types of particles react sensitively to the local enstrophy at the particle position, reflecting their tendency to stay in regions with different vorticity contents. We thus calculate the joint PDF of Voronoï volumes and enstrophy for three types of particles at a fixed St = 0.6 for $Re_\lambda = 75$. For comparison, we also calculate the joint PDF for the case of neutrally buoyant particles with the smallest St available in the simulations (St = 0.1 and β = 1). The statistical behavior of these particles is expected to be close to that of ideal fluid tracers (St = 0 and β = 1). From now on, we refer to this case as the fluid tracer case. The Voronoï volume and the enstrophy are normalized by the mean values ($\mathscr{V}_{tr}$ and Ω_{tr}) of the fluid tracers. Figure 5.7 shows the joint PDFs of the normalized Voronoï volume ($\mathscr{V}/\mathscr{V}_{tr}$) and the normalized enstrophy (Ω/Ω_{tr})

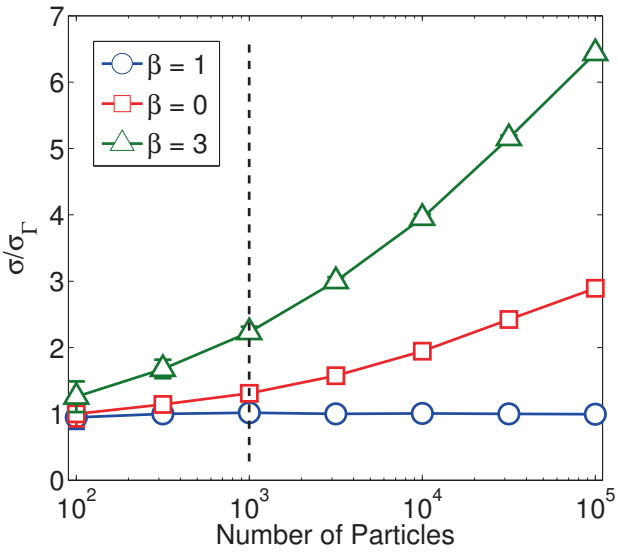

Figure 5.6: Normalized standard deviation of the Voronoï volume distributions as a function of number of particles taken from a snapshot case at $Re_\lambda = 75$. The dashed line shows the number of particles we used in the present work at $Re_\lambda = 75$ and St = 0.6 (simulation A).

for the different type of particles. The joint PDF for neutrally buoyant particles of St = 0.6, shown in figure 5.7 (c), is very similar to that of fluid tracers shown in figure 5.7 (a). We observe a clear difference in the joint PDF for heavy and light particles, as shown in figure 5.7 (b, d). The coordinates corresponding to the peak of the joint PDF $((\Omega/\Omega_{tr})^{max}_{jPDF}, (\mathscr{V}^p/\mathscr{V}_{tr})^{max}_{jPDF})$ is indicated by the crosses in the figure for each case. Compared to the tracer case, a slightly lower $(\mathscr{V}^p/\mathscr{V}_{tr})^{max}_{jPDF}$ and a lower $(\Omega/\Omega_{tr})^{max}_{jPDF}$ for heavy particles indicates more clustering at low enstrophy regions. The maximum value of the joint PDFs for the light particles is located at the region with a much higher enstrophy and a smaller Voronoï volume. This shows that the light particles shows strong clustering at high enstrophy regions.

The St dependence on the peak coordinates of the joint PDF $((\Omega/\Omega_{tr})^{max}_{jPDF}$, $(\mathscr{V}^p/\mathscr{V}_{tr})^{max}_{jPDF})$ is plotted in figure 5.8. As shown in figure 5.8 (a), the value of $(\mathscr{V}^p/\mathscr{V}_{tr})^{max}_{jPDF}$ for neutrally buoyant particles is nearly same with that of tracers at St from 0.1 to 4. The value of $(\mathscr{V}^p/\mathscr{V}_{tr})^{max}_{jPDF}$ for heavy particles is slightly smaller than unity for all St, indicating clustering. Figure 5.8 (a) also shows that the clustering for light particles is stronger as evidenced by the much smaller $(\mathscr{V}^p/\mathscr{V}_{tr})^{max}_{jPDF}$ compared to those of neutrally buoyant and heavy particles at all St. The minimum value of $(\mathscr{V}^p/\mathscr{V}_{tr})^{max}_{jPDF}$ indicating strongest clustering for the light particles is located at St = $1-2$, which is in excellent agreement with the results obtained using the indicator σ/σ_Γ (figure 5.5). The corresponding enstrophy at the peak $((\Omega/\Omega_{tr})^{max}_{jPDF})$ of the joint PDF versus St for the different particles is shown in figure 5.8 (b). The value of $(\Omega/\Omega_{tr})^{max}_{jPDF}$ for the heavy particles is smaller than unity, and it is much larger than unity for the light particles. This reflects the clustering of light particles in flow regions with very high enstrophy, whereas heavy particles cluster in low enstrophy regions for all St in the present study.

5.3.5 Voronoï Lagrangian autocorrelation

Finally, we conduct a Lagrangian analysis on the Voronoï volumes. For each type of particle we calculate the Lagrangian autocorrelation of its associated Voronoï volume. Figure 5.9 (a) shows a typical temporal evolution of Voronoï volumes for the three types of particles at St = 0.6 and $Re_\lambda = 75$. To compare the behavior of the three different particles, we choose particles with similar Voronoï volume at the starting time and trace their time evolution. While the Voronoï volumes of heavy and neutrally buoyant particles change frequently in time, it is clearly seen that light particles tend to have small values for longer times. This suggests that light particles are trapped in clustered regions for a long time and are suddenly ejected, as seen in figure 5.9 (a) around $\tau/\tau_\eta \approx 95$.

Figure 5.9 (b) shows the autocorrelation function $C_V(\tau)$ for heavy, neutrally

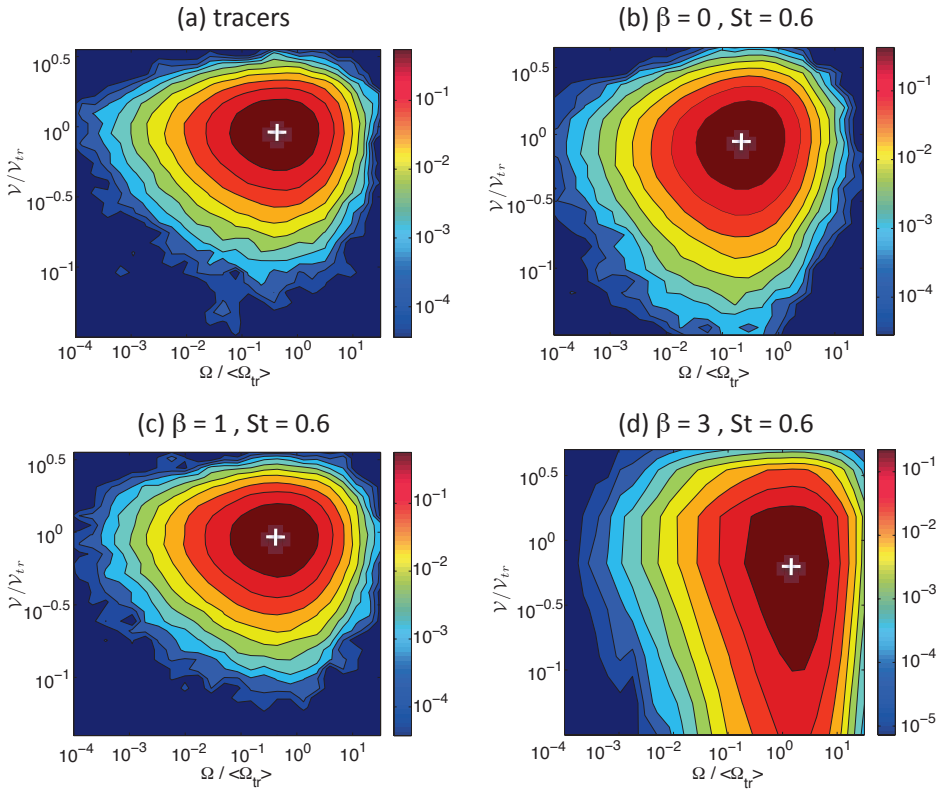

Figure 5.7: Joint PDFs of normalized Voronoï volumes and enstrophy for tracers and particles at St = 0.6 for $Re_\lambda = 75$: (a) fluid tracers, (b) heavy particles, (c) neutrally buoyant particles, and (d) light particles. The cross indicates the location of the maximum probability (peak) for each case.

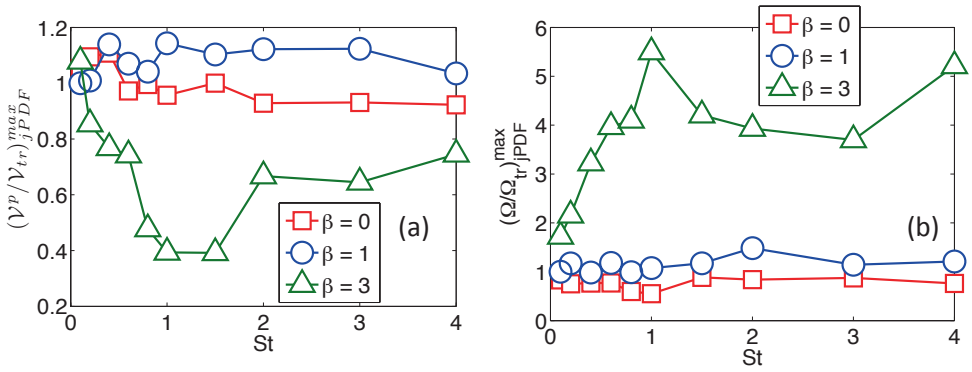

Figure 5.8: The coordinates of the peak of the Joint PDFs of normalized Voronoï volumes and enstrophy as a function of St: (a) $\mathscr{V}^p/\mathscr{V}_{tr}$ versus St, (b) Ω^p/Ω_{tr} versus St.

buoyant, and light particles at a fixed St = 0.6 and $Re_\lambda = 75$. We define the decorrelation time τ_V as the time when the autocorrelation function has decreased to 1/2, i.e., $C_V(\tau_V) = 1/2$. As shown in figure 5.9 (b), the decorrelation time for light particles is around $\tau_V \sim 7\tau_\eta$, whereas for heavy and neutrally buoyant particles decorrelation already occurs around $4\tau_\eta$. Thus the clustering of light particles lasts for a longer time as compared to heavy and neutrally buoyant particles. As shown by Calzavarini *et al.* [11], light particles accumulate in filamentary structures and heavy ones tend to cluster outside these structures to form wall-like interconnected tunnels. These differences in the morphology of the clustered particles could be a possible reason for the light particles being clustered for a longer time as compared to heavy particles.

We also compare the autocorrelation time scale of the Voronoï volumes to that of the enstrophy shown in figure 5.9(c) for the same St and Re_λ. First, as expected, for neutrally buoyant particles, the Lagrangian decorrelation time for the Voronoï volumes is comparable to that of the enstrophy (τ_Ω), i.e. $\tau_\Omega \sim \tau_V \sim 4\tau_\eta$, because the neutrally buoyant particles do not cluster. However, remarkably, for light particles the decorrelation time of the Voronoï volumes is much larger, $\tau_V \sim 7\tau_\eta$, i.e., more than twice as large as the autocorrelation time scale $\tau_\Omega \sim 3\tau_\eta$ of the enstrophy itself. For heavy particles, the Lagrangian decorrelation time of the Voronoï volumes is around $\tau_V \sim 4\tau_\eta$, which is also about two times that of enstrophy $\tau_\Omega \sim 2\tau_\eta$.

We also study the St dependence of the decorrelation time scales of Voronoï volume (τ_V) and enstrophy (τ_Ω) at $Re_\lambda = 75$ for heavy, neutrally buoyant, and light

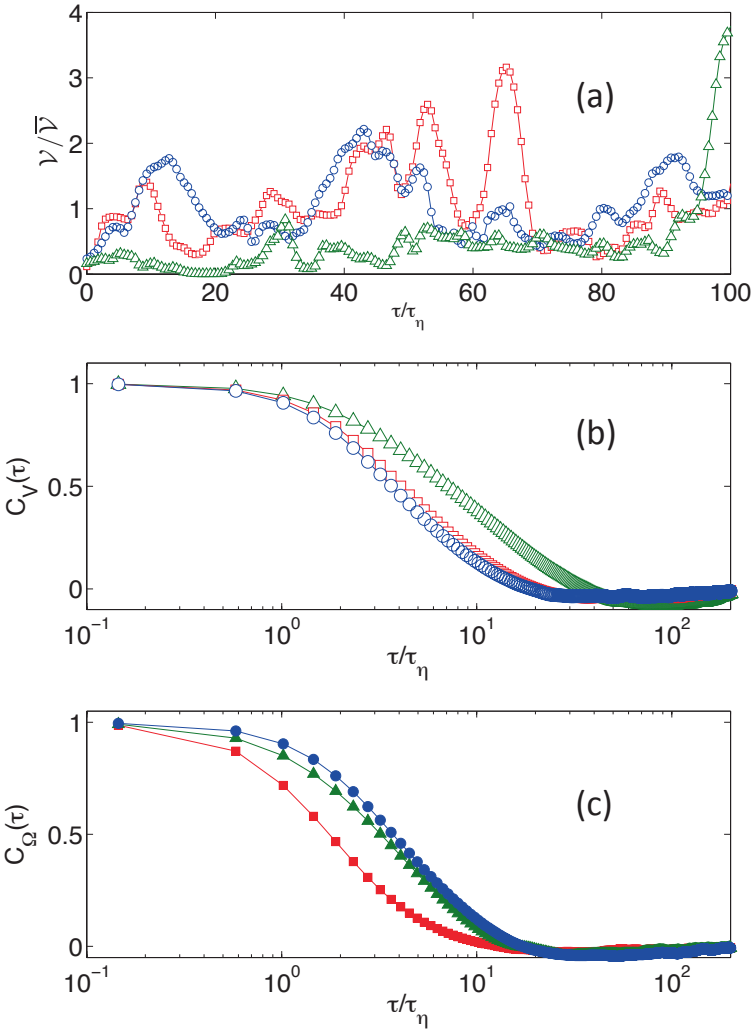

Figure 5.9: Lagrangian Voronoï analysis for heavy (squares), neutrally buoyant (circles), and light particles (triangles) at St = 0.6 and $Re_\lambda = 75$. (a) Temporal evolution of Voronoï volumes. (b) Temporal autocorrelation functions of Voronoï volumes. (c) Temporal autocorrelation functions of enstrophy.

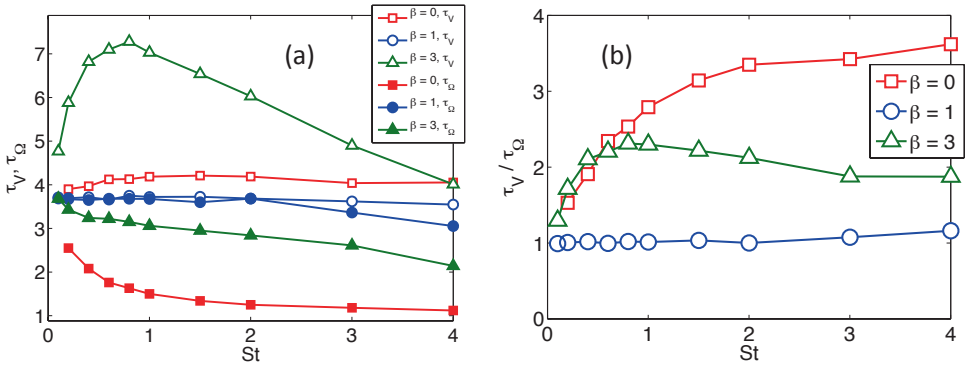

Figure 5.10: (a) Decorrelation time of Voronoï volume (τ_V) and enstrophy (τ_Ω) as a function of St at $Re_\lambda = 75$ for heavy (squares), neutrally buoyant (circles), and light particles (triangles). Open and filled symbols represent decorrelation time of Voronoï volume and enstrophy, respectively. (b) The ratio of decorrelation times (τ_V / τ_Ω) as a function of St.

particles as shown in figure 5.10 (a). We observe that τ_V for light particles is always larger than heavy and neutrally buoyant particles in the St range 0.1 to 4, with a peak around St unity. This suggests that the light particles cluster for a longer time in the range of studied St.

It is well known that flow regions of high enstrophy trap bubbles and regions with intense strain accumulate heavy particles. Figure 5.10(a) also shows that τ_V for both light and heavy particles is much larger than their decorrelation time of enstrophy τ_Ω for all St from 0.1 to 4. This is more clearly seen in figure 5.10(b) where the ratio τ_V/τ_Ω for both light and heavy particles is greater than unity for all St, while this ratio is always close to unity for the neutrally buoyant particles. Remarkably, this means that the lifetimes of the clustered bubbles and heavy particles are much longer than the lifetime of the trapping flow structures themselves. The interpretation is that clustered particles are constrained in different regions of the flow and due to their inertia need time to reorganize themselves in the flow after sudden changes in flow conditions. However, neutrally buoyant particles do not have this constraint and are distributed more evenly at any given time in the flow. Figure 5.10(b) shows that the ratio τ_V/τ_Ω for light particles has a weakly decreasing trend at St larger than unity. The ratio τ_V/τ_Ω for heavy particles monotonically increases with increasing St, and it is larger compared to light particles for St > 0.5.

5.4 Conclusion

We use three-dimensional Voronoï analysis to study particle clustering in homogenous isotropic turbulence with both numerical data in the point particle limit and one experimental data set. The analysis is applied to inertial particles (light, neutrally buoyant, and heavy) of different density ratios β, St ranging from 0.1 to 4 and two different Taylor-Reynolds numbers (Re_λ = 75 and 180). In the entire range of parameters covered, the Voronoï volume PDFs of neutrally buoyant particles agree well with the Γ-distribution for randomly distributed particles. At a fixed value of St, the PDFs of Voronoï volumes of light and heavy particles show higher probability to have small and large Voronoï volumes than randomly distributed particles, reflecting the clustering behavior. The standard deviation of normalized Voronoï volumes σ/σ_Γ is used as an indicator to quantify the clustering. Heavy particles show some clustering, and light particles have a much stronger clustering. Both heavy and light particles show a stronger clustering for a higher Re_λ. The maximum clustering for light particles is around St $\approx$ 1-2 for both Taylor-Reynolds numbers, and this maximum clustering range has a consistent trend with that of the Kaplan-Yorke analysis. We check the effect of number of particles on the value of the indicator and find that the clustering trend is robust for a given number of particles.

For one (small) Stokes number St = 0.04 $\pm$ 0.02 we have also extracted the three-dimensional Voronoï volume PDF from experimental data. Though the PDF fits into the general trend – at these small Stokes numbers the PDF nearly follows a Γ-distribution – a quantitative analysis shows that the experimental PDF of 3D Voronoï volumes is slightly broader than what is obtained from point-particle simulations. More experiments with larger Stokes numbers will have to be done to judge whether this is a limitation of the point-particle approach, a consequence of the neglect of two-way and four-way coupling in the numerics, or whether the experimental data are not precise enough. From our point of view, the Voronoï analysis is an excellent means to quantitatively compare clustering effects of particles in experimental and numerical data sets.

Finally, we show that the Voronoï analysis can be connected to local flow properties like enstrophy. By comparing the joint PDFs of enstrophy and Voronoï volumes and their Lagrangian autocorrelation, the clustering behavior of heavy, neutrally buoyant, and light particles can further be distinguished. It is found that the light particles strongly cluster in flow regions with very high enstrophy, whereas heavy particles weakly cluster in low enstrophy regions for all St in the present study. From the Lagrangian autocorrelation of Voronoï volumes we conclude that the clustering of light particles lasts much longer than that of heavy or neutrally buoyant particles. And because of inertial effects due to the density difference from the carry-

ing fluid, light and heavy particles remain clustered for a much longer time than the flow structures themselves.

References

[1] S. Pratsinis and S. Vemury, *Particle formation in gases: a review.*, Powder Technology **88**, 267 (1996).

[2] E. Bodenschatz, S. P. Malinowski, R. A. Shaw, and F. Stratmann, *Can We Understand Clouds Without Turbulence?*, Science **327**, 970 (2010).

[3] F. Schmitt and L. Seuront, *Intermittent turbulence and copepod dynamics: increase in encounter rates through preferential concentration*, J. Mar. Syst. **70**, 263 (2008).

[4] F. Toschi and E. Bodenschatz, *Lagrangian properties of particles in turbulence*, Annu. Rev. Fluid Mech. **41**, 375 (2009).

[5] E. Calzavarini, T. van der Berg, F. Toschi, and D. Lohse, *Quantifying microbubble clustering in turbulent flow from single-point measurements*, Phys. Fluids **20**, 040702 (2008).

[6] J. Fessler, J. Kulick, and J. Eaton, *Preferential concentration of heavy particles in a turbulent channel flow*, Phys. Fluids **6**, 3742 (1994).

[7] A. Aliseda, A. Cartellier, F. Hainaus, and J. Lasheras, *Effect of preferential concentration on the settling velocity of heavy particles in homogeneous isotropic turbulence*, J. Fluid Mech. **468**, 77 (2002).

[8] L. Chen, S. Goto, and J. Vassilicos, *Turbulent clustering of stagnation points and inertial particles*, J. Fluid Mech. **553**, 143 (2006).

[9] E. Saw, R. Shaw, S. Ayyalasomayajula, P. Chuang, and A. Gylfason, *Inertial clustering of particles in high-Reynolds-number turbulence*, Phys. Rev. Lett. **100**, 214501 (2008).

[10] J. Bec, L. Biferale, G. Boffetta, A. Celani, M. Cencini, A. Lanotte, S. Musacchio, and F. Toschi, *Acceleration statistics of heavy particles in turbulence*, J. Fluid Mech. **550**, 349 (2006).

[11] E. Calzavarini, M. Kerscher, D. Lohse, and F. Toschi, *Dimensionality and morphology of particle and bubble clusters in turbulent flow*, J. Fluid Mech. **607**, 13 (2008).

[12] R. IJzermans, M. Reeks, E. Meneguz, M. Picciotto, and A. Soldati, *Measuring segregation of inertial particles in turbulence by a full Lagrangian approach*, Phys. Rev. E **80**, 015302 (2009).

[13] M. Kerscher, K. Mecke, J. Schmalzing, C. Beisbart, T. Buchert, and H. Wagner, *Morphological fluctuations of large-scale structure: the PSCz survey*, Astron. Astrophys. **373**, 1 (2001).

[14] R. van de Weygaert and V. Icke, *Fragmenting the universe. II. Voronoi vertices as Abell clusters*, Astron. Astrophys. **213**, 1 (1989).

[15] R. Monchaux, M. Bourgoin, and A. Cartellier, *Preferential concentration of heavy particles: A Voronoi analysis*, Phys. Fluids **22**, 103304 (2010).

[16] M. Maxey and J. Riley, *Equation of motion for a small rigid sphere in a nonuniform flow*, Phys. Fluids **26**, 883 (1983).

[17] F. Toschi, L. Biferale, E. Calzavarini, A. Scagliarini, and E. Leveque, *Lagrangian modeling and properties of particles with inertia.*, Advances in Turbulence, XII, Proceedings of the 12th European Turbulence Conference (ETC-12), Marburg (D), Springer Proceedings in Physics. (2009).

[18] J. Martínez Mercado, D. Chehata Gómez, D. van Gils, C. Sun, and D. Lohse, *On bubble clustering and energy spectra in pseudo-turbulence*, J. Fluid Mech. **650**, 287 (2010).

[19] J. Martínez Mercado, V. N. Prakash, Y. Tagawa, C. Sun, and D. Lohse, *Lagrangian statistics of light particles in turbulence*, Phys. Fluids **24**, 055106 (2012).

[20] A. Okabe, B. Boots, K. Sugihara, and S. Chiu, *Spatial tesselations*, 1st ed. (John Wiley & Sons, UK, 2000).

[21] J. Ferenc and Z. Néda, *On the size distribution of Poisson Voronoi cells*, Physica. A **385**, 518 (2007).

[22] I. Mazzitelli, D. Lohse, and F. Toschi, *On the relevance of the lift force in bubbly turbulence*, J. Fluid Mech. **488**, 283 (2003).

[23] I. Mazzitelli and D. Lohse, *Lagrangian statistics for fluid particles and bubbles in turbulence*, New J. Phys. **6**, 203 (2004).

[24] L. Biferale, A. Scagliarini, and F. Toschi, *On the measurement of vortex filament lifetime statistics in turbulence*, Phys. Fluids **22**, 065101 (2010).

[25] R. Benzi, L. Biferale, E. Calzavarini, D. Lohse, and F. Toschi, *Velocity-gradient statistics along particle trajectories in turbulent flows: The refined similarity hypothesis in the Lagrangian frame*, Phys. Rev. E **80**, 066318 (2009).

6

The clustering morphology of freely rising deformable bubbles * †

We investigate the clustering morphology of a swarm of freely rising deformable bubbles. A three-dimensional Voronoï analysis enables us to quantitatively distinguish between two typical preferential clustering configurations: a regular lattice arrangement and irregular clustering. The bubble data is obtained from direct numerical simulations (DNS) using the front-tracking method. It is found that the bubble deformation, represented by the aspect ratio χ, plays a significant role in determining which type of clustering is realized: nearly spherical bubbles form a regular lattice arrangement, while more deformed bubbles show irregular clustering. Remarkably, this criteria for the clustering morphology holds for different diameters of the bubbles, surface tension, and viscosity of the liquid in the studied parameter regime. The mechanism of this clustering behavior is most likely connected to the amount of vorticity generated at the bubble surfaces.

*Published as: Y. Tagawa, I. Roghair, Vivek N. Prakash, M. van Sint Annaland, H. Kuipers, C. Sun, and D. Lohse, The clustering morphology of freely rising deformable bubbles, J. Fluid Mech. 721, R2 (2013)

†Vivek N. Prakash contributed to the analysis, discussions and writing. The numerical simulations are from Ivo Roghair.

6.1 Introduction

Particles dispersed in a flow can distribute inhomogeneously, showing clustering or preferential concentration behavior. This is attributed to the interaction between the two phases, and the inertia of the particles [1, 2]. A swarm of bubbles rising in a quiescent liquid is a subset of the general case of particles dispersed in a complex flow. This topic of bubbly flow has applications in bubble columns that are important in the chemical industry, in chemical processes such as oxidation, chlorination, in water treatment, and in the steel industry [3]. Freely rising bubbles in an originally still liquid are known to induce liquid velocity fluctuations which result in the so-called "pseudo-turbulence". Bubble clustering in pseudo-turbulence has attracted much attention because of its importance in applications, and lack of understanding of the fundamental physics [4–7]. Bunner & Tryggvason [8, 9] have conducted numerical simulations and found that deformability of the bubbles plays an important role in the clustering phenomenon: bubbles with small deformability (spherical bubbles) show a horizontal alignment, while deformed bubbles display clustering in the vertical direction. Meanwhile, experiments have found both horizontal and vertical clustering depending on parameters like bubble deformation, size, and other flow properties [4, 6, 10].

In the present chapter, the bubble data are obtained from direct numerical simulations of a swarm of rising bubbles. The bubble clustering in the same dataset was previously studied using the angular pair correlation [11]. Here, we revisit the issue of bubble clustering, using a Voronoï analysis technique, which has been proven to be a powerful tool for quantifying the clustering behavior of bubbles and particles in fluid flow (see for e.g. Refs. [12–14]). We extend the Voronoï analysis to study the geometric morphology of the clusters formed by freely rising deformable bubbles.

6.2 Voronoï analysis for clustering morphology

In the method of Voronoï tesselations, each Voronoï cell is defined at a particle location based on its neighbors [15]. Every point inside a Voronoï cell is the nearest to the particle location compared to the neighbors; the exceptions being borderlines, vertices, and facets, which have the same distance between two or more particles. In a given three-dimensional distribution of particles, if the volume of the Voronoï cells is smaller compared to the cells in neighboring regions, then the particles belong to a clustering region. It has been found that a Γ-distribution can well describe the Probability Density Functions (PDF) of the Voronoï volumes of randomly distributed

particles in three-dimensions [16], namely

$$f(x) = \frac{3125}{24} x^4 \exp(-5x), \tag{6.1}$$

where $x = \mathscr{V}/\overline{\mathscr{V}}$ is the Voronoï volume $\mathscr{V}$ normalized by the mean volume $\overline{\mathscr{V}}$. Such a random distribution of particles, and their corresponding Voronoï cells are shown in the upper panel of figure 6.1(b). In the lower panel of figure 6.1(b), the corresponding Γ-distribution fitted PDF is shown. Particles which are not randomly distributed will have a PDF that deviates from this Γ-distribution.

Figure 6.1 shows examples of different particle arrangements. In figure 6.1(a), the particles prefer to aggregate in a small central region, accompanied by void regions. We refer to this situation as 'irregular clustering'. In this case, the probabilities of small and large Voronoï volumes are higher than the Γ-distribution. In figure 6.1(c) particles keep the same distance between each other, having the same size Voronoï cells. Therefore, the size distribution becomes narrower compared to the case of randomly distributed particles. We refer to this situation as a 'regular lattice arrangement'. Tagawa *et al.* [13] found that these distributions can be well fitted by a $\Gamma-$distribution with a single fitting parameter σ, which is the standard deviation of Voronoï volumes. Furthermore, this parameter σ can be used for a quantification of the particle clustering. In this work, we use σ to investigate the morphology of the bubble clustering. Here σ is normalized by the standard deviation of randomly distributed particles σ_{rnd}. The indicator is (see figure 6.1): $\sigma/\sigma_{rnd} > 1$ for irregular clustering, $\sigma/\sigma_{rnd} = 1$ for a random distribution, and $\sigma/\sigma_{rnd} < 1$ for a regular lattice arrangement.

In the application of the Voronoï analysis on the present numerical data, there are two specific issues that are addressed below. First, the Voronoï cells of particles located near the edges of the domain are not well-defined, i.e. the Voronoï cells either do not close or close at points outside of the domain. These Voronoï cells located near the domain edges are usually discarded from the Voronoï analysis (as in Ref. [13]). However, in the present data, the number of bubbles in the domain are small. In this case, we cannot afford to ignore the edge cells, as doing so will result in poor statistics. We take advantage of the periodic boundary condition of the numerics to overcome this problem. The periodic boundary condition enables us to form a box ($3\times3\times3$ larger, and including all particles) surrounding the original box. We then apply the three-dimensional Voronoï tesselation on the particle positions in this larger box. We can now ignore the cell edges on this larger box, as we have sufficient number of particles for good statistics. Also, if one considers the central box, although some Voronoï cells protrude into the neighboring boxes, the total volume is still conserved owing to the periodic boundary conditions. This is an added advantage of this

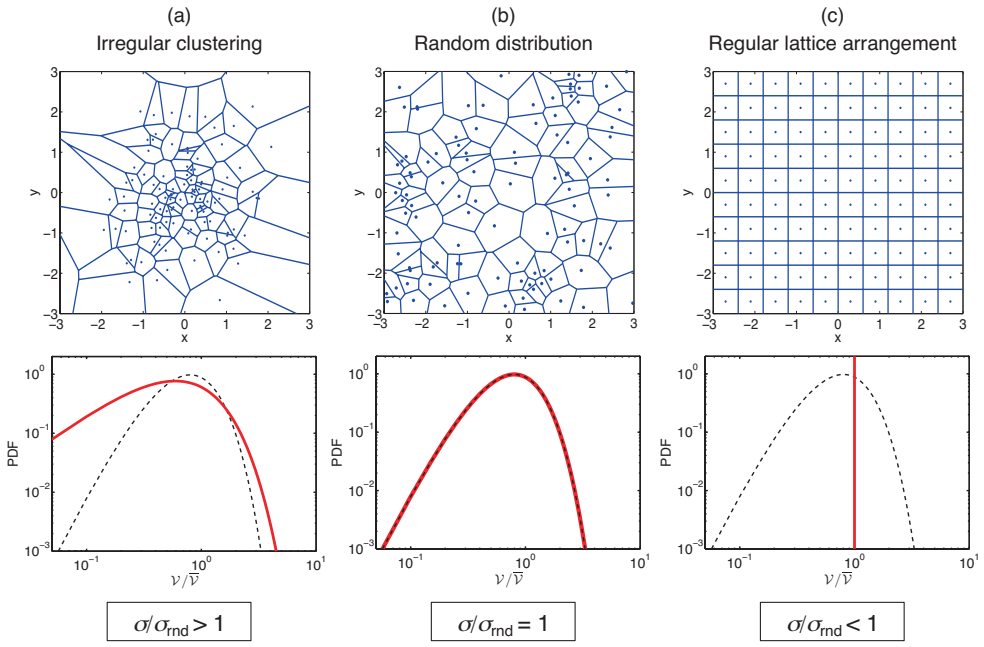

Figure 6.1: Examples of the different types by which a fixed number (in this case 100) of particles can be spatially distributed: (a) irregular clustering (b) random distribution, and (c) regular lattice arrangement. The upper panels show the Voronoï tesselations based on the particle positions in two dimensions, for ease of illustration. The lower panels show the corresponding Probability Density Functions (PDFs) of the Voronoi Volumes (the three-dimensional case). In each case, the PDF corresponding to the upper panel (thick red line) is compared with the PDF of the randomly distributed particles (dashed black line). The value of the clustering indicator (i.e. the standard deviation of the PDFs normalized by that of randomly distributed particles, σ/σ_{rnd}) is also shown below the PDF.

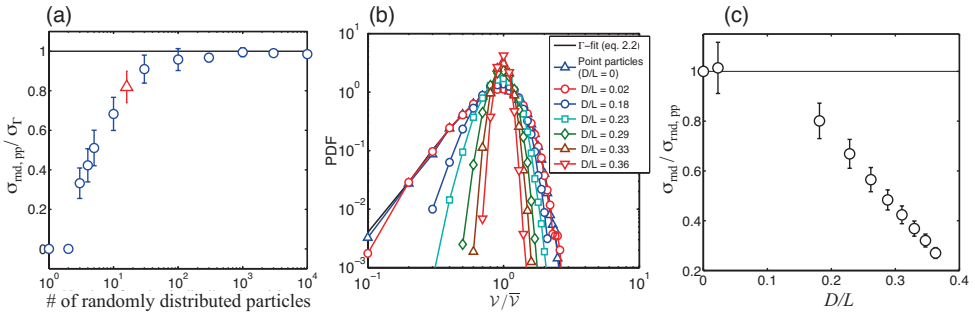

Figure 6.2: (a) The standard deviation of Voronoï volumes as a function of the number of randomly distributed point-like particles in a periodic box. The standard deviations are normalized by the standard deviation $\sigma_\Gamma = 0.4472$ for an infinite number of particles ($> 10^6$) in a box, as shown by Ferenc & Neda [16]. In the present datasets, we consider 16 bubbles in a periodic box, and the corresponding datapoint is indicated using the red triangle. (b) The PDFs of Voronoï volumes for randomly distributed spheres at different sphere-domain length ratios D/L. The Γ-fit for 16 spheres expressed by equation (6.2) with $\sigma_{rnd,pp}$ (thin black line) and the PDF for randomly distributed point-like particles agree well. The shape of the PDFs becomes narrower with increasing D/L due to the finite-size effect. (c) The standard deviations of Voronoï volumes σ_{rnd} normalized by that for the point-particle case $\sigma_{rnd,pp}$ as a function of D/L. The value $\sigma_{rnd}/\sigma_{rnd,pp}$ decreases with increasing D/L.

method.

Secondly, the number of particles available for the Voronoï analysis is a key parameter that can significantly affect the results (see Fig.6 in Ref. [13]). We check the dependence of the number of particles on the standard deviation of Voronoï volumes in figure 6.2(a) for randomly distributed point-like particles. We vary the number of particles inside each of the boxes that are replicated to form the larger box as mentioned above. The Voronoï tesselations are applied and the standard deviation of Voronoï volumes for each case of the varying number of particles is shown in figure 6.2(a). Also, the standard deviation of Voronoï volumes is normalized by that of randomly distributed particles with numbers $>10^6$ [16]. Each error bar has been calculated by repeating this procedure more than 10^4 times. We see in figure 6.2(a) that when the particle number is less than 100, the value of the standard deviation changes quite significantly. We note the peculiarity that, when a box includes just one or two particle(s), the Voronoï volumes are the same or half of the volume of the domain, respectively, and hence the standard deviation is zero. For a larger number of

particles, the standard deviation grows with increasing number of particles and shows an asymptotic behavior, and saturates to the value of unity when the particle numbers approach $\sim$ 1000. In the previous chapter [13], we have used a value of σ/σ_Γ=1 for the Voronoï analysis, as we had 1000 particles in our simulations. In the present chapter, the number of bubbles used in the numerical simulations is 16. In this case, figure 6.2(a) gives the corresponding value of the standard deviation as $\sigma_{rnd,pp}/\sigma_\Gamma$ = 0.82. We account for this change by using $\sigma_{rnd,pp} = 0.82\sigma_\Gamma$ in the equation which describes the Voronoï volume PDF fit using the single parameter σ [13] :

$$f(x) = \frac{1}{\sigma^{(2/\sigma^2)}\Gamma(\frac{1}{\sigma^2})} x^{(1/\sigma^2)-1} \exp^{-(x/\sigma^2)}. \tag{6.2}$$

This equation indeed results in a nice fit as shown in figure 6.2(b), where we plot the Voronoï volume PDF for 16 randomly distributed particles (blue upward-pointing triangles) and the curve from equation (6.2) (thin black line).

All the above discussions were devoted to point-like particles, but in this chapter we consider bubbles with a finite-size (D =1-3.5 mm). Table 6.1 lists the different parameters used in the numerics. Thus, we need to first understand the effect of finite particle size on the Voronoï volume distributions. For this, we artificially generate random positions in three-dimensions (see § 6.3) for 16 perfect spheres of diameter D and change the domain size L to vary the sphere-domain length ratio D/L. This sphere-domain length ratio D/L is related to the void fraction α by the expression: $D/L = (3\alpha/8\pi)^{1/3}$. For clarity of presentation, we have chosen to describe the clustering results using D/L instead of α. In figure 6.2(b) we show the Voronoï volume PDFs for the 16 randomly distributed spheres at different D/L. The PDF of the Voronoï volume for the randomly distributed point particles and for spheres at the small value of D/L = 0.02 show quite a similar behavior, i.e. the finite-size effect is then negligible. The finite-size effects become more significant with increasing D/L, and this is seen in the shape of the PDF. The PDFs become narrower with increasing D/L, implying that the bubbles are distributed more evenly throughout the domain. At a large value of D/L, each of the spheres occupies a relatively larger volume in the box, which reduces the available free-space (for other spheres), leading to a more constrained distribution and narrower PDF shape.

The standard deviations of the Voronoï volume PDFs as a function of D/L are shown in figure 6.2(c). The values σ_{rnd} are normalized by the standard deviation obtained from the Γ-distribution fit for randomly distributed point particles, $\sigma_{rnd,pp}$. The indicator $\sigma_{rnd}/\sigma_{rnd,pp}$ decreases monotonically with D/L, starting at 1 (at D/L = 0) and reduces to $\sim$1/5 for $D/L = 0.36$, clearly indicating the effect of finite-size. The normalization of the clustering indicator $\mathscr{C} = \sigma(D/L)/\sigma_{rnd}(D/L)$ for each case

used in the discussion below is carried out at the same bubble-domain length ratio D/L, in order to fully focus on dynamical effects. For the case of deformable bubbles to be discussed below, there will be variations in the bubble eccentricity, which is difficult to take into account while defining a standard case for normalization of the clustering indicator. Hence, we choose the reference case of artificially generated spheres to present our results below.

6.3 Numerical method

Three-dimensional direct numerical simulations (DNS) have been performed to simulate bubbles rising in a swarm, using periodic boundary conditions in all directions to mimic an 'infinite' swarm without wall effects, similarly to what has been done by Bunner & Tryggvason [8]. The simulations have been carried out using a model that incorporates the front-tracking (FT) method [17], which tracks the interfaces of the bubbles explicitly using Lagrangian control points distributed homogeneously over the interface. Compared to interface reconstruction techniques, such as volume-of-fluid or level-set methods, the advantage of the FT method is that the bubbles are able to approach each other closely (within the size of one grid cell) and can even collide, while preventing (artificial) merging of the interfaces. Therefore, the size of the bubbles remains constant throughout the simulation. Especially for bubble swarm simulations with high void fractions as studied in this work, this is an important aspect. In addition, the interface is sharp allowing the surface tension force to act at the exact position of the interface.

In our model (see Ref. [18, 19] for details), the fluid flow is solved by the discretised incompressible Navier-Stokes equations on a Eulerian background mesh consisting of cubic computational cells:

$$\rho \frac{\partial \vec{u}}{\partial t} + \rho \nabla \cdot (\vec{u}\vec{u}) = -\nabla p + \rho \vec{g} + \nabla \cdot \mu \left[\nabla \vec{u} + (\nabla \vec{u})^T \right] + \vec{F}_\gamma, \qquad \nabla \cdot \vec{u} = 0 \tag{6.3}$$

where $\vec{u}$ is the fluid velocity and $\vec{F}_\gamma$ representing a singular source-term accounting for the surface tension force at the interface (see below). The flow field of both phases is resolved using a one-fluid formulation where the physical properties are determined from the local phase fraction. The local density ρ is obtained by the weighted arithmetic mean and the dynamic viscosity μ is obtained via the weighted harmonic mean of the kinematic viscosities. The interface between the gas and the liquid is tracked using Lagrangian control points, distributed over the interface. The control points are connected such that they form a mesh of triangular cells. The surface tension force is acquired by obtaining the pull-forces for each marker m and its neighboring cells i: $\vec{F}_{\gamma,i\to m} = \gamma\left(\vec{t}_{mi} \times \vec{n}_{mi}\right)$. The shared tangent $\vec{t}_{mi}$ is known from the control

point locations, and the shared normal vector $\vec{n}_{mi}$ is obtained by averaging the normals of marker m and neighboring marker i. Subsequently, the surface tension force is mapped to the Eulerian background grid using mass-weighing [20] at the position of the interface. After accounting for the surface tension force on all interface cells, the total pressure jump Δp of the bubble is obtained. The pressure jump is distributed over the bubble interface and mapped back to the Eulerian mesh. For interfaces with a constant curvature (i.e. spheres), the pressure jump and surface tension cancel each other out exactly on each marker, but if the curvature varies over the interface (which is the case for deformed bubbles), a small net force will be transmitted.

At each time step, after solving the fluid flow equations, the Lagrangian control points are advected with the interpolated flow velocity. Spatial interpolation of the flow field to the control point positions is performed by a piecewise cubic spline, and temporal integration is performed by Runge-Kutta time stepping. Since the control points may move away from or towards each other, the interface mesh is remeshed afterwards, in order to keep the control points equally distributed on the interface (while keeping the volume enclosed by the dispersed elements constant). The edges of the triangular interface markers are kept within 0.2-0.5 times an Eulerian grid size. The total runtime for numerical simulations is about t=2 s, and the Voronoï volume time series reveals that the clustering is initially transient and settles to a quasi-steady state after t=1 s. Hence, we only consider data after t=1 s from the starting time. The clustering results are averaged over different snapshots at intervals of t=0.05 s.

Each bubble was tracked individually, using the locations of the control points on the interface to acquire the bubble position (center of mass) and bubble shape (aspect ratio), which were stored for further analysis. The aspect ratio is calculated from the ratio between the major and the minor axis χ along the Cartesian axes: $\chi = (\sqrt{d_x d_y})/d_z$. Note that this procedure neglects diagonal shape deformations, so that strongly deformed bubbles oriented diagonally may be attributed an aspect ratio of $\chi \approx 1$ (nearly spherical). In this work we consider bubbles with limited deformability and under mild flow conditions so that these effects can safely be neglected.

Simulations were performed using 16 bubbles in a periodic domain. For ellipsoidal bubbles, Bunner & Tryggvason [8] have indicated that 12 bubbles is the minimum number of bubbles that are required to simulate bubbles rising in a swarm, based on their terminal rise velocity. The present simulations with periodic boundary conditions might not be totally comparable to real systems, as length scales larger than the size of the periodic box might not be captured accurately. The void fraction $\alpha = V_{bubbles}/V_{domain}$ was varied from dilute ($\alpha = 0.05$) up to dense void fractions of $\alpha = 0.4$ by changing the domain size. In all simulations, the spatial resolution was determined by the bubble diameter $1.0 \times 10^{-3} \leq d_b \leq 3.5 \times 10^{-3}$ such that the length

Table 6.1: Summary of the simulation parameters.

Case #	Diameter D [mm]	Void fraction α [%]	Sphere-domain ratio D/L	Kinematic viscosity ν [$\times 10^{-6}$ m^2/s]	Surface tension γ [mN/m]
1-3	1.0	10, 25, 40	0.23, 0.31 ,0.36	1	73
4	1.0	10	0.23	5	73
5	1.0	10	0.23	1	7.3
6-11	2.0	5 - 40	0.18 - 0.36	1	73
12-18	2.5	5 - 40	0.18 - 0.36	1	73
19-26	3.0	5 - 40	0.18 - 0.36	1	73
27-33	3.5	5 - 40	0.18 - 0.36	1	73

of a cubic grid cell $\Delta x = d_b/20$. The physical properties represent typical air bubbles in water conditions, i.e. a density ratio of $\rho_{\text{liquid}}/\rho_{\text{gas}} \approx 1000$, dynamic viscosity ratio $\mu_{\text{liquid}}/\mu_{\text{gas}} \approx 50$ and a surface tension coefficient $\gamma = 0.073$ N m^{-1}.The simulation parameters are summarized in table 6.1. Figure 6.3 provides information on the variation of (a) the aspect ratio χ and (b) the Reynolds number Re as a function of D/L. Here, the Reynolds number is defined as $Re = UD/\nu$, where U is the relative velocity between the bubbles and surrounding liquid. The errorbars in figure 6.3a indicate the time-averaged standard deviation of the aspect ratio for all the bubbles. We observe that the variation of χ, indicated by the errorbars, decreases with increasing D/L due to spatial restriction. The majority of the cases considered here ($D \geq 2$ mm) correspond to Reynolds numbers $Re > 200$ as shown in figure 6.3b. However, the Reynolds numbers are lower (~ 100) for the bubble sizes of D =1 mm and for special cases of high viscosity, Re =12.

In order to avoid initialization effects from influencing our simulation results, the bubble positions were initially set to a non-ordered fashion in the domain. Especially at higher void fractions it is not efficient to subsequently place a bubble randomly in the domain without allowing overlap. Therefore, a Monte-Carlo simulation procedure has been used to generate the initial positions of the bubbles, which works for all void fractions [21, 22]. First, the bubbles are placed as spheres in a structured configuration in the domain in a simple cubic configuration. Depending on the void fraction, the bubbles might overlap with each other. We now define the potential energy of the system as: $E = [|\vec{x}_i - \vec{x}_j|/(R_i + R_j)]^n$, with a variable n characterizing how steep the potential is. The position of a bubble i is given by $\vec{x}_i$ and its radius

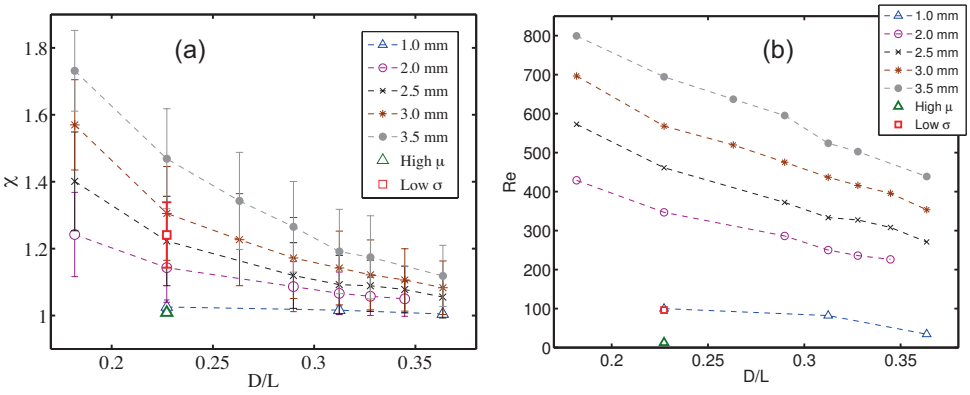

Figure 6.3: (a) The aspect ratio χ vs. bubble-domain length ratio D/L. (b) Reynolds number Re vs. D/L

by R_i. Each bubble is now moved by a small amount in a random direction and the potential energy is determined. A move is accepted whenever the potential energy remains equal or becomes less, whereas a move that increases the potential energy is accepted only if it is smaller than a critical number c: $c = \exp[k(E_{\text{old}} - E_{\text{new}})]$, where k was set to 50. In a single iteration, each bubble is allowed 200 attempts of displacement. Then, the power n is gradually increased from an initial value of 6 up to a final value of 100, and a new iteration starts. The potential energy of the system as a whole decreases during this process, and when the final state has been reached and the bubbles show no overlap at all, the positions of the bubbles are accepted for use as starting positions in the front tracking model. Additionally, in the initial transient of the front tracking simulations, the bubbles accelerate, deform and move through the domain, which also changes their relative positions. This start-up stage is discarded from further analysis. For the random positions of the point-particles as shown in figure 6.2(c), the same procedure was used, except that we chose the number of allowed displacements for each particle per iteration to be 10^4.

6.4 Results and Discussions

We recall that the values of the clustering indicator $\mathscr{C} = \sigma/\sigma_{rnd}$ are: $\mathscr{C} > 1$ for an irregular cluster, $\mathscr{C} = 1$ for a random distribution, and $\mathscr{C} < 1$ for a regular lattice arrangement (figure 6.1). Figure 6.4 shows the typical bubble clustering snapshots of the side view and top view. Figure 6.4(a) displays a snapshot of the case of bubble diameter $D = 1.0$ mm at $D/L = 0.23$. We observe horizontal clustering in one layer in

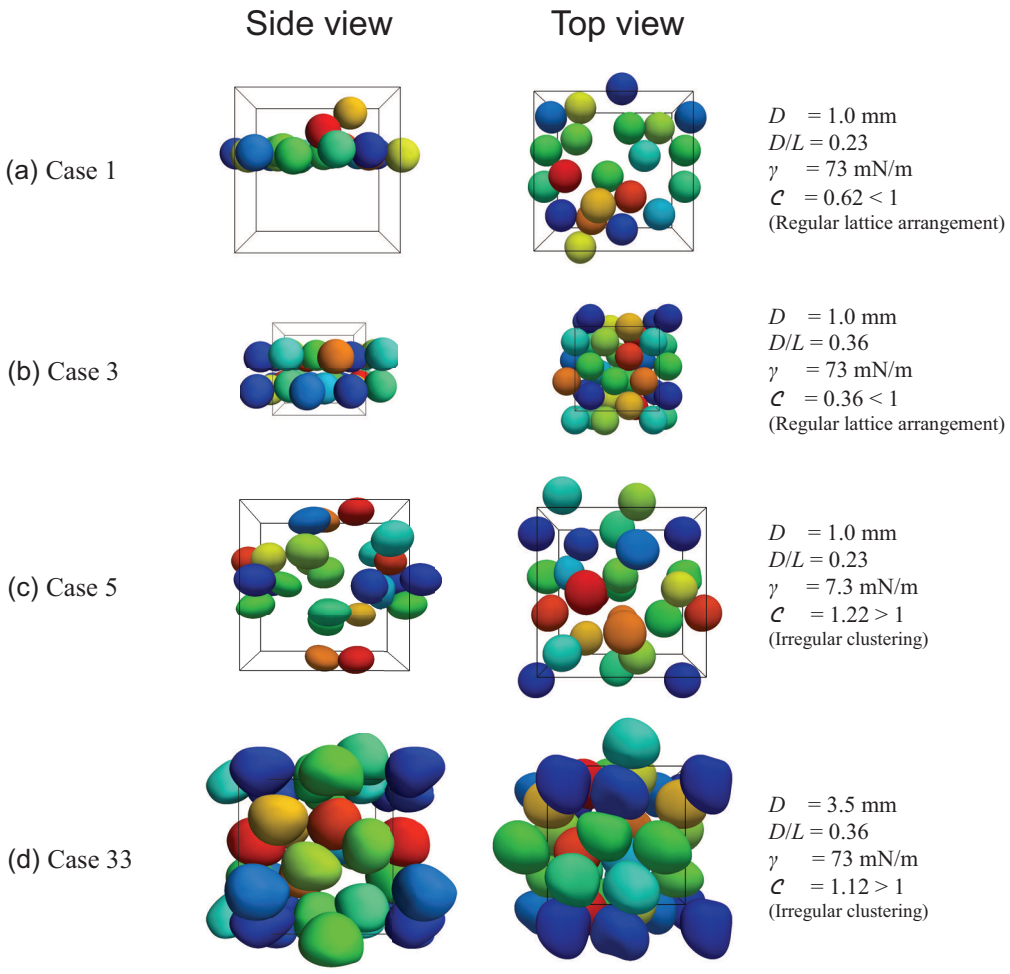

Figure 6.4: Snapshots of bubbles showing typical clustering morphologies from the side and top. The periodic box is indicated by the thin black lines. The bubbles are colored to aid in distinguishing between individual bubbles.

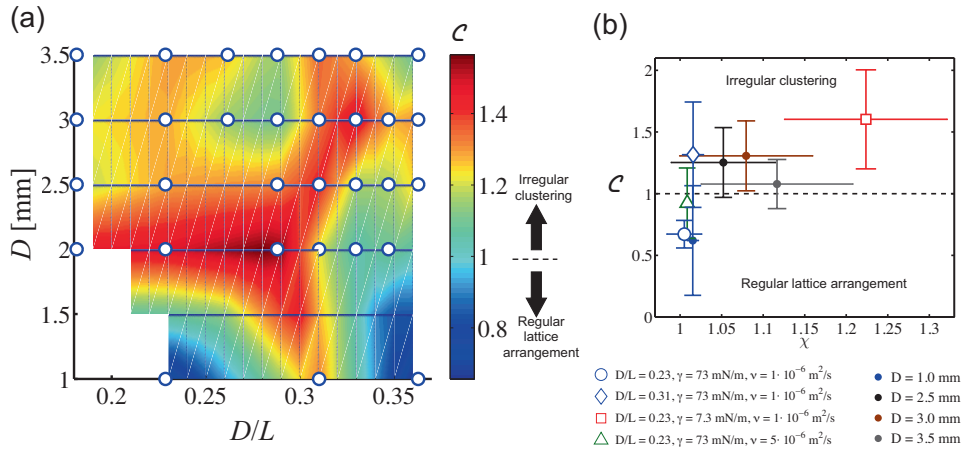

Figure 6.5: (a) Bubble clustering results: A contour plot of the clustering indicator $\mathscr{C}$ as function of the bubble-domain length ratio D/L for all bubble sizes D (in mm). The colorbar indicates the magnitude of $\mathscr{C}$. All the simulation cases in table 6.1 are shown here except 4 and 5. (b) The clustering indicator $\mathscr{C}$, as a function of the aspect ratio χ for: fixed bubble size (*open symbols*), D = 1.0 mm (cases 1, 2, 4, 5 in table 6.1); and fixed bubble-domain length ratio (*solid symbols*), $D/L = 0.36$ (cases 3, 18, 26, 33 in table 6.1). The clustering indicator $\mathscr{C}$ increases with increasing aspect ratio, indicating that the shape of the bubbles plays a crucial role in determining the clustering morphology. Spherical bubbles with an aspect ratio $\chi = 1.015 \pm 0.015$ have $\mathscr{C} < 1$, indicating the regular lattice arrangement. All deformed bubbles with $\chi = 1.015 \pm 0.015$ have $\mathscr{C} > 1$, implying irregular clustering.

the side view. The top view reveals a regular lattice arrangement, which corresponds to $\mathscr{C} < 1$. In figure 6.4(b), $D = 1.0$ mm at $D/L = 0.36$, and the bubbles show horizontal clustering in a double layer, owing to larger D/L (i.e. larger void fraction α), and the value of $\mathscr{C}$ is correspondingly less than 1. It must be noted that the shapes of the bubbles for $D = 1.0$ mm at (a) $D/L = 0.23$ and (b) $D/L = 0.36$ are almost spherical. In figure 6.4(c), we show a case of $D = 1.0$ mm at $D/L = 0.23$ with lower surface tension, where the bubbles are evenly distributed throughout the domain and the horizontal one-layer clustering no longer prevails. In figure 6.4(d), in the case of $D = 3.5$ mm at $D/L = 0.36$, the bubbles are more evenly distributed. The corresponding $\mathscr{C}$ values for both cases are larger than 1, i.e. indicating irregular clustering. One must note that the bubbles with $D = 1.0$ mm at $D/L = 0.23$ with lower surface tension (panel (c)) and those with $D = 3.5$ mm at $D/L = 0.36$ have a deformed shape (panel (d)).

For a quantitative discussion, in figure 6.5(a) we show (as a color contour plot)

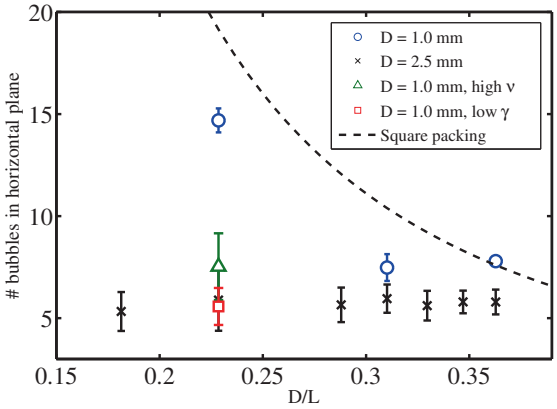

Figure 6.6: The maximum number of bubbles in a horizontal plane. The dotted line shows the values for square packing. The 1 mm bubbles (cases 1-5 in table 6.1) show a increasing trend with decreasing D/L indicating that they form horizontal clusters. The 2.5mm bubbles (cases 12-18 in table 6.1) show almost constant values of 6, implying that there is no horizontal clustering. The result in the case of liquid with high viscosity (case 4 in table 6.1, green triangle) and that for low surface tension (case 5 in table 6.1, red square) are also shown.

the values of the clustering indicator $\mathscr{C}$ at different bubble-domain length ratios D/L and bubble sizes D. The data points in the parameter space (table 6.1) are indicated using open blue circles. The formation of regular lattice arrangements ($\mathscr{C} < 1$) was only encountered in the cases of 1.0 mm diameter bubbles at D/L = 0.23 and 0.36 (figure 6.5(a)). All other cases show irregular clustering ($\mathscr{C} > 1$), but to a different extent.

It is well-known that a rising spherical bubble with a free-slip boundary condition generates little vorticity, whereas a rising deformed bubble has a wide region of wake structure behind it [23]. The amount of vorticity generated from the bubbles determines the clustering morphology. The flow around spherical bubbles can be expected to be close to potential flow, containing little vorticity, and these bubbles form a regular lattice arrangement (in the horizontal plane). Deformable bubbles with larger wake regions show more tendency to aggregate in the vertical direction. Hence, in the discussion of the results, we focus on the bubble shape (or deformability) characterized by the bubble aspect ratio χ. Below, we fix the size and bubble-domain length ratio, and discuss the clustering at different χ.

Figure 6.5(b) shows the values of the clustering indicator $\mathscr{C}$ as a function of the

bubble aspect ratio χ. First, we keep the bubble size constant (D = 1.0 mm shown with open symbols) and discuss results for different bubble-domain length ratios, surface tension, and viscosity. The value of $\mathscr{C}$ increases with an increase in the aspect ratio, indicating that the bubble shape is crucial for the clustering structure. We now fix the bubble-domain length ratio ($D/L = 0.36$) and study the clustering behavior for different bubble sizes shown with solid symbols in figure 6.5(b). Although the fixed parameter is different in this case, we still see the same trend of increasing $\mathscr{C}$ with increasing aspect ratio χ. Overall, we find that the shape of the bubbles is crucial for the structure of the clustering. Considering the error bars in figure 6.5(b), we find that the clustering transition occurs at a critical value of eccentricity, $\chi_c = 1.015 \pm 0.015$. Spherical bubbles with $\chi \lesssim \chi_c$ have $\mathscr{C} < 1$, indicating the regular lattice arrangement. All the deformed bubbles with $\chi \gtrsim \chi_c$, have $\mathscr{C} > 1$, indicating the irregular clustering morphology. In homogeneous bubbly flows at moderate particle Reynolds numbers, mono-dispersed spherical bubbles have been found to organize themselves into microstructures (e.g. [10, 24, 25]). The physical reason is that interactions between bubbles are responsible for a slight excess of horizontal pairs, which is in agreement with present simulations at a high viscosity (case 4, see table 6.1).

We also quantify the intensity of horizontal clustering by counting the maximum number of bubbles at a horizontal plane, for the cases of D = 1 mm and 2.5 mm bubbles. The bubbles are sliced at the horizontal plane and divided by the area of a circle based on the bubble radius. Figure 6.6 shows the maximum number of bubbles in a horizontal plane versus the bubble-domain length ratio. The line obtained from the theory of square packing is also shown for the sake of comparison. On the one hand, the 1 mm bubbles show a trend similar to the theoretical line, indicating that they organize themselves to form horizontal clusters. On the other hand, the 2.5 mm bubbles show almost constant values around 6, indicating the absence of horizontal clustering. The result of the lower surface tension case (case 5 in table 6.1) is rather close to the 2.5 mm case (case 13 in table 6.1) due to deformation. These results for the horizontal clustering are consistent with those obtained from the Voronoï analysis.

6.5 Conclusion

In this chapter, we have applied the three-dimensional Voronoï analysis on DNS data of freely rising deformable bubbles in order to investigate the clustering morphology. The numerics used a front-tracking method that allows the simulation of fully deformable interfaces of the bubbles at different diameters, bubble-domain length ratios, surface tensions, and liquid viscosities. The present Voronoï analysis takes into

account the effects of the number of bubbles and the finite-size. It then provides a clustering indicator $\mathscr{C} = \sigma/\sigma_{rnd}$, where σ is the standard deviation of Voronoï volumes of the bubbles and σ_{rnd} is the standard deviation of Voronoï volumes of randomly distributed particles with finite size. We quantitatively identify two different clustering morphologies: $\mathscr{C} > 1$ for irregular clustering and $\mathscr{C} < 1$ for a regular lattice arrangement. Our results indicate that the bubble deformability, represented by its aspect ratio χ, plays the most crucial role in determining the clustering morphology. A regular lattice arrangement is observed in the case of nearly spherical bubbles with $\chi \lesssim 1.015 \pm 0.015$. When the bubbles are deformable, for $\chi \gtrsim 1.015 \pm 0.015$, an irregular clustering behavior is observed. This clustering behavior is believed to be related to the amount of vorticity generated by the bubbles. The irregular clustering for deformed bubbles is due to the low-pressure regions in their wakes, which attract other bubbles. Spherical bubbles tend to form a regular lattice arrangement due to reduced vorticity generation.

References

[1] E. Calzavarini, M. Kerscher, D. Lohse, and F. Toschi, *Dimensionality and morphology of particle and bubble clusters in turbulent flow*, J. Fluid Mech. **607**, 13 (2008).

[2] F. Toschi and E. Bodenschatz, *Lagrangian properties of particles in turbulence*, Annu. Rev. Fluid Mech. **41**, 375 (2009).

[3] N. G. Deen, R. F. Mudde, J. A. M. Kuipers, P. Zehner, and M. Kraume, *Ullmanns Encyclopedia of Industrial Chemistry, chapter Bubble Columns.* (Wiley-VCH Verlag GmbH & Co. KGaA., ADDRESS, 2000).

[4] R. Zenit, D. Koch, and A. Sangani, *Measurements of the average properties of a suspension of bubbles rising in a vertical channel*, J. Fluid Mech. **429**, 307 (2001).

[5] G. Riboux, F. Risso, and D. Legendre, *Experimental characterization of the agitation generated by bubbles rising at high Reynolds number*, J. Fluid Mech. **643**, 509 (2010).

[6] J. Martínez Mercado, D. Chehata Gómez, D. van Gils, C. Sun, and D. Lohse, *On bubble clustering and energy spectra in pseudo-turbulence*, J. Fluid Mech. **650**, 287 (2010).

[7] I. Roghair, J. Martínez Mercado, M. Van Sint Annaland, J. A. M. Kuipers, C. Sun, and D. Lohse, *Energy spectra and bubble velocity distributions in pseudo-turbulence: numerical simulations vs. experiments*, Int. J. Multi. Flow **37**, 1 (2011).

[8] B. Bunner and G. Tryggvason, *Dynamics of homogeneous bubbly flows. Part 2. Velocity fluctuations*, J. Fluid Mech. **466**, 53 (2002).

[9] B. Bunner and G. Tryggvason, *Effect of bubble deformation on the properties of bubbly flows*, J. Fluid Mech. **495**, 77 (2003).

[10] A. Cartellier and N. Rivière, *Bubble-induced agitation and microstructure in uniform bubbly flows at small to moderate particle Reynolds number*, Phys. Fluids **13**, (2001).

[11] I. Roghair, M. van Sint Annaland, and J. A. M. Kuipers, *Drag Force and Clustering in Bubble Swarms*, AIChE J. **59**, 1791 (2013).

[12] R. Monchaux, M. Bourgoin, and A. Cartellier, *Preferential concentration of heavy particles: A Voronoi analysis*, Phys. Fluids **22**, 103304 (2010).

[13] Y. Tagawa, J. Martínez Mercado, V. N. Prakash, E. Calzavarini, C. Sun, and D. Lohse, *Three-dimensional Lagrangian Voronoi Analysis for clustering of particles and bubbles in turbulence*, J. Fluid Mech. **693**, 201 (2012).

[14] L. Fiabane, R. Zimmermann, R. Volk, J.-F. Pinton, and M. Bourgoin, *Clustering of finite-size particles in turbulence,*, Phys. Rev. E **86**, 035301 (2012).

[15] A. Okabe, B. Boots, K. Sugihara, and S. Chiu, *Spatial tesselations*, 1st ed. (John Wiley & Sons, UK, 2000).

[16] J. Ferenc and Z. Néda, *On the size distribution of Poisson Voronoi cells*, Physica. A **385**, 518 (2007).

[17] S. Unverdi and G. Tryggvason, *A front-tracking method for viscous, incompressible, multi-fluid flows*, J. Comput. Phys. **100**, 25 (1992).

[18] W. Dijkhuizen, I. Roghair, M. Van Sint Annaland, and J. Kuipers, *DNS of gas bubbles behaviour using an improved 3D front tracking model–Model development*, Chem. Eng. Sci. **65**, 1427 (2010).

[19] I. Roghair, Y. M. Lau, N. G. Deen, H. M. Slagter, M. W. Baltussen, M. van Sint Annaland, and J. A. M. Kuipers, *On the drag force of bubbles in bubble swarms at intermediate and high Reynolds numbers*, Chem. Eng. Sci. **66**, 3204 (2011).

[20] N. Deen, M. Van Sint Annaland, and J. Kuipers, *Multi-scale modeling of dispersed gas-liquid two-phase flow*, Chem. Eng. Sci. **59**, 1853 (2004).

[21] D. Frenkel and B. Smit, *Understanding molecular simulation: from algorithms to applications* (Academic Press, San Diego/London, 2002).

[22] R. Beetstra, *Drag force in random arrays of mono- and bidisperse spheres* (PhD thesis, University of Twente, The Netherlands, 2005).

[23] J. Magnaudet and G. Mougin, *Wake instability of a fixed spheroidal bubble*, J. Fluid Mech. **572**, 311 (2007).

[24] X. Yin and D. Koch, *Lattice-Boltzmann simulation of finite Reynolds number buoyancy-driven bubbly flows in periodic and wall-bounded domains*, Phys. Fluids **20**, 103304 (2008).

[25] C. A., M. Andreotti, and S. P., *Induced agitation in homogeneous bubbly flows at moderate particle Reynolds number*, Phys. Rev. E. **80**, (2009).

7
Conclusions and Outlook

In this thesis, we have addressed several key research issues on light particles in homogeneous and isotropic turbulence. Here, we enumerate the major findings from our investigations.

In Chapter 2 (Ref. [1]), we have presented experimental results on the Lagrangian statistics of micro-bubbles in turbulence. Three-dimensional (3D) trajectories of the micro-bubbles were captured using Lagrangian Particle Tracking experiments at a high temporal resolution in the Twente Water Tunnel (TWT). The micro-bubble diameters are $\sim$340 μm and the Taylor-Reynolds numbers Re_λ are varied from 160 to 265. The micro-bubble velocity probability distribution functions (PDFs) have been found to closely follow a Gaussian distribution, independent of Re_λ. But the acceleration PDFs are highly non-Gaussian with intermittent tails. Using stretched exponential functions to fit the acceleration PDFs, the flatness values were found to be in the range of 23–30 and show an increasing trend with Re_λ, consistent with previous experimental [2] and numerical [3] results. A comparison of our results with experiments in von Kármán flows [2, 4–6] suggest that the present micro-bubble acceleration PDF is similar to tracers and bubbles (in von Kármán flows) for very different Re_λ, due to the small Stokes numbers (St $\sim$ 0.02-0.09) in our study. Since the micro-bubble diameter is comparable to the Kolmogorov scale, we do not expect finite-size effects [7] to play a role. Hence, the micro-bubbles almost behave like tracer particles in turbulence.

The next step was to study the effects of finite-size for light particles in turbu-

lence. To this end, in Chapter 3 (Ref. [8]), we studied finite-sized bubbles of diameter ~ 3 *mm* at Reynolds numbers Re_λ, 145–230, and size ratios, $\Xi = D/\eta$, 7.3–12.5. These represent the first measurements in a previously unexplored regime of large (compared to η) and very light (with respect to ρ_f) particles in turbulence. The finite-sized bubbles were tracked using a sled-based two-dimensional (2D) Lagrangian Particle Tracking system in the TWT. The measurement provided information on both the vertical and horizontal components, so it was of vital importance to see if gravity played a role on the Lagrangian statistics in addition to the finite-size. Indeed, we found that gravity produces anisotropy in the acceleration statistics of the vertical component – it adds a g^2 offset to the variance, and decreases the intermittency of PDF, at lower Re_λ. In addition, the bubble acceleration variances clearly indicate the finite-size effect; the variances of both the horizontal and vertical components (with gravity corrections) are about 5 ± 2 times larger than those measured in the same flow for fluid tracers. These experiments are in good agreement with results from DNS simulations of bubbles in turbulence which have implemented the Faxén corrections to account for the particle finite-size [7]. Also, the intermittency of experimental bubble acceleration PDF decreases with increasing size ratios, Ξ.

After investigating dilute, light particle-laden turbulent flows (1-way coupling), we have studied turbulent bubbly flows where the void fraction is significant for bubble-bubble interactions to become important (2-way and even 4-way coupling). In Chapter 4 (Ref. [9]), we have studied the unknown nature of the transition between the classical $-5/3$ energy spectrum scaling for a single-phase turbulent flow and the -3 scaling for a swarm of bubbles rising in a quiescent liquid and of bubble-dominated turbulence. Here, the bubblance parameter (b) [10, 11], which measures the ratio of the bubble-induced kinetic energy to the kinetic energy induced by the turbulent liquid fluctuations before bubble injection, is used to characterise the bubbly flow. We have systematically varied the bubblance parameter from $b = \infty$ (pseudo-turbulence) to $b = 0$ (single-phase flow) over 2-3 orders of magnitude: $\approx O(0.01, 0.1, 5)$ to study its effect on the turbulent energy spectrum and liquid velocity fluctuations. The experiments employ a single-point Eulerian phase-sensitive Constant Temperature Anemometry (CTA) technique, which provides *in-situ* flow information to discard bubble collisions. The liquid velocity PDFs for the bubbly cases ($b > 0$) show asymmetry, and more upward fluctuations compared to a Gaussian profile. When $b < 1$, the liquid fluctuations reveal a weak dependence with the b parameter; a slight decrease in the fluctuations with decrease in b. The energy spectra are found to follow the *-3* subrange scaling not only in the well-established case of pseudo-turbulence, but in all cases where bubbles are present in the system ($b > 0$), in the present parameter regime ($b \gtrsim 0.01$). In turbulent bubbly flow, one approach

is to decompose the velocity fluctuations into spatial and temporal contributions [12–14], and both contributions have been found to exhibit the *-3* subrange [14]. The spatial contribution is characterised by the random spatial distribution of the bubbles, and is not influenced by turbulence, while the temporal contribution changes with the turbulence intensity. In our experiments, we mainly change the temporal contributions by adding the external active-grid-induced turbulence to the system of freely rising bubbles. Since the spatial contribution is dominant in the explored parameter regime [12], we see the robust *-3* scaling for turbulent bubbly flow in a wide variety of conditions ($b > 0$) over 2-3 orders magnitude change in the b parameter.

We have also carried out investigations on the clustering of particles in homogenous isotropic turbulence using a three-dimensional (3D) Voronoï analysis technique. In Chapter 5 (Ref. [15]), we have applied the 3D Voronoï analysis to study particle clustering in turbulence with both numerical data in the point particle limit [16] and experimental data. The analysis is applied to inertial particles (light, neutrally buoyant, and heavy) of different density ratios, Stokes numbers and Taylor-Reynolds numbers (Re_λ). In the entire range of parameters covered, the Voronoï volume PDFs of neutrally buoyant particles agree well with the Γ-distribution, as expected, for randomly distributed particles. At a fixed value of St, the PDFs of Voronoï volumes of light and heavy particles show higher probability to have small and large Voronoï volumes than randomly distributed particles, reflecting the clustering behavior. The standard deviation of normalized Voronoï volumes σ/σ_Γ is used as an indicator to quantify the clustering. Heavy particles show some clustering, and light particles have a much stronger clustering. Both heavy and light particles show a stronger clustering for a higher Re_λ. The maximum clustering for light particles is around St $\approx$ 1-2 for both Taylor-Reynolds numbers. we have also extracted the 3D Voronoï volume PDF from experimental data of micro-bubbles (at St$\sim$0.04), and although this is slightly broader than what is obtained from point-particle simulations, the overall trend is consistent. Finally, we show that the Voronoï analysis can be connected to local flow properties like enstrophy. It is found that the light particles strongly cluster in flow regions with very high enstrophy, whereas heavy particles weakly cluster in low enstrophy regions for all St in the present study. From the Lagrangian autocorrelation of Voronoï volumes we have revealed that the clustering of light particles lasts much longer than that of heavy or neutrally buoyant particles. And because of inertial effects due to the density difference from the carrying fluid, light and heavy particles remain clustered for a much longer time than the flow structures themselves.

In Chapter 6 (Ref. [17]), we have applied the three-dimensional Voronoï analysis on DNS data of freely rising deformable bubbles in order to quantify the clustering morphology. The numerics used a front-tracking method that allows the simulation

of fully deformable interfaces of the bubbles at different diameters, bubble-domain length ratios, surface tensions, and liquid viscosities [18]. The present Voronoï analysis takes into account the effects of the number of bubbles and the finite-size. It then provides a clustering indicator $\mathscr{C} = \sigma/\sigma_{rnd}$, where σ is the standard deviation of Voronoï volumes of the bubbles and σ_{rnd} is the standard deviation of Voronoï volumes of randomly distributed particles with finite size. We quantitatively identify two different clustering morphologies: $\mathscr{C} > 1$ for irregular clustering and $\mathscr{C} < 1$ for a regular lattice arrangement. Our results indicate that the bubble deformability, represented by its aspect ratio χ, plays the most crucial role in determining the clustering morphology. A regular lattice arrangement is observed in the case of nearly spherical bubbles, and when the bubbles are deformable, an irregular clustering behavior is observed. This clustering behavior is believed to be related to the amount of vorticity generated by the bubbles. The irregular clustering for deformed bubbles is due to the low-pressure regions in their wakes, which attract other bubbles. Spherical bubbles tend to form a regular lattice arrangement due to reduced vorticity generation.

In future work, it will be challenging to implement the 3D Lagrangian Particle Tracking technique on the moving-sled system. When this task is accomplished, we can obtain long duration 3D trajectories of light particles such as micro-bubbles in turbulence. Such experimental data could be invaluable for investigations of two-particle statistics like pair dispersion and shape evolution.

In our work on finite-sized bubbles in turbulence, the acceleration PDF obtained from the Faxén corrected numerics shows a difference of factor $\sim$ 2-3 in Ξ compared to the experiments. The reason for this discrepancy between numerics and experiments is yet to be understood. The numerics neither account for the small deformability of the bubbles present in the experiments nor do they consider gravity in the simulations. The capability of the numerical point particle approaches, also those with Faxén corrections, of course remains limited, in particular with respect to the two-way coupling aspects. We have also found a complex interaction between gravity and inertia in our experiments. Clearly, more experimental and numerical data with a full resolution of the particles and their wakes are needed to dig deeper and unravel this interplay. In order to advance our current understanding of finite-sized light particles, experiments using rigid hollow spheres are currently underway in the Twente Water Tunnel. The objective is to extend further our coverage of the light particles phase space by: (i) exploring the finite-size effect by varying the sphere diameters (D) over a wider range, at fixed Re_λ numbers, and (ii) exploring the effect of inertia and gravity by varying the Re_λ, at fixed sphere diameters. Preliminary results on these light rigid spheres have been presented in Appendix 1 of this thesis. An important direction of future research is to study the dynamics of non-spherical particles

(going all the way to flexible fibers) in turbulence, as this is closer to real-world applications. We have carried out preliminary studies on light rods in turbulence using 3D LPT to focus on the rotation statistics; these results are summarized in Appendix 2 of this thesis.

Our experiments on turbulent bubbly flow have revealed that the -3 spectrum scaling seems to be a generic feature in such flow conditions. Remarkably, the -3 spectrum scaling is followed even at very small b parameter values (~ 0.01); i.e. when the void fraction is as low as 0.1%. Hence, the bubbles are able to modify the spectra very efficiently, even though they are present in small numbers, due to the long lifetime of their wakes. In future work, it will be interesting to test until what limit of the b parameter the -3 scaling still holds.

We are currently using the 3D Voronoï clustering analysis to investigate the characteristic Lagrangian spatiotemporal scales of inertial particle clustering in turbulence. For this, we are applying ideas of dynamic heterogeneity, which has been used to study glass transition and jamming in granular systems.

From our point of view, the Voronoï analysis is an excellent means to quantitatively compare clustering effects of particles in experimental and numerical data sets. More three-dimensional experiments of bubbles with larger Stokes numbers will have to be done to have a thorough comparison of clustering between experiments and numerics. In addition to characterizing clustering in an Eulerian framework, the Voronoï analysis offers new insights into the clustering phenomenon from a Lagrangian viewpoint. In future work, it will be interesting to investigate the Lagrangian properties of particle clusters in detail. It is also interesting to study the clustering of finite-sized particles in turbulence.

References

[1] J. Martínez Mercado, V. N. Prakash, Y. Tagawa, C. Sun, and D. Lohse, *Lagrangian statistics of light particles in turbulence*, Phys. Fluids **24**, 055106 (2012).

[2] G. Voth, A. La Porta, A. M. Crawford, J. Alexander, and E. Bodenschatz, *Measurement of particle accelerations in fully developed turbulence*, J. Fluid Mech. **469**, 121 (2002).

[3] T. Ishihara, Y. Kaneda, M. Yokokawa, K. Itakura, and A. Uno, *Small-scale statistics in high-resolution direct numerical simulation of turbulence: Reynolds number dependence of one-point velocity gradient statistics*, J. Fluid Mech. **592**, 335 (2007).

[4] N. Mordant, A. M. Crawford, and E. Bodenschatz, *Experimental Lagrangian acceleration probability density function measurement*, Physica D **193**, 245 (2004).

[5] R. Volk, E. Calzavarini, G. Verhille, D. Lohse, N. Mordant, J.-F. Pinton, and F. Toschi, *Acceleration of heavy and light particles in turbulence: Comparison between experiments and direct numerical simulations*, Physica D **237**, 2084 (2008).

[6] R. Volk, N. Mordant, G. Verhille, and J.-F. Pinton, *Laser Doppler measurement of inertial particle and bubble accelerations in turbulence*, Europhys. Lett. **81**, 34002 (2008).

[7] E. Calzavarini, R. Volk, M. Bourgoin, E. Leveque, J.-F. Pinton, and F. Toschi, *Acceleration statistics of finite-sized particles in turbulent flow: the role of Faxèn forces*, J. Fluid Mech. **630**, 179 (2009).

[8] V. N. Prakash, Y. Tagawa, E. Calzavarini, J. Martinez Mercado, F. Toschi, D. Lohse, and C. Sun, *How gravity and size affect the acceleration statistics of bubbles in turbulence*, New J. Phys. **14**, 105017 (2012).

[9] V. N. Prakash, J. Martinez Mercado, F. E. M. Ramos, Y. Tagawa, D. Lohse, and C. Sun, *Energy spectra in bubbly turbulence*, J. Fluid Mech. (submitted) arXiv:1307.6252 (2013).

[10] M. Lance and J. Bataille, *Turbulence in the liquid phase of a uniform bubbly air–water flow*, J. Fluid Mech. **222**, 95 (1991).

[11] J. Rensen, S. Luther, and D. Lohse, *The effects of bubbles on developed turbulence*, J. Fluid Mech. **538**, 153 (2005).

[12] F. Risso, V. Roig, Z. Amoura, G. Riboux, and A. Billet, *Wake attenuation in large Reynolds number dispersed two-phase flows*, Phil. Trans. R. Soc. A **366**, 2177 (2008).

[13] F. Risso, *Theoretical model for k^{-3} spectra in dispersed multiphase flows*, Phys. Fluids **23**, 011701 (2011).

[14] G. Riboux, D. Legendre, and F. Risso, *A model of bubble-induced turbulence based on large-scale wake interactions*, J. Fluid Mech. **719**, 362 (2013).

[15] Y. Tagawa, J. Martínez Mercado, V. N. Prakash, E. Calzavarini, C. Sun, and D. Lohse, *Three-dimensional Lagrangian Voronoi Analysis for clustering of particles and bubbles in turbulence*, J. Fluid Mech. **693**, 201 (2012).

[16] E. Calzavarini, M. Kerscher, D. Lohse, and F. Toschi, *Dimensionality and morphology of particle and bubble clusters in turbulent flow*, J. Fluid Mech. **607**, 13 (2008).

[17] Y. Tagawa, I. Roghair, V. N. Prakash, M. van Sint Annaland, H. Kuipers, C. Sun, and D. Lohse, *The clustering morphology of freely rising deformable bubbles*, J. Fluid Mech. **721**, R2 (2013).

[18] I. Roghair, M. van Sint Annaland, and J. A. M. Kuipers, *Drag Force and Clustering in Bubble Swarms*, AIChE J. **59**, 1791 (2013).

Appendix 1: Light spheres in turbulence *

We investigate the Lagrangian dynamics of light rigid spheres in homogeneous and isotropic turbulence. Preliminary experiments using the moving-sled based Lagrangian Particle Tracking have been carried out to obtain the two-dimensional (2D) trajectories of spheres in turbulent flow conditions in the Twente Water Tunnel. We measured data of rigid light (hollow) spheres (Density ratio, $\Gamma = \rho_p/\rho_f \sim 0.3$–$0.5$) with a large range of size ratios (D/η = 30, 55, 76, 146) at Re_λ = 160. The velocity PDFs reveal a slightly sub-Gaussian behavior, especially with an increase in the size ratios, although this trend needs to be tested with more data. The acceleration variance of both the horizontal and vertical components are of comparable magnitude, and do not show a change with increasing size ratios, also there is no systematic trend visible.

Dispersed particulate materials carried by turbulent flows are often encountered both in the realm of natural phenomena and in industrial applications. Such turbulent particle-laden flows are typically studied by making simplifying assumptions such as a dilute system (1-way coupling dynamics), spherical shape of the particles, homogenous isotropic turbulence, and so on. The important control parameters in this problem are $[Re_\lambda, \Gamma, \Xi]$, respectively the Reynolds number based on the Taylor scale of the carrying flow, the particle to fluid mass density ratio ($\Gamma \equiv \rho_p/\rho_f$) and the particle diameter to Kolmogorov length (dissipative-length) ratio ($\Xi \equiv D/\eta$). In this thesis, we have focused on light particles in turbulent flows. For dilute flows, using the Lagrangian approach we have so far explored the effects of particle density by studying micro-bubbles (Chapter 2) and the effects of particle finite-size and gravity (Chapter 3) by studying $\sim$3 mm sized air bubbles in turbulence. Once again, we consider the parameter space of existing Lagrangian literature on spherical particles in turbulence (see Figure 7.1). Since we have been studying air bubbles in turbulent water flow, our coverage of the light particles parameter space has been restricted to the density ratio $\Gamma \equiv \rho_p/\rho_f \sim 10^{-3}$. Here, our goal is to expand our coverage of the light particles parameter space in both the density ratio Γ and size ratio Ξ. In order

*Preliminary work by Vivek N. Prakash and other students in the water tunnel lab

to achieve this objective, we have carried out preliminary experiments using rigid hollow light spheres. The region we cover in the parameter space using these spheres (Density ratio, $\Gamma \sim 0.3$–0.5, size ratios, D/η = 30, 55, 76, and 146) has been shown using black solid circles in Figure 7.1.

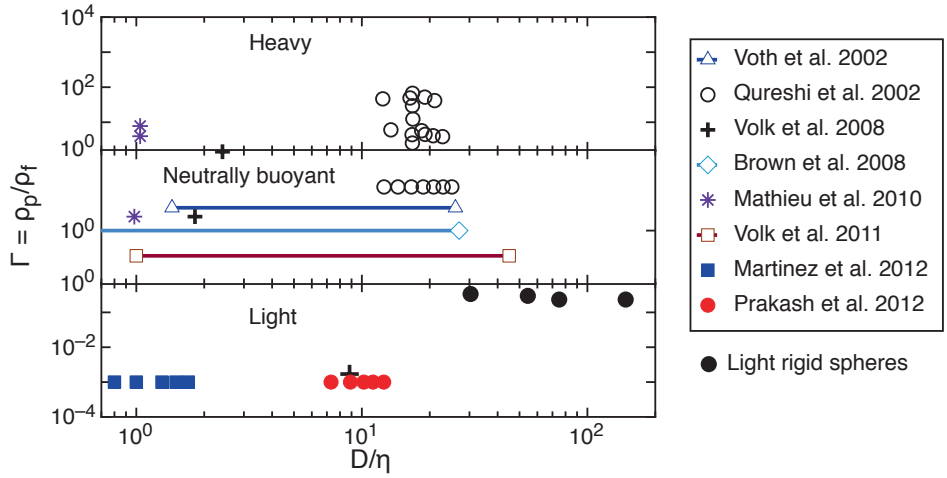

Figure 7.1: Parameter space of the density ratio $\Gamma = \rho_p/\rho_f$ (ratio of particle density to fluid density) versus size ratio, D/η (ratio of particle diameter to the Kolmogorov scale) for particles in turbulence, from data available in literature (from Chapter 3, Ref. [1]). Majority of previous studies (see Chapter 3 for the full references) have focused on $\Gamma \geq 1$, while I have explored light particles ($\Gamma \ll 1$): ■ (Chapter 2, Ref. [2]), ● (Chapter 3, Ref. [1]), ● (Light rigid spheres: present preliminary work).

In addition to extending our coverage of the light particles parameter space, there are two key important aspects of this study which must be taken into consideration. (1) *Deformability:* In our work on finite-sized bubbles (Chapter 3), the bubbles were slightly deformable, and this could have its own effect on the particle dynamics. Here, the spheres are rigid, enabling us to study the particle dynamics in turbulence without the effects of deformability. (2) *Diameter:* Also, in our study of finite-sized bubbles (Chapter 3), we did not have a control on the bubble sizes; there was a distribution in the bubble diameters whose peak value decreased with an increase in Re_λ. Here, the sphere diameter is well-controlled, so these spheres enable us to study issues - (i) Finite-size effects at a fixed Re_λ (i.e. D/η can varied by changing D alone), and (ii) Reynolds number effects at a fixed size (D) (i.e. D/η can varied by changing η alone, i.e. Re_λ). Hence, the study of these rigid light hollow spheres could yield a

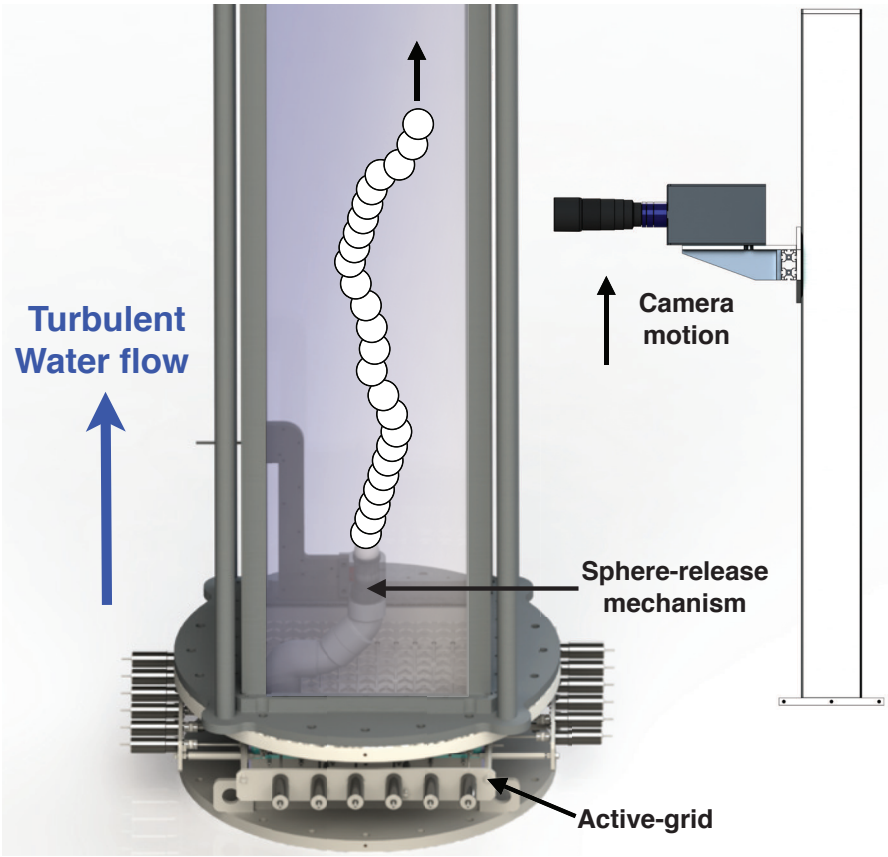

Figure 7.2: A light rigid sphere is released in the Twente Water Tunnel. The sphere-release mechanism is placed above the active-grid and can release one or many spheres stored inside its reservoir. The camera is timed to follow the rising sphere as it moves upward with the turbulent water mean flow, and this allows the measurement of long-duration 2D trajectories of the spheres.

wealth of new information on light particles in turbulence.

In this preliminary study, we have fixed the Reynolds number (Re_λ=160), and we vary the sphere diameters (10, 18.4, 25.4, 49 mm). The sphere density changes slightly ($\Gamma \sim 0.5, 0.4, 0.3, 0.3$) depending on the material used and wall thickness. The spheres are made of polypropylene material and they are hollow, white in color (from Precision plastic balls company, UK).

We designed a new sphere-release mechanism which can be mounted inside one of the access windows of the measurement section, above the active-grid of the Twente Water Tunnel as shown in Figure 7.2. This sphere-release mechanism stores a few spheres in its reservoir and can be released (one or many) when required. The camera is timed to follow the motion of these spheres which rise upward with the turbulent water mean flow. The experimental approach employed in these sphere measurements are basically the same as in the finite-sized bubbles project (Chapter 3). The sphere centers are detected very accurately over time using the circular hough transform technique (same as in the case of finite-sized bubbles). The sphere centers are then tracked over time using standard particle tracking to obtain their two-dimensional Lagrangian trajectories (see Figure 7.3). The sphere trajectories are smoothed using the moving polynomial fitting technique as in Chapter 3. As expected, the spheres rise in a 3D trajectory, but in the present experimental configuration we obtain information on only the vertical component and one horizontal component of the spheres. The spheres appear bigger when near to the camera and appear smaller when away from the camera, we implement corrections for this change in the perspective to minimize the errors. In these sphere experiments, obtaining sufficient statistics is a big challenge which we are yet to overcome. The experiments are currently carried out in batches of ∼tens of spheres, and the water tunnel must be emptied after each experiment, resulting in a long waiting time between experiments. To reach the data quality of the finite-sized bubble experiments, the sphere experiments would take a few months if performed full-time, and this is in spite of employing the moving-sled camera system. So, our current capability to obtain sufficient statistics is limited. Alternate approaches have been tried, but were in vain because they give rise to other significant complications. Here, we present some preliminary results obtained from the data available so far.

In Figure 7.4, we present the normalized Probability Distribution Functions (PDFs) of the Lagrangian velocity components of the spheres. The PDF of the horizontal and vertical components do not show significant differences in general. The velocity PDF seems to follow a Gaussian profile in Figure 7.4(a) for $D/\eta = 30$. As we proceed to cases with higher size ratios, we observe that the PDFs slowly start deviating from the Gaussian profile, and tend towards sub-Gaussianity (Figure 7.4(c,d)). The problem

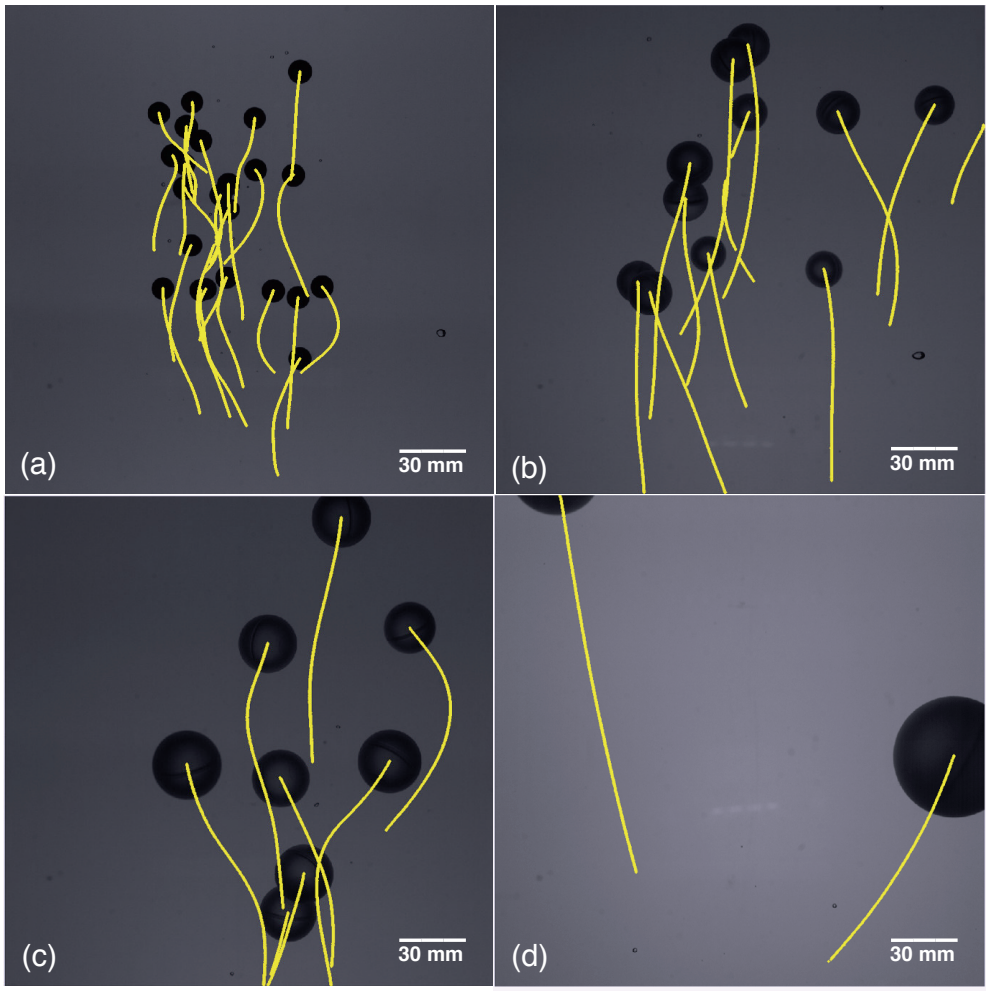

Figure 7.3: Typical experimental images of the spheres rising upwards with the turbulent water mean flow (dark circles). The 2D sphere trajectories over time (obtained after processing) are overlaid on the raw images (shown in yellow color). The sphere diameters are: (a) 10 mm, (b) 18.4 mm, (c) 25.4 mm and (d) 49 mm.

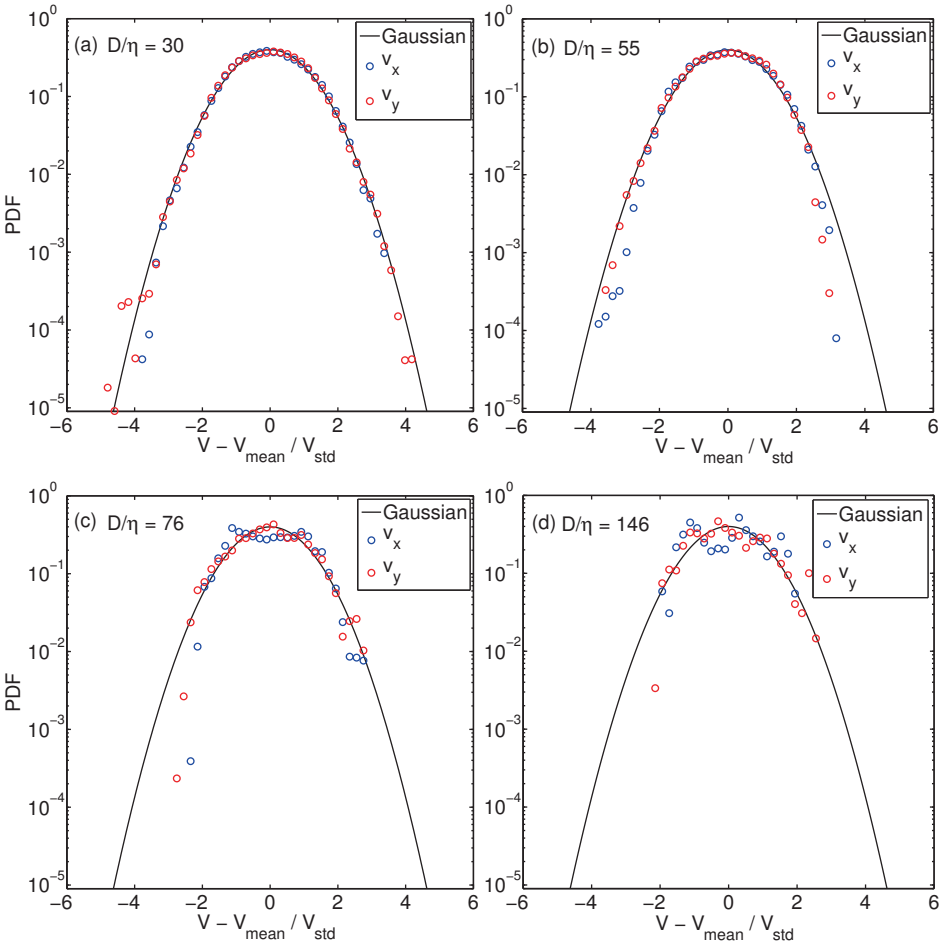

Figure 7.4: Velocity PDFs of the light spheres at $Re_\lambda = 160$. In (a) and (b) the PDFs are closer to a Gaussian profile, and start showing a tendency to become sub-Gaussian in (c) and (d).

with this data is already evident, as the sphere size increases, the amount of datapoints available becomes lesser and lesser. For the cases of Figure 7.4(c,d) we clearly need to collect more data before we can come to any conclusion.

The acceleration variance of the spheres is normalized with those of tracers (from Chapter 3) and shown in Figure 7.5. Here, the finite-sized bubble results are shown, along with the gravity corrections for the vertical component. For the sphere data, there does not seem to be a gravity correction as both horizontal and vertical compo-

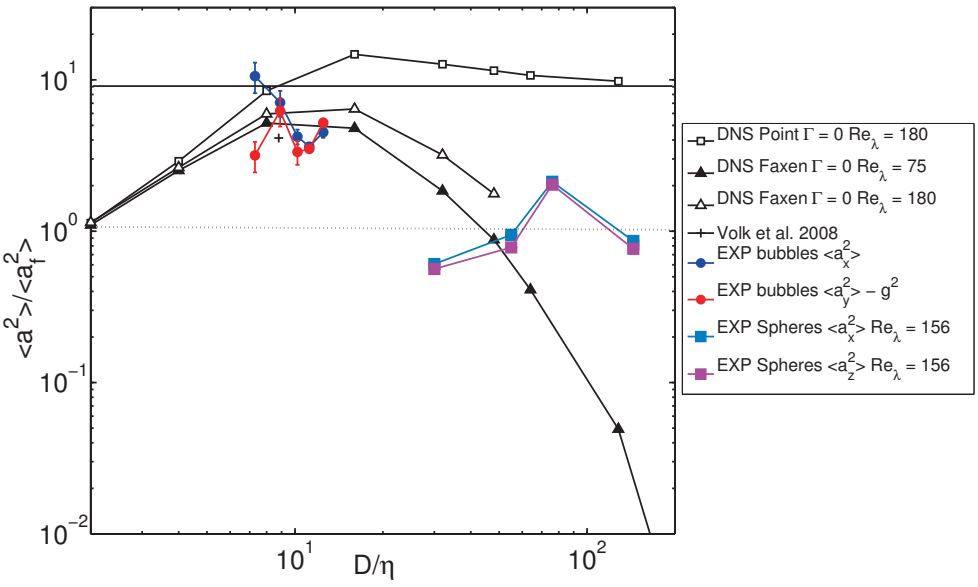

Figure 7.5: The normalized acceleration variance versus the size ratio. Legend: The finite-sized bubble results (●) are represented with error bars, along with a gravity offset for the vertical component a_y (Chapter 3). (□): PP DNS of bubbles [3] (△ & ▲): bubbles from DNS with FCs [3], (+) : single experimental point for bubbles [4], (colored ■) Preliminary light sphere results.

nents are comparable. A possible reason for this could be due to the small density contrast (0.3-0.5) for the present spheres whereas the density contrast was 10^{-3} for bubbles. There is no decrease in the variance with increase in the size ratio as one would expect, also the trend is unclear.

It is evident that more data will reveal the true characteristics of the Lagrangian dynamics of these light spheres in turbulence. Currently, we are testing a new promising idea which might make data collection easier. In future work, it will also be interesting to study the effect of Reynolds number Re_λ on the particle dynamics. Also, it would be interesting to cover density ratios of $\Gamma \sim 10^{-2}$ using different particles to explore the light particles parameter space even further.

References

[1] V. N. Prakash, Y. Tagawa, E. Calzavarini, J. Martinez Mercado, F. Toschi, D. Lohse, and C. Sun, *How gravity and size affect the acceleration statistics of bubbles in turbulence*, New J. Phys. **14**, 105017 (2012).

[2] J. Martínez Mercado, V. N. Prakash, Y. Tagawa, C. Sun, and D. Lohse, *Lagrangian statistics of light particles in turbulence*, Phys. Fluids **24**, 055106 (2012).

[3] E. Calzavarini, R. Volk, M. Bourgoin, E. Leveque, J.-F. Pinton, and F. Toschi, *Acceleration statistics of finite-sized particles in turbulent flow: the role of Faxèn forces*, J. Fluid Mech. **630**, 179 (2009).

[4] R. Volk, N. Mordant, G. Verhille, and J.-F. Pinton, *Laser Doppler measurement of inertial particle and bubble accelerations in turbulence*, Europhys. Lett. **81**, 34002 (2008).

Appendix 2: Light rods in turbulence [†]

Rod-like particles are a commonly found class of non-spherical particles dispersed in many turbulent flows. Here, we investigate the Lagrangian dynamics of light rigid rods in homogeneous and isotropic turbulence. Preliminary Lagrangian Particle Tracking experiments have been carried out to capture the three-dimensional (3D) trajectories of rods in turbulent flow conditions in the Twente Water Tunnel. We have obtained data for light rods (Density ratio, $\Gamma = \rho_p/\rho_f \sim 0.65$) of two different length ratios (L/η = 30, 60) at Re_λ = 160. The translation statistics of the rods reveal interesting features. The velocity PDFs for both length ratios show deviations from Gaussian behavior. The translational acceleration variance shows a nice agreement with previous numerical simulations (DNS) of neutrally buoyant fibers in turbulence [1]. The translational acceleration PDFs for rods of both length ratios show highly non-Gaussian intermittent tails.

In this thesis, we have discussed the dynamics of light particles in turbulence in detail. We have adopted the Lagrangian approach to study dilute systems of light particles in turbulence (1-way coupling). The light particles in our investigations so far (micro-bubbles (Chapter 2), finite-sized bubbles (Chapter 3) and light spheres (Appendix 1)), for all practical purposes were considered to be spherical. Most of the previous research on the Lagrangian dynamics of particles in turbulence have focused on spherical particles [2–4], mostly because of the simplicity of the spherical shape. However, in many real-world applications, the spherical assumption will not really hold. In natural and industrial contexts, the particle shapes tend to be non-spherical; this includes both well-defined shapes such as cylinders (rods), disks, ellipsoids, more complex shapes such as crystals and flexible fibres. Relevant example applications of non-spherical particles in turbulence include the paper-making industry [5], ice-crystals in clouds [6], and suspensions of micro-swimmers [7]. We begin our exploration of non-spherical particle dynamics in turbulence by studying the well-defined shape of rods in turbulence.

Recently Parsa *et al.* [8] investigated the rotation rate of rods in turbulence. They

[†]Preliminary experimental work by Vivek N. Prakash and Huanshu Tan

dispersed neutrally buoyant rods in a turbulent flow created between oscillating grids. The Lagrangian Particle Tracking technique was used to obtain the 3D trajectories of the rods providing information on both the translation and rotation. The rod lengths (L) were in the dissipative regime (η) and the statistics of the rotation rate of the rods (PDF, variance) were of primary interest.

A comprehensive DNS simulation-based study of the dynamics of fibres in turbulent flows was carried out by Shin and Koch [1]. They looked into the translation and rotation dynamics of fibres in isotropic turbulent flows at modest Reynolds numbers (Re_λ=16-50). Regarding the fibre translation dynamics, when $L < \eta$, they found that the acceleration variance increases with an increase in Re_λ. When $L > \eta$, they found a decrease in the normalised acceleration variance with increase in L/η, with a slight dependence on Re_λ. They also found that the fibre velocity and acceleration autocorrelations showed an increasing trend with L/η. Regarding the fibre rotation dynamics, they report a decrease in the rotation rate variance with increase in L/η. Further, they present results on the fibre rotation rate autocorrelations at different L and Re_λ, and discuss the dispersion aspects of the fibres. Many of these DNS simulation results by Shin and Koch [1] are awaiting experimental verification.

The experimental investigation by Parsa *et al.* [8] marked the beginning step in the direction of non-spherical particles in turbulence. When the rod length L increases well beyond the dissipative length-scale, i.e. when $\mathrm{L} > 7\eta$, Parsa *et al.* [8] note that their dynamics will be different. Also, changes in the rod density will further complicate the dynamics. There is a lot to be done experimentally as many fundamental questions remain unexplored. Motivated by these issues, we have conducted preliminary investigations of light rigid rods with $\mathrm{L} \sim 30\eta, 60\eta$ in homogenous isotropic turbulence.

The experiments with light rigid rods have been conducted in the Twente Water Tunnel as shown in Figure 7.6. The sphere-release mechanism (described in Appendix 1) is also used to release the rods into the water tunnel. A small number of rods are placed beneath a light sphere in the sphere-release mechanism. The light sphere essentially acts a lid, and when it leaves the mechanism, all the rods are dispersed into the measurement section and rise along with the upward turbulent water mean flow. The rod trajectories are captured using the 3D Lagrangian Particle Technique as they pass through the cubic measurement volume fixed by the four-camera arrangement. These preliminary experiments are carried out at a mean flow speed of 30 cm s^{-1}, corresponding to a Reynolds number of Re_λ = 160.

The rods used in our experiments are basically made of wooden (Density ratio, $\Gamma = \rho_p/\rho_f \sim 0.65$) cocktail sticks / toothpicks (standard supermarket quality) which are accurately cut to the required lengths (10, 20 mm), and their diameter is 2 mm.

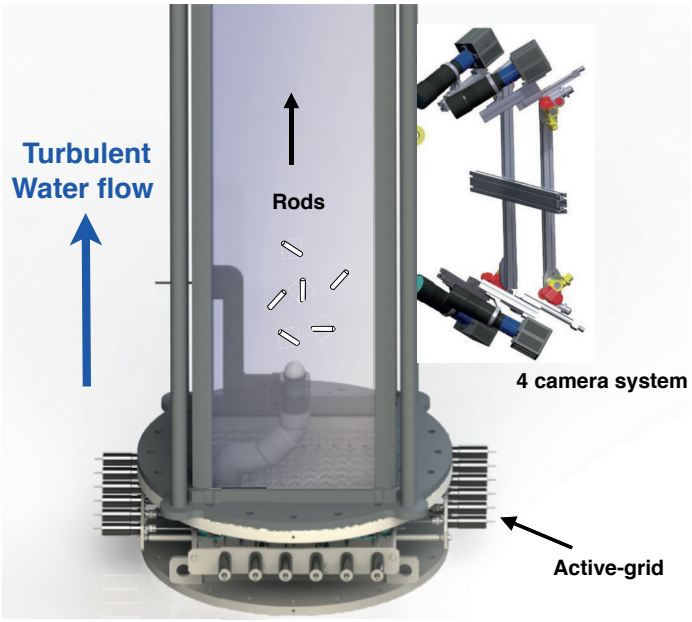

Figure 7.6: Light rigid rods are released in the Twente Water Tunnel using the sphere-release mechanism (Appendix 1). The four-camera system captures the 3D trajectories of the rods are they move upward with the turbulent water mean flow.

Figure 7.7: Raw image from one of the four cameras in the 3D LPT experiments, the visible white dots represent the ends of the rods. The rods are obtained from the 3D positions of their visible edges using a robust reconstruction algorithm.

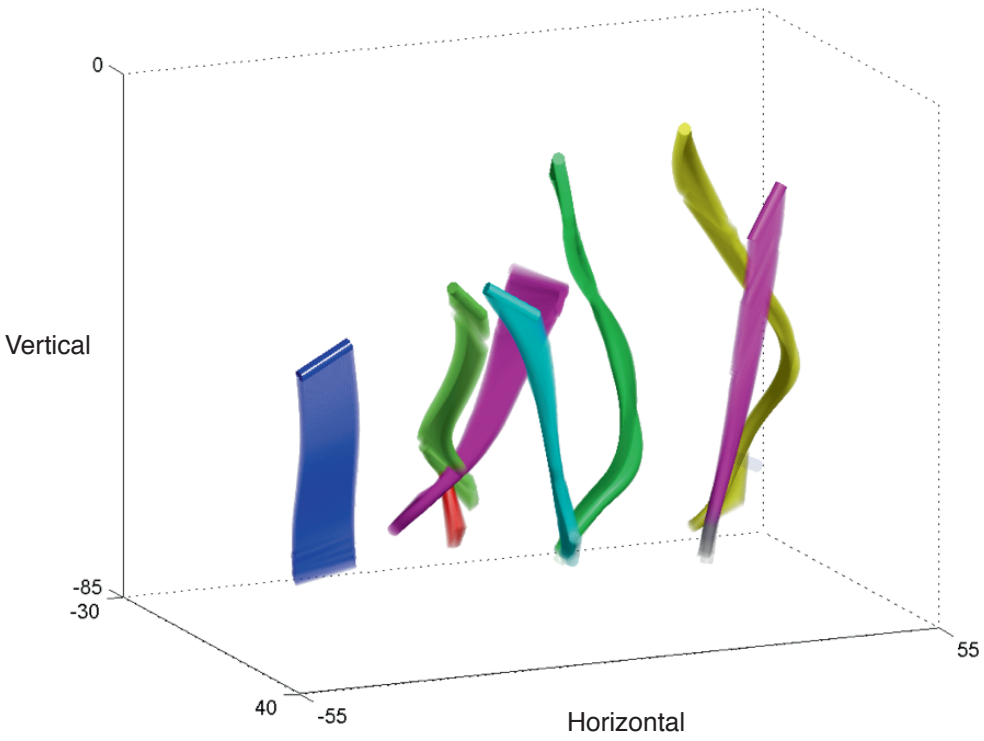

Figure 7.8: The reconstructed three-dimensional (3D) trajectories of the rods from the experiments.

These cut rods are carefully painted with black color in the middle regions and the ends (2 mm) are left uncolored. The idea is that under suitable illumination using a combination of white light sources and a black background, the uncolored parts of the rods are visible are dots in the images (see Figure 7.7). A pre-calibrated four-camera arrangement (as in Chapter 2) is used to capture the 3D trajectories of the visible rod ends. A robust multi-step reconstruction algorithm is applied to the data of visible rod ends to obtain the 3D rod trajectories and their angular orientations (see Figure 7.8). These measurements provide information on both the translation and rotation dynamics of the rods over time. The trajectories are smoothed using the moving polynomial fitting technique as in Chapter 2. In order to study the translation dynamics, we consider the mid-point of the rods and look at its dynamics over time. The rotation analysis is more complicated, and we are currently still trying to find the optimal angular smoothing. Hence, we present here only the preliminary results on translation dynamics.

The current experiments with the rods present the same challenge for collecting sufficient statistics as in the light sphere experiments in Appendix 1. The sphere-release mechanism can only be used for the release of a limited number of rods ($\sim$25) in batches, and the water tunnel must be emptied after each experiments, once again resulting in a long waiting time in-between experiments. Although we can slightly increase the number of rods in each experiment, we avoid this because a large number of rods in the images would overlap heavily, and an accurate reconstruction of the rods becomes more difficult. In future work, we need to find a faster and efficient way to collect a large amount of data for sufficient statistics. Here, we present preliminary rod translation results from the data acquired so far.

We present the translation velocity Probability Distribution Functions (PDFs) of the light rods in Figure 7.9. The results for 'long cylinders' refers to the case of $L = 20$ mm rods, $L/\eta = 60$, and the results for 'short cylinders' refers to the case of $L = 10$ mm rods, $L/\eta = 30$, where η is the Kolmogorov length scale (333 μm) for this Re_λ (= 160). In these results, the x and z components represent the horizontal directions, with z being the depth component and the y component is in the vertical direction. The three velocity components v_x, v_y and v_z in Figure 7.9(a) and (b) almost follow the Gaussian profile near the peaks, but show differences in the tails. In general, the velocity PDFs for both the long and short rods show deviations from the Gaussian profile. The depth direction (z component) is slightly less accurate than the other two directions, but more data is needed to fully understand these deviations from Gaussian behaviour, as there is no clear trend visible at the moment.

In Figure 7.10, we present the translational acceleration variance of the rods normalised by the acceleration variance of fluid tracers versus the length ratio (L/η).

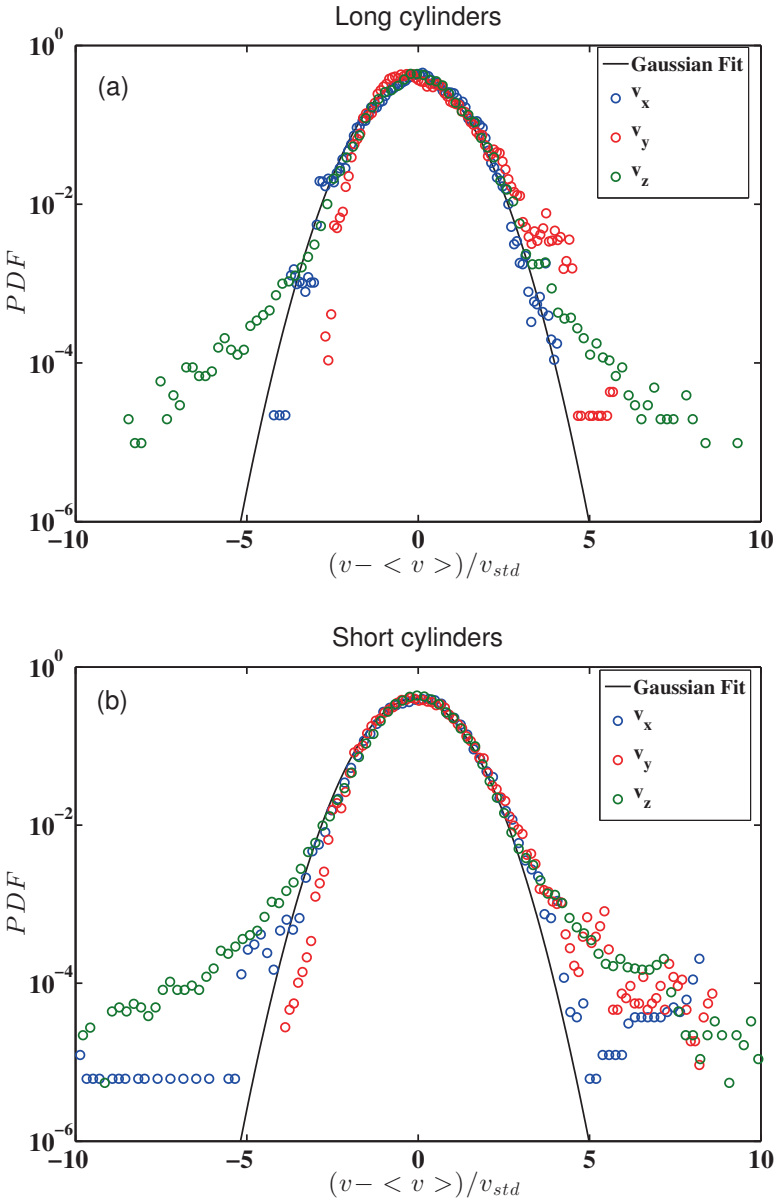

Figure 7.9: Rod translation statistics: velocity PDFs of (a) Long cylinders (b) Short cylinders.

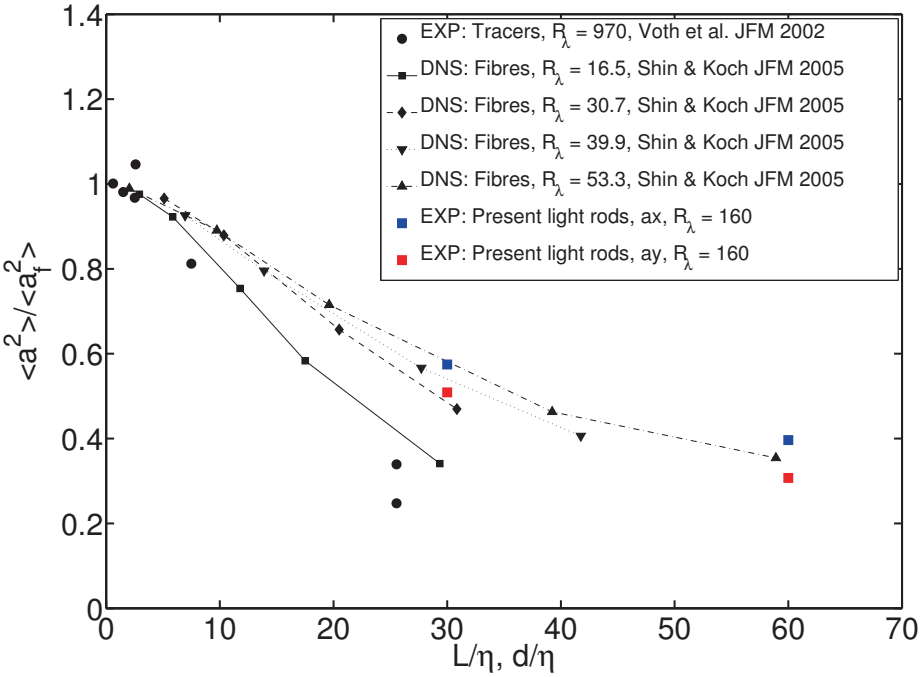

Figure 7.10: Rod translational acceleration variances, compared with DNS results from Shin and Koch [1], and fluid tracer experimental results from Voth *et al.* [9]. The present preliminary results on the light rods show a nice agreement with the DNS results of Shin and Koch [1], with a decrease in the variance as L/η increases.

Here, we show the results on fibres in turbulence from the DNS simulations by Shin and Koch [1] and fluid tracer experiments at high $Re_\lambda = 970$, from Voth *et al.* [9]. As expected, for fluid tracers, the normalised acceleration variance decreases with increase in d/η, where d is the spherical particle diameter. The fibre results from numerics also show a decrease in variance with increase in L/η, and the decrease is sightly lesser when the Re_λ value increases. The present acceleration variance results of the light rods are shown (in colour), and they agree nicely with the numerical results of Shin and Koch [1]. The a_z (depth) component results of the rods is not shown here, as it is less accurate (due to limitations in the 3D LPT technique) and more data is needed to converge to a reliable value.

In Figure 7.11, we show the translational acceleration PDFs of the rods. In case of both the long and short rods, in Figure 7.11(a) and (b) respectively, we observe

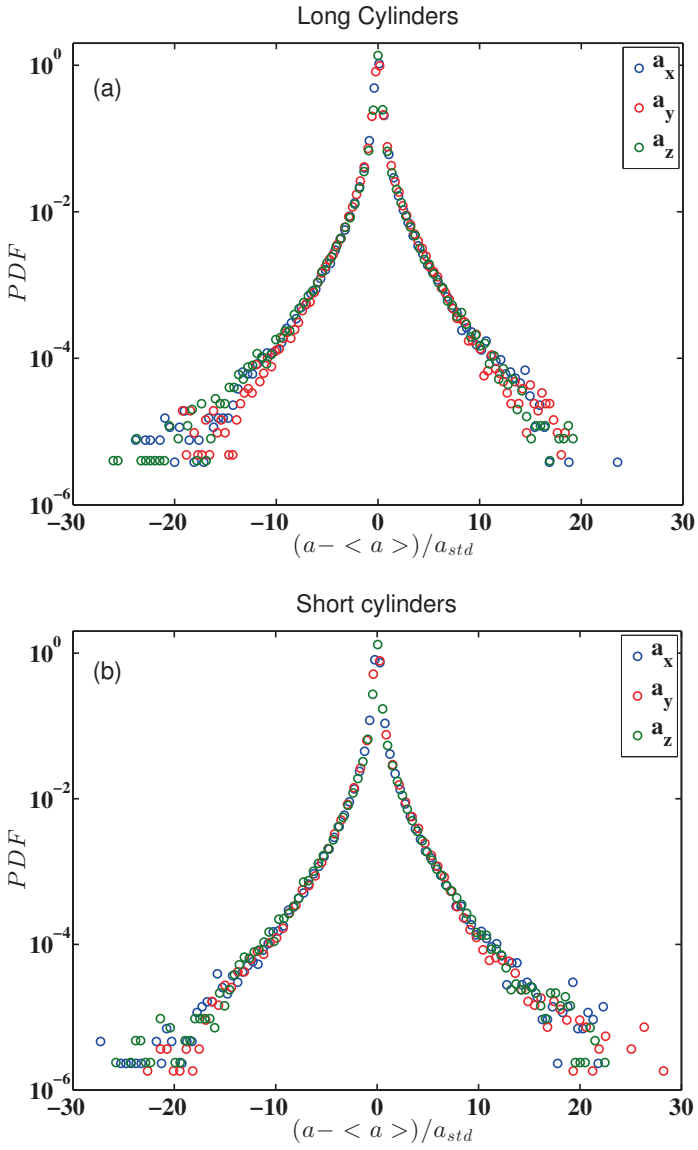

Figure 7.11: Translation statistics: acceleration PDFs

a remarkable isotropy in the statistics, i.e. the a_x, a_y and a_z components are almost identical. Also, these acceleration PDFs are highly non-Gaussian, with stretched intermittent tails. It will be very interesting to compare these PDFs with those of tracers and other particles to further understand the underlying effects of intermittency. At the moment, we do not see significant differences between the long and short cylinders. Once we have more data, we will be able to quantify this intermittency. It is also interesting to connect these translational statistics with the rotational statistics to further understand the dynamics of light rods in turbulence.

In future work, it will be interesting to study light rods at an expanded range of length ratios (L/η). Also, the effect of the Reynolds number (Re_λ) on the rod dynamics will be an interesting issue. We have not presented rotational statistics here, but this will be of major interest in future investigations. As we have mentioned above, we also need to improve the experiments to make them more faster and efficient to collect a large amount of data for sufficient statistics.

References

[1] M. Shin and D. L. Koch, *Rotation and translational dispersion of fibres in isotropic turbulent flows*, J. Fluid Mech. **540**, 143 (2005).

[2] F. Toschi and E. Bodenschatz, *Lagrangian properties of particles in turbulence*, Annu. Rev. Fluid Mech. **41**, 375 (2009).

[3] A. La Porta, G. Voth, A. M. Crawford, J. Alexander, and E. Bodenschatz, *Fluid particle accelerations in fully developed turbulence*, Nature. **409**, 1017 (2001).

[4] D. Lohse, *Particles go with the flow*, Physics **1**, 18 (2008).

[5] F. Lundell, L. D. Soderberg, and P. H. Alfredsson, *Fluid Mechanics of Papermaking*, Annu. Rev. Fluid Mech. **43**, 195 (2011).

[6] S. C. Sherwood, V. T. J. Phillips, and J. S. Wettlaufer, *Small ice crystals and the climatology of lightning*, Geophysical Research Letters **33**, (2006).

[7] D. Saintillan and M. Shelley, *Orientational Order and Instabilities in Suspensions of Self-Locomoting Rods*, Phys. Rev. Lett. **99**, 058102 (2007).

[8] S. Parsa, E. Calzavarini, F. Toschi, and G. A. Voth, *Rotation Rate of Rods in Turbulent Fluid Flow*, Phys. Rev. Lett. **109**, 134501 (2012).

[9] G. Voth, A. La Porta, A. M. Crawford, J. Alexander, and E. Bodenschatz, *Measurement of particle accelerations in fully developed turbulence*, J. Fluid Mech. **469**, 121 (2002).

Summary

This thesis deals with the broad topic of particles in turbulence, which has applications in a diverse number of fields. A vast majority of fluid flows found in nature and in the industry are turbulent and contain dispersed elements. In this thesis, I have focused on light particles (air bubbles in water), where the particle density is lesser than the carrier fluid. I have experimentally investigated the dynamics of these light particles in turbulence, which is an unexplored regime in current literature.

The experiments have been carried out in a unique large-scale (8m high, 3-storey) multi-phase turbulence facility (Twente Water Tunnel), which is part of the European High-performance Infrastructures in Turbulence (EuHIT) consortium. I experimentally studied micro-bubbles in turbulence (Chapter 2) by implementing the challenging three-dimensional (3D) Lagrangian Particle Tracking (LPT) technique for the first time in the group. This technique allows us to track thousands of micro-bubbles in fully developed turbulence in 3D, with full temporal and spatial resolution. The results on acceleration statistics showed that the micro-bubbles almost behave like fluid tracers. As a next step, I studied $\sim$3 mm sized air bubbles in the turbulent water flow to investigate the effects of finite-size and gravity (Chapter 3). To this end, I developed a sled-based particle tracking system, which moved a high-speed camera along with the bubbles, and provided results with greatly improved statistics. For the data analysis, I adapted the Circular Hough Transform technique (for the first time in this field) to detect the centres of overlapping bubbles in the images. The bubble acceleration statistics indicated that both the effects of finite-size and gravity are important for the dynamics. Gravity has two new surprising effects: it produces anisotropy in the acceleration statistics of the vertical component by adding a g^2 offset to the variance, and it decreases the intermittency of the acceleration PDF at lower Re_λ. The experiments are in good agreement with results from DNS simulations of bubbles in turbulence with Faxén corrections which account for the particle finite-size. In these studies, the bubble concentration in the system was low (dilute) and we assumed a 1-way coupling (only carrier fluid turbulence affects the particles) dynamics to hold.

When the particle concentration is no longer dilute, the particles have a back-reaction on the surrounding liquid turbulence (2-way coupling and even 4-way cou-

pling dynamics). I adapted the phase-sensitive hot-film anemometry technique to measure the liquid velocity fluctuations in a turbulent bubbly flow (Chapter 4) at gas volume fractions up to 2%. I investigated a long-standing research issue regarding the transition from the $-5/3$ classical Kolmogorov energy spectrum scaling for a single-phase flow to the well-known -3 pseudo-turbulence spectrum scaling for a swarm of freely rising bubbles in a quiescent liquid. This study uncovered another surprising result: the -3 spectrum scaling was found in all cases where bubbles were present in the system, even at very low gas volume concentrations (0.1%). Remarkably, the bubbles are able to modify the spectra very efficiently, even if they are present in small numbers, due to the long lifetime of their wakes. Hence, the -3 spectrum scaling seems to be a generic feature of turbulent bubbly flows.

We have also studied the preferential clustering of inertial particles in turbulence. We developed a three-dimensional (3D) version of the Voronoï analysis technique and applied it to both numerical and experimental data to study the clustering phenomena in detail. In addition to characterizing particle clustering in an Eulerian framework, the 3D Voronoï analysis technique offered new insights into the clustering phenomenon from a Lagrangian viewpoint (Chapter 5). For point-particle DNS simulations of inertial particles in turbulence, the Eulerian Voronoï analysis revealed that both light and heavy particles show clustering behavior, but light particles show much stronger clustering. The maximum clustering for light particles was found to be around $St \sim$1-2, for two different Re_λ, which is consistent with results from other clustering studies in literature. The Lagrangian Voronoï analysis showed that the clustering of light particles lasts much longer than that of heavy or neutrally buoyant particles. We also found that light and heavy particles remain clustered for a much longer time than the flow structures themselves, and this is attributed to inertial effects arising from the particle density difference to the carrier fluid. We have also applied the Voronoï analysis to investigate the clustering morphology of a swarm of freely rising deformable bubbles (Chapter 6) obtained from DNS simulations. We quantitatively identify two different bubble clustering morphologies: irregular clustering and regular lattice arrangement. It was found that the bubble deformability plays the dominant role in determining this clustering morphology. Currently, we are studying light rigid spheres of different sizes to extend our exploration of the light particles parameter space (Appendix 1). Also, there are ongoing experimental investigations to study non-spherical particles in turbulence using light rigid rods (Appendix 2).

Samenvatting

Dit proefschrift gaat over het brede onderwerp ‘deeltjes in turbulentie’, welk een breed scala aan toepassingen heeft. Een overgrote meerderheid van vloeistofstromen in de natuur en in industrie zijn turbulent en bevatten deeltjes. De nadruk van dit proefschrift ligt op lichte deeltjes bijv. lucht bellen in water. Hiermee bedoelen we deeltjes waarvan de dichtheid kleiner is dan de omringende vloeistof. Ik heb experimenteel onderzoek gedaan naar de dynamiek van deze lichte deeltjes in turbulente stromingen, een vrijwel onverkend gebied in de huidige literatuur.

Deze experimenten zijn uitgevoerd in een unieke, grootschalige (8 meter hoog, 3 verdiepingen) meer-fasestromingsopstelling, genaamd de Twente Water Tunnel. Deze maakt deel uit van het EuHIT (Europese hoge-prestaties infrastructuren voor turbulentie) consortium. Ik heb experimenteel onderzoek gedaan naar microbelletjes in turbulentie (Hoofdstuk 2) door, voor het eerst in onze groep, het uitdagende driedimensionaal (3D) Lagrangiaans volgen van deeltjes (LPT) te implementeren. Deze techniek stelt ons in staat om duizenden microbelletjes in volledig ontwikkelde turbulentie te volgen in 3D, met hoge tijd- en ruimteprecisie. Ons onderzoek naar de statistische eigenschappen van de versnelling van microbelletjes heeft aangetoond dat ze bijna perfect de stroming volgen. Daarna heb ik het effect van een eindige grootte en zwaartekracht op $\sim$3 mm grote luchtbelletjes in turbulente waterstromingen onderzocht (Hoofdstuk 3). Om dit te bewerkstelligen heb ik op een slee gebaseerd deeltjesvolgsysteem ontwikkeld welke een hogesnelheidscamera met de belletjes mee laat bewegen. Dit heeft tot gevolg dat onze resultaten nu aanzienlijk verbeterde statistiek hebben. Voor de data-analyse heb ik gebruik gemaakt van de cirkelvormige Houghtransformatie (als eerst in dit onderzoeksgebied) om overlappende belletjes te detecteren in afbeeldingen. De statistische analyse van de versnelling van belletjes tonen aan dat zowel de eindige grootte als de zwaartekracht belangrijk zijn voor de dynamiek. Zwaartekracht heeft twee verrassende effecten: het introduceert anisotropie in de statistiek van de versnelling van de verticale component door het verschuiven van de variantie met g^2, en het vermindert de intermittentie van de versnellings-PDF voor lage Re_λ. De experimenten zijn in overeenstemming met de resultaten van numerieke simulaties van belletjes in turbulentie met Faxén-correcties, die rekening houden met

de eindige grootte van deeltjes. In al dit onderzoek was de concentratie van de belletjes laag (verdund) en hebben we aangenomen dat de dynamiek van de deeltjes met éénrichtingskoppeling (enkel de turbulentie van de omringende vloeistoef beïnvloedt de deeltjes) konden worden beschreven.

Wanneer de deeltjesconcentratie hoog is, zal de stroming niet alleen werken op de deeltjes maar zullen de deeltje ook reageren op de omringende turbulente vloeistof (tweerichtingskoppelings- en zelfs vierrichtingskoppelingsdynamiek). Ik heb de fasegevoelige hete-film-anemometrietechniek aangepast om de fluctuaties van de stroomsnelheid te kunnen meten in een turbulente bubbelstroom met gasvolumefracties tot 2%. Ik onderzocht de aloude vraagstelling over de transitie van de $-5/3$ klassieke Kolmogorov-energiespectrumschaling voor een enkel-fasige stroming naar de welbekende -3-pseudo-turbulentie-spectrumschaling voor een groep van opstijgende bellen in een stilstaande vloeistof. Dit onderzoek onthulde nog een verrassend resultaat: de -3-spectrumschaling werd gevonden voor alle gevallen wanneer er bubbels aanwezig waren in het systeem, zelfs voor erg lage gasvolumefracties (0.1%). Het is opmerkelijk dat de bellen in staat zijn het spectrum efficient te veranderen door de lange levensduur van hun zog, zelfs als ze aanwezig zijn in kleine aantallen. Het lijkt er dus op dat een -3-spectrumschaling een generieke eigenschap is van turbulente bubbelstromingen.

We hebben ook de voorkeursclustering van deeltjes met traagheid in turbulentie onderzocht. We hebben een drie-dimensionale (3D) versie van de Voronoï-analyse ontwikkeld en toegepast op zowel numerieke als experimentele data om in detail het clusteringsfenomeen te bestuderen. Naast het karakteriseren van het clusteren van deeltjes in het Euleriaanse kader, heeft de 3D-Voronoï-analysetechniek ons nieuw inzicht gegeven in het clusteringsfenomeen in het Lagrangiaanse kader (Hoofdstuk 5). Euleriaanse Voronoï-analyse van directe numerieke simulaties van puntdeeltjes met traagheid in turbulentie heeft aangetoond dat zowel lichte als zware deeltjes clustergedrag vertonen, echter lichte deeltjes laten een sterker clustergedrag zien. De maximale clustering for lichte deeltjes trad op bij ongeveer $St \sim$1-2, voor twee verschillende Re_λ, en was in overeenstemming met resultaten van andere studies in de literatuur. De Lagrangiaanse Voronoï-analyse heeft aangetoond dat de clustering van lichte deeltjes veel langer duurt dan dat van zware deeltjes of van deeltjes met neutraal drijfvermogen. Ook vonden we dat lichte en zware deeltjes voor een veel langere tijd geclusterd blijven dan de stromingsstructuren zelf. Dit wordt toegeschreven aan traagheidseffecten die voortvloeien uit het dichtheidsverschil tussen het deeltje en de omringende vloeistof. We hebben ook de Voronoï-analyse toegepast om de clusteringsmorfologie van een groep opstijgende, vervormbare bellen (Hoofdstuk 6), verkregen uit directe numerieke simulaties, te analyseren. We hebben kwantitatief

twee verschillende belclusteringsmorfologiën gevonden: onregelmatige clustering en rangschikking in een regelmatig rooster. Het blijkt dat de vervormbaarheid van de bellen een dominante rol speelt in de clusteringsmorfologie. Op dit moment bestuderen we lichte bollen van verschillende groottes om de parameterruimte van lichte deeltjes verder te verkennen (Appendix 1). Ook zijn er lopende experimenten om niet-bolvormige deeltjes in turbulentie zoals lichte starre staafjes te bestuderen (Appendix 2).

Scientific output

Publications

Peer-reviewed journals

1. Vivek N. Prakash, Y. Tagawa, E. Calzavarini, J. M. Mercado, F. Toschi, D. Lohse, and C. Sun, *"How gravity and size affect the acceleration statistics of bubbles in turbulence",*
   New Journal of Physics, 14, 105017, (2012).
   see Chapter 3 of this thesis.
   – Part of NJP focus issue on *'Dynamics of Particles in Turbulence'*
   – Featured in *"Highlights of 2012 - New Journal of Physics"*, which brings together some of the very best research published in NJP in 2012
   – NJP *Video Abstract Prize 2013*

2. J. M. Mercado[#], Vivek N. Prakash[#,*], Y. Tagawa, C. Sun, and D. Lohse, *"Lagrangian statistics of light particles in Turbulence",*
   Physics of Fluids, 24, 055106 (2012).
   see Chapter 2 of this thesis. ([#]Equal contribution) (*corresponding author)

3. Vivek N. Prakash, J. M. Mercado, F. E. M. Ramos, Y. Tagawa, D. Lohse, and C. Sun, *"Energy spectra in bubbly turbulence",* (2013)
   (submitted to the Journal of Fluid Mechanics, under review)
   see Chapter 4 of this thesis.

4. Y. Tagawa, J. M. Mercado, Vivek N. Prakash, E. Calzavarini, C. Sun, and D. Lohse, *"Three-dimensional Lagrangian Voronoi analysis for clustering of particles and bubbles in turbulence"*,
   Journal of Fluid Mechanics, 693, 201-215 (2012).
   see Chapter 5 of this thesis.

5. Y. Tagawa, I. Roghair, Vivek N. Prakash, M. van Sint Annaland, H. Kuipers, C. Sun, and D. Lohse, *"The clustering morphology of freely rising deformable bubbles",*
   Journal of Fluid Mechanics, 721, R2 (2013).
   see Chapter 6 of this thesis.

Manuscripts under preparation

6. Y. Tagawa, K. Saitoh, Vivek N. Prakash, E. Calzavarini, D. van der Meer, C. Sun, and D. Lohse, *"Dynamic heterogeneity of inertial particles in homogeneous isotropic turbulence",* (2013)

7. Vivek N. Prakash, K. R. Sreenivas, and J. H. Arakeri, *"The role of viscosity contrast on plume structure in laboratory modeling of mantle convection",* (2013) *(Master's thesis research)*

Media coverage

New Journal of Physics Video Abstract Prize - 2013
(*Vivek N. Prakash et al., New J. Phys, 2012*)

- Featured on the New Journal of Physics front page: www.njp.org (July 2013 -)
- News item featured on the front page of the University of Twente: www.utwente.nl (Aug 2013)
- University of Twente news article:
  "UT Researchers win NJP video competition" (Aug 2013)
- Dutch media:
  "UT-Onderzoekers winnen internationale videowedstrijd", RTV-OOST NL

  "Onderzoekers UT winnen prijs met video", Tubantia NL

Seminars and Presentations

Invited Seminars

1. *JMBC Multiphase flow group meeting*, TATA Steel Europe, The Netherlands, May 2013
2. *FOM-DROP Meeting,* TU Delft, The Netherlands, Apr 2013
3. Department of Bioengineering, Stanford University, USA, Nov 2012
4. Fluid Mechanics Seminar, University of California, Berkeley, USA, Nov 2012
5. Department of Physics, University of California, San Diego, USA, Nov 2012
6. *JMBC Turbulence group meeting*, TU Eindhoven, The Netherlands, Apr 2011
7. *Physics of Fluids group seminars*, University of Twente, 2010-2012

Seminars and Presentations

Conference Presentations

1. *European Turbulence Conference (ETC) 14*, Lyon, France, Sep 2013
2. *COST Particles in Turbulence Conference*, TU Eindhoven, Jul 2013
3. *American Physical Society, 65th Annual Meeting - DFD*, San Diego, USA, Nov 2012
4. *9th Euromech Fluid Mechanics Conference*, University of Rome "Tor Vergata", Italy, Sep 2012
5. *COST Particles in Turbulence workshop*, Lorentz Center, Leiden, May 2012
6. *American Physical Society, 64th Annual Meeting - DFD*, Baltimore, USA, Nov 2011
7. *COST Particles in Turbulence Conference,* University of Potsdam, Germany, Mar 2011
8. *American Physical Society, 63rd Annual Meeting - DFD*, Long Beach, USA, Nov 2010
9. *Physics@FOM Meeting (poster),* Veldhoven, The Netherlands, 2010 – 2013
10. *JMBC Burgersdag (poster),* The Netherlands, 2010 – 2013

Training - Schools attended

1. *Hands-On Research in Complex Systems Advanced Study Institute*
   Shanghai Jiao Tong University (SJTU), Shanghai, China, June 2012.
2. *New Challenges in Turbulence Research II*
   Ecole de Physique, Les Houches, France, March 2012.
3. *Tutorial School on Fluid Dynamics: Topics in Turbulence*
   University of Maryland, USA, May 2010.
4. *J.M. Burgerscentrum (JMBC) courses:*
   – *Experimental Techniques in Fluid Mechanics,*
   University of Twente, The Netherlands, April 2010
   – *Particle Image Velocimetry,* TU Delft, The Netherlands, Oct 2009

Teaching Experience

- *Experimental Techniques in Physics of Fluids* (Master course), 2011– 2013
  Course Instructor: Prof. Chao Sun
  Teaching assistant: gave classroom and laboratory lectures
- *Physics of Fluids* (Bachelor course), 2010
  Course Instructor: Prof. Jacco Snoeijer
  Teaching assistant: Grading homeworks and class tutorials

Student mentoring

- Jun 2013 – present, Varghese Mathai, *PhD student*
- July 2013 – Sep 2013, Jon Brons, *Master student (capita selecta project)*
- Aug 2012 – Aug 2013, Tobias Foertsch, *Master student (thesis project)*
- Jan 2013 – Apr 2013, Huanshu Tan, Shanghai University, *visiting Master student (internship project)*
- July 2012 – Dec 2012, Ernesto Mancilla, UNAM, Mexico, *visiting PhD student*
- Summer 2011 – 2013, *Experimental Techniques in Physics of Fluids course*,
  Course Instructor: Prof. Chao Sun
  Supervised 1-week Master student assignments, totally 9 students

Acknowledgements

I met *Detlef* for the first time at a Euromech conference in Manchester back in September 2008. It was there that he offered me a PhD position. After visiting the group a week later, I immediately decided to accept the offer. This has turned out to be one of the best decisions I have ever made. I have thoroughly enjoyed my stay here in the Physics of Fluids Group over the past four years. Being in this group is like living in a dream: 'a scientific paradise' full of exceptionally smart but also very nice people. When I first arrived here from India, I had left my familiar comfort zone and everything was so new to me. I would like to thank everyone in the group for making me feel 'at home' here with all the support and hospitality.

In particular, I would like to thank:

Detlef, for being a father figure and an outstanding mentor. I very much admire your personality, leadership and your scientific abilities, and hope that I have managed to pick up some of your qualities. I have learned so much from you; both professionally and personally. Your approach to practising science - thinking, writing, and presenting, has left a deep impression on me. I thank you for having faith in my abilities and nurturing me right from the start to help me grow and succeed. I very much appreciate that you went out of your way to support me when I began looking for my next position. Thank you very much for everything that you have done for me. All my PhD expectations and ambitions have been surpassed, thanks to you. It has been a great experience working with you, and I am certainly looking forward to future scientific collaborations.

Chao, for being the 'best advisor' I could ever have ! Dear Chao, you have been an excellent supervisor and also one of my best friends (for all the others reading this, yes, it is possible!). You have played a decisive role in my training and development. It has been such a joyful experience working with you all these years. We were so excited about our experiments; whenever something was new, I would run to tell you and we would run back together to the lab to see the experiments in action.

We became fired-up with energy whenever we saw a new result. It was such a pleasure to discuss research, papers, the future, and life in general. In hindsight, I realize that I probably spent more time with you than anyone else in the group. The way we discussed and wrote the papers together and the satisfaction we derived from the end product was simply unparalleled; I will always remember that awesome feeling. Thank you for being there for me whenever I needed you. Thanks for your tremendous support, encouragement and advice on matters ranging from PhD research and extending all the way to the fellowship proposals, future planning and personal matters; I am forever indebted to you. I hope that we will continue working with each other in the years to come. We have spent wonderful times attending conferences together, and outside work at dinners and parties; I had a great time with you.

Federico, for key contributions to my research and support. I have benefitted a lot from interacting with you, and your inputs to our collaborative work on finite-sized bubbles have been very helpful. Thank you for chairing the very successful EU COST Action MP0806: 'Particles in Turbulence' program. I was able to attend very useful conferences and meetings supported by this program. Thank you for agreeing to be on my PhD graduation committee.

Mickael Bourgoin, for fruitful interactions. I have gained a lot through our discussions at meetings in Les Houches and Rome. Thank you for sending me the EPS particles; we are planning to use them in our ongoing project. Thank you for inviting us (as guest editor) to submit our work on finite-sized bubbles to the New Journal of Physics (NJP) special issue on 'particles in turbulence'. The NJP video abstract prize was a fantastic bonus! Thank you for agreeing to be on my PhD graduation committee.

Leen van Wijngaarden, for sharing your wisdom and experiences, it is so nice to be around you. Thank you for agreeing to be the chairman of my defence ceremony. *Devaraj van der Meer, Rob Hagmeijer* and *Harry Hoeijmakers* for agreeing to be on my PhD graduation committee, thank you for taking the time.

Yoshi, for being a good postdoc collaborator and a very good friend. Thank you for the collaboration on the Voronoi clustering analysis, it added a new direction to my thesis complementing the water tunnel experiments. Our collaborative efforts led to several joint publications and the work has been well appreciated by others in the community. It was a memorable experience writing the Voronoi papers together with you, Julian and Chao. You have been very supportive and provided me with very

useful tips/suggestions for data analysis and experiments in the other projects. We travelled together to different conferences and I very much enjoyed your company. Thank you for everything.

Julian, for being an excellent collaborator, and a very good friend. You introduced me to everything in the lab and in the group. It was a lot of fun doing the experiments together and learning from you. I enjoyed all the parties and dinners we had together. Although you left halfway through my PhD, we were always in touch. I appreciate your important contributions to the bubbly turbulence project even though you were busy with your postdoc work in Chile. Also, I am thankful that you were always available for discussions over Skype for advice on experiments. Thank you for everything, and I hope you will soon join the 'Professors' club, good luck !

Enrico, for crucial inputs and a very fruitful collaboration. We spent more than half a year on the NJP finite-sized bubbles paper. During this period, we interacted heavily over Skype and emails, and I have learnt a lot from you. Your contribution to the data analysis and interpretation in the NJP paper was significant. Also, thank you for providing us your DNS simulation data on point-particles in turbulence for the Voronoi analysis. I have also enjoyed discussions with you at conferences in Potsdam and Rome.

Ivo Roghair, Martin van Sint Annaland and Hans Kuipers, for a fruitful collaboration. Thank you for providing us your data on the fully resolved, front-tracking DNS simulations of freely rising bubbles. We applied the Voronoi analysis to this data to study the bubble clustering morphology, and it eventually led to a very nice joint article.

Devaraj van der Meer, Michel Versluis and Jacco Snoeijer, for many stimulating discussions over the years, I have learnt so much from all of you. *Jacco*, when I was a teaching assistant for the bachelor Physics of Fluids course along with *Ceyda* and *Koen*, I was so impressed with your teaching methodology that I plan to follow the same approach when I get the opportunity to teach in the future.

Roberto Verzicco, Andrea Prosperetti, and Xuehua Zhang, for interesting discussions and dinner conversations when you visited the group.

Roberto Zenit, for many beneficial discussions, and for sending Ernesto Mancilla here for a short stay in our lab.

K. R. Sreenivas and Jaywant H. Arakeri, for your continued support and encouragement over the years. I was able to come here because of you, thank you.

Gert-Wim and *Martin*, for being the 'best technicians' and the backbone support for the water tunnel lab. *Gert-Wim*, you are a genius when it comes to designing and building new setups. You aim for perfection, and in the end we always have an outstanding result. *Martin*, I have come to you so many times for help with the experiments, and you always lent a helping hand, thank you. We have relied heavily on both of you and without your help we would not be able to proceed with our work. I have also enjoyed working with both of you all these years. During my PhD, we made many important changes in the water tunnel: the active-grid position, the moving-sled camera system, the bubble islands, the implementation of the sphere-release system, the external pump system, and the list goes on. All of this went smoothly and in the best possible manner, thanks to both of you.

Joanita, for efficiently taking care of all the administrative tasks. You are always the person with all the answers, and you amazingly manage to handle so many requests from everyone in the group. Thank you so much for your help with all the paperwork and your advice to make my stay here and travels comfortable.

Bas, for being the backbone support for all our computational infrastructure. Thank you for your prompt help to solve all my issues related to computers and electronics. You also took care of the PIV cluster, the active-grid and other electrical wiring systems.

Shashank and *Rodolfo*, for being very nice housemates. *Shashank*, you helped me adjust to life here when I first arrived. Looking back over the past four years, we've had such a wonderful time together. You know me and my situation better than anyone else here. You were always there for me, during both happy and sad times, thank you so much for everything. Thanks for teaching me how to cook, and for all the nice meals :) Thanks also for pushing me to try new things like for example ice-skating or flying on the glider planes which was a fantastic experience. I am pleased that you will be next to me on the big day. *Rodolfo*, its been a nice experience living with you. I have enjoyed our conversations on varied topics and learned many new things from you. Thanks also for cooking nice and exotic meals. I have also enjoyed travelling with you in Sweden and Italy.

Sander, for being a very good friend and companion. Thanks for your help in the water tunnel lab on many occasions like setting up of the LDA, PIV systems. Thanks also for many suggestions and ideas over the years, and for your help with the NJP video. Thank you for taking so many good photographs of me, and the 'appealing' thesis cover. I enjoyed the movie nights at your house, along with Fede, Alvaro and others, and dinners with you, Chao and others. We have also travelled together on many occasions to Maryland, DC, Sweden, Italy, and Friesland. I particularly enjoyed our three-week trip to China, where we visited many places in Beijing, Xian, and attended the important and useful Hands-on school on complex systems in Shanghai. Over the years, I have enjoyed hanging out with you, and I am happy that you will also be next to me on the big day.

Over these years, I have enjoyed the company of many colleagues and friends in the group, past and present. *Dennis van Gils*, thank you for your initial help with the LDA and CTA techniques at the beginning stages of my PhD. *Fede and Alex*, I started using my office only during the last two years, and it has been nice sharing my office with both of you. *Fede (Andale, Andale)* and *Kike*, we laughed so much together, both at the office and outside, it was pure awesome fun, thank you. It is in your nature to make people around you smile. *Oscar*, you are one of the most charming persons I have met, you have been a very good friend. *Claas-Willem*, I have always enjoyed talking to you, about life in general or about our future research careers, thank you for your advice on various matters. *Rodolfo, Fede, Guillaume, Sander H, and Sander W*, the awesome trip to Sweden where we saw the Northern Lights was a once-in-a-lifetime experience. I also thank *Rodolfo, Dennis van Gils, Oscar, Claas-Willem, Fede, Kike, Alex, Rianne, Guillaume, Sander W, Hanneke, Joost, Tess, Pascal, Bram Verhaagen, Ivo Peters, Erwin, Mathijs, Roeland, Tim Segers, Mark-Jan, Erik-Jan, Michiel, Theo, Loreto, Rajaram, Hrudya, Richard, Tak, Ceyda, Koen, Daniela Narezo, Nikolai, Marise, Bart, Stef, Marine, Helen and Michelle* for other wonderful times. *Rodolfo, Claas-Willem, Fede, Kike, Guillaume, Sander*, it was so relaxing to go to the city for a drink on Friday nights. *Guillaume,* thanks for the nice dinners and parties at your house. I also enjoyed spending time with the postdocs in the group, I thank *Siddhartha, James, Kristjan, Yantao and Songchuan*. *Tuan*, I have enjoyed chatting with you about many topics, my favourite one was how you went from working on turbulence to droplet impact. *Uncle Alvaro*, I have always admired your cheerful and pleasant personality, and enjoyed hanging out with you, Thanks for your advice during my postdoc search. *Amy*, thanks for the nice dinners with friends and interesting discussions. *Antonin and Henri*, I have very much enjoyed interacting with both you, and learnt more about the ways of the french people. *Antonin*, thanks

also for your advice on my postdoc search. At this point, I would also like to thank *Anubhab Roy*, a good friend of mine, for very crucial, unbiased advice during my PhD and postdoc search.

I had the opportunity to mentor quite a few students during my stay here. *Varghese*, you started when I was finishing, thank you for understanding my situation with many deadlines and being supportive. It has been a pleasure working with you so far, and I wish you all the very best for your future. *Jon*, thank you for your excellent work on the sphere experiments. *Tobias*, thanks for initiating the work on fibres and showing that it is a promising problem to study. Thanks also for your other contributions to painting the spheres, and the NJP video filming. My best wishes for your future. *Huanshu*, with little help, you managed to accomplish the challenging task of reconstructing the 3D trajectories of the rods and recovering their orientations, you did a very good job. You were a very good student, and it was very nice to work with you. Thank you for your positive feedback and my best wishes for your future. *Ernesto*, it was nice to have you here, Thanks for your help with the bubbly turbulence experiments, and for laying the groundwork for other bubbly projects. *Dennis Bakhuis*, I thank you for your contributions to the lab experiments in the beginning stages of my PhD. As part of the Experimental techniques course, I supervised one-week master student projects, which have been very useful for our own research. I thank *Jeroen, Bram, Ella, Geert, Frank, Joost, Raguram,* for their contributions and positive feedback.

Outside the group, I enjoyed the company of many other friends. *Burcu*, I have enjoyed spending time with you over the years and our conversations during those much needed coffee-breaks. Thanks for being my gym-buddy, for whatever its worth, I went to the gym regularly for many months this year. *Jithin*, our awesome dinners and parties with Shashank were so legendary. *David, Andreea, Olga, Elif*, it has been nice interacting with all of you at different occasions. I would also like to thank other friends in the Indian community here at Enschede, *Abhinendra, Omkar, Dhirendra, Somnath, Kartikeya, Naveen, Aditya, and Himanshu*. *Deepak*, I have enjoyed dinners with you, and catching up on movies, karting, and travelling with you. It was an awesome experience to go with you to the F1 German GP. Four years is a long time, and I have met many people along the way, my apologies if I forgot to mention some of you here. I thank all my friends and relatives back in India, the US, and other parts of the world, for supporting me indirectly.

Finally, I wholeheartedly thank my family: my parents *Veena* and *Nagendra*, sister *Vijetha*, uncle *Lingaraj* and aunt *Kathyayini*; this thesis is dedicated to them. They have always been extremely supportive and encouraged me to pursue my goals. I am happy that my mother will travel all the way to be here with me on the big day.

About the author

Vivek N. Prakash was born on September 26, 1985 in Bangalore, India. When he was six years old, his family moved to Sydney, Australia, and returned to Bangalore after two years. He stayed in Bangalore for the next 17 years till his master's degree. He studied in Christ School, Vijaya High School and the National Pre-University College, Jayanagar, Bangalore. He developed a keen interest in science and mathematics during his school days. His participation in the National Intel Science Talent Discovery Fair (2001) made him start thinking about a research career.

In 2003, for his undergraduate degree, Vivek enrolled in R.V. College of Engineering (RVCE) in Bangalore, and chose to study mechanical engineering as it was a 'perfect fit' for his diverse interests in science and technology. An introductory course in fluid mechanics gave him a glimpse of its challenging nature and captured his fascination. He received several awards for his excellent all-round academic performance during his bachelor studies - 'The LG electronics scholarship and potential manager award' for the best student in mechanical engineering (in 2006), and 'Cognizant Technology Solutions - Best outgoing student award' in mechanical engineering (in 2007). In 2005 and 2006, he was awarded a Summer Research Fellowship by the Jawaharlal Nehru Centre for Advanced Scientific Research (JNCASR), Bangalore, to pursue a research internship project in the fluid dynamics lab at JNCASR. This summer internship further kindled his interest in fluid mechanics and led him to pursue a research career. In 2007, he decided to continue working in the same lab at JNCASR with Professor K.R. Sreenivas for his master's thesis research on 'Laboratory modelling of mantle convection'. His research was also co-supervised by Professor Jaywant H. Arakeri at the Indian Institute of Science, Bangalore.

In October 2009, Vivek moved to Europe to pursue his doctoral studies in the Physics of Fluids Group at the University of Twente, The Netherlands. His doctoral research on 'Light particles in turbulence' was supervised by Professors Detlef Lohse and Chao Sun. Recently, he started developing an interest in the applications of fluid mechanics in biological problems. In order to pursue this further, in Jan 2014 he will move to Stanford University, California, USA, where he will begin his postdoctoral research with Professor Manu Prakash at the bioengineering department.

Vivek N. Prakash earned a PhD in applied physics for his research on `Light particles in turbulence' in the Physics of Fluids group at the University of Twente, The Netherlands, in 2013. He is originally from Bangalore, India, where he received an MS in engineering mechanics from JNCASR, and a BE in mechanical engineering from RVCE.